12

JAYCOR

205 South Whiting Street
Alexandria, Virginia 22304

(12)

(6)

PRELIMINARY EXPERIMENTAL DESIGN AND THEORETICAL INVESTIGATION OF A PLASMA IMPLOSION DRIVEN MASS ACCELERATOR

(9) Final Report

12 9 1

(14) JAYCOR ~~FINAL REPORT NO.~~ J207-81-008

prepared by:

(10) D. A. Tidman and S. A. Goldstein
~~JAYCOR~~
205 S. Whiting Street
Alexandria, VA 22304

submitted to:

(11) 1981

Department of the Army
US Army Armament R&D Command
ATTN: Dr. Peter Kemmey
DRDAR-PRW-FS
Dover, NJ 07801

(15) Contract: DAAK10-80-C-0267
Amount: $49,900
Period: 9/29/80 - 6/30/81

CONTENTS

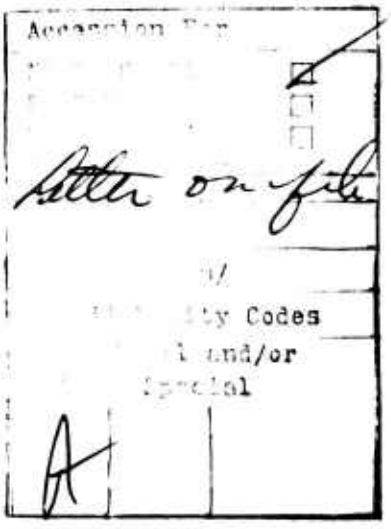

1. INTRODUCTION

The basic idea that motivated this research effort is the prospect that a series of timed z-pinch plasma implosions could be used to sequentially propel a projectile to high velocities. Such a process would provide us with a new type of electrically driven gun with the potential for achieving projectile velocities well above those attainable by chemical guns. The concept in its earliest form is described in references 1-4 and the system appears to have the attractive feature of being potentially rep-ratable. The current flows axially along sections of the accelerator instead of perpendicular to the projectile path as in a rail gun, i.e., plasma pressure propels the projectile, not the $\underline{j}x\underline{B}$ force.

The primary objective of this research was to design a test module which if built could be used to investigate the effectiveness of such z-pinch implosions for projectile propulsion. Other objectives were to examine background experimental information on z-pinch implosions and to explore a range of parameters using a lumped-parameter computer model for the implosions and their driving circuits. Our results for these three components of the program are presented in sections 2, 3, and the Appendix.

2. DESIGN AND ENGINEERING DRAWINGS FOR AN ACCELERATOR TEST MODULE

In this section we have compiled the drawings (Figures 1-28) that provide a design for a single test module. Such a design also has the advantage that it can easily be stacked into an assembly of more than one module. This has been verified by using internal GT-Devices funds to construct and perform experiments with several of these modules of various implosion chamber designs. In order to provide the reader with a visual image we have also enclosed a picture (Figure 29) showing an

assembled 5 module system. The remaining figures and captions give the particular drawings that were prepared under the support of this contract.

3. LUMPED PARAMETER IMPLOSION MODEL

This model is based on an equation for the driving circuit energized by a capacitor, together with a snow-plow model for the imploding z-pinch discharge. The snow plow model assumes that all of the gas initially present in the implosion volume is swept up by the radially imploding discharge which in turn is propelled inward by the $\underline{j}\times\underline{B}$ force involving the self azimuthal magnetic field. The geometry is shown in Figure 30 and the model is discussed in reference 1.

In this section we first summarize the model equations, and then present some computer results that provide us with a view of how things vary over a range of parameters. The basic equations are an equation of motion for the imploding plasma shell:

$$m_g \frac{d}{dt}\left[\left(1 - \frac{a^2}{a_w^2}\right)\dot{a}\right] = -\frac{I^2 \ell}{ac^2} \qquad (1)$$

together with the circuit equation

$$V = \frac{Q}{C} = \frac{d}{dt}(LI) + IR$$

$$L = L_g + \frac{2\ell}{c^2}\ell n\left(\frac{a_w}{a}\right) \qquad (2)$$

$$R \approx \ell/2\pi\sigma\delta a$$

for an implosion driven by discharge of a capacitor C, where L, L_g, R, V are the total inductance, external inductance, discharge resistance, and voltage, respectively, and

$$m_g = \pi a_w^2 \ell \rho_o \tag{3}$$

is the mass of gas in the module. In the formula for the discharge resistance we take δ as the current penetration skin depth, i.e.,

$$\delta = \left(\frac{c^2 t}{4\pi\sigma}\right)^{1/2} + \delta_{flash} \ , \tag{4}$$

where σ is assumed constant and δ_{flash} is the small initial conducting layer thickness associated with the initiating surface breakdown at a_w.

In deriving scaling laws or utilizing computer results it is useful to write these equations in the following dimensionless form:

$$\begin{aligned} &\frac{d}{d\tau}\left((1-A^2)\frac{dA}{d\tau}\right) = -\frac{i^2}{A} \ , \\ &\frac{d^2}{d\tau^2}(\mathcal{L} i) + \frac{d}{d\tau}\left(\frac{ir}{A(\tau^{1/2}+\varepsilon)}\right) + i = 0 \ , \end{aligned} \tag{5}$$

where the dimensionless radius A, current i, and time τ are defined by

$$A = a/a_w, \ i = I/I_o, \ \tau = \omega\tau \ , \tag{6}$$

respectively, and

$$\begin{aligned} &\mathcal{L} = \frac{L}{L_o} = \left(1 - \frac{L_m}{L_g}\frac{\ln A}{\ln(a_w/a_p)}\right)\left(1 + \frac{L_m}{L_g}\right)^{-1} \ , \\ &L_o = L_g + L_m, \ L_m = \frac{2\ell}{c^2}\ln\left(\frac{a_w}{a_p}\right) \ , \\ &\omega = (L_o C)^{-1/2} \ , \\ &I_o = c a_w \omega (m_g/\ell)^{1/2} \ , \\ &r = \frac{2\ell}{c a_w L_o (4\pi\sigma\omega)^{1/2}} \end{aligned} \tag{7}$$

$$\frac{1}{\sigma} = \frac{Z\ell nA}{1.7 \times 10^{14} T_{ev}^{3/2}} + \frac{1}{\sigma_{eo}} \quad ,$$

where σ_{eo}^{-1} is the contribution to the resistivity from electron-neutral scattering.

The initial conditions at $\tau = 0$ are

$$A = 1 - \frac{\delta_{flash}}{a_w} \approx 1, \; i = 0, \; \frac{dA}{d\tau} = 0 \; ,$$
$$\left(\frac{di}{d\tau}\right)_{\tau=0} = \frac{V_o}{L_g I_o \omega} = \frac{(2C\ell)^{1/2}}{a_w} \left(1 + \frac{L_m}{L_g}\right)\left(\frac{\frac{1}{2}CV_o^2}{\pi a_w^2 \rho_o c^2 \ell}\right)^{1/2} . \qquad (8)$$

Solutions are insensitive to the initial thin flash-over layer δ_{flash} which appears in both the initial value of A and also in the initial resistance.

Numerical solutions to Eq. (5) are presented in Figures 31-36 for a range of parameters. Figure 31 plots $A(\tau)$, $-\frac{dA}{d\tau}(\tau)$, and $i(\tau)$ for the standard set of parameters shown in Table 1. For simplicity, we assume that the resistance r is constant throughout the implosion. Unlike the examples shown in Ref. (1), there has been no attempt to "match" the implosions by choosing $\frac{di}{d\tau}(\tau=0)$ so that $i(\tau = \tau_{imp}) \approx 0$. (The implosion time τ_{imp} is the time at which $A(\tau) = a_p/a_w$.) The qualitative features of Figure 31 are reproduced over a very broad range of parameters. In the remaining examples, one of the quantities listed in Table 1 has been varied while holding the others constant.

A major factor in determining the behavior of the imploding plasma is the dimensionless initial current rise $\frac{di}{d\tau}(0)$. As can be seen from Eq. (8), this quantity can be readily varied by changing the gas density ρ_o. Figure 32 shows some of the effects of varying the current rise. As $\frac{di}{d\tau}(0)$ increases,

Table 1

Standard Parameters for
Implosion Calculations
(Dimensionless)

Quantity	Value
Inductance Ratio: L_m/L_g	3
Projectile radius: a_p/a_w	0.2
Resistance: r	0.01
Initial resistance: ε	0.01
Flashover width: δ_{flash}	10^{-4}
Current rise rate: $\frac{di(0)}{d\tau}$	1.9

both the current $i(\tau_{imp})$ and efficiency ε_{imp} at $\tau = \tau_{imp}$ increase steadily. The efficiency for transfer of electrical energy to implosion kinetic energy was shwon in Ref. 1 to be

$$\varepsilon_{imp} = \left[\frac{(dA/d\tau)_{imp}}{\frac{di}{d\tau}(0)}\right]^2 \frac{\left(\frac{L_m}{L_g}\right)\left(1+\frac{L_m}{L_g}\right)}{2(1-f)\,\ell n\left(\frac{a_w}{a_p}\right)} \qquad (9)$$

where f is the fraction of energy stored in the capacitor bank at the end of the implosion. Projectile stability considerations[1] require that $\frac{dP}{da}(\tau=\tau_{imp}) < 0$ where P is the radially-directed momentum per radian of the plasma annulus. This means that the speed of the implosion must be decreasing as $\tau \to \tau_{imp}$, or $\frac{d^2A}{d\tau^2} < 0$. Figure 32 demonstrates that the stabilizing force on the projectile is lost for $\frac{di}{d\tau}(0) > 2.0$. A more complete discussion of this point will be given later in this section.

The implosion time and implosion velocity are weakly dependent on $\frac{di}{d\tau}(0)$, as shown in Figure 33. As one would expect, a steeper rise in the current shortens the implosion time and increases the implosion velocity.

Figure 34 plots $\frac{dA}{d\tau}(\tau_{imp})$ and $i(\tau_{imp})$ as functions of the dimensionless resistance r. Unlike other quantities which we have varied, the plasma resistance is not actually a directly controllable parameter. For simplicity, we have assumed that it is constant, neglecting its complex dependence on plasma temperature and the degree of ionization. Increasing the resistance lowers the current and implosion velocity (and hence efficiency) although some of the energy may be recovered in the form of I^2R heating of the plasma.

The ratio a_p/a_w of the projectile radius to the wall radius is an easily varied parameter which is expected to change as the local projectile velocity changes. Figure 35 plots τ_{imp}, $-\frac{dA}{d\tau}(\tau_{imp})$, and $i(\tau_{imp})$ as functions of a_p/a_w. The inductance ratio and initial current rise rate have been held constant, so some of the apparent loss in implosion velocity and efficiency, as a_p/a_w increases, could be recovered by decreasing $\frac{di}{d\tau}(0)$.

Figure 36 illustrates the tradeoff between efficiency and projectile stability which was briefly discussed in connection with Figure 32. As discussed in Ref. 1, the projectile will tend to be stabilized against radial displacements if the implosion speed is decreasing as $\tau \to \tau_{imp}$. This condition is achieved in Figure 36 for $\frac{di}{d\tau}(0) = 1.6$. The thermal pressure term which was omitted from the right hand side of Eq. (5) will further decelerate the plasma. However, for $\frac{di}{d\tau}(0) = 2.1$, the implosion kinetic energy is higher, but the implosion velocity continues to increase

with τ, so there may be a complete loss of projectile stability. It seems clear that projectile stability may be an important limiting factor for implosion velocity and efficiency.

REFERENCES

1. D. A. Tidman and S. A. Goldstein, J. Appl. Phys. 51, 1975 (1980).

2. Proceedings of the Impact Fusion Workshop, LASL Report 8000-C (1979).

3. S. A. Goldstein, F. Sandel, D. A. Tidman, D. Massey, The MAID System, Data Base and Design Issues, Proceedings Conference on EM Guns and Launchers, November 4-6, 1980, San Diego, CA (sponsored by ARRADCOM/DARPA).

4. D. A. Tidman, Applications of Rep-Ratable Mass Accelerators (such as MAID). Proceedings Conference on EM Guns and Launchers, November 4-6, 1980, San Diego, CA (sponsored by ARRADCOM/DARPA).

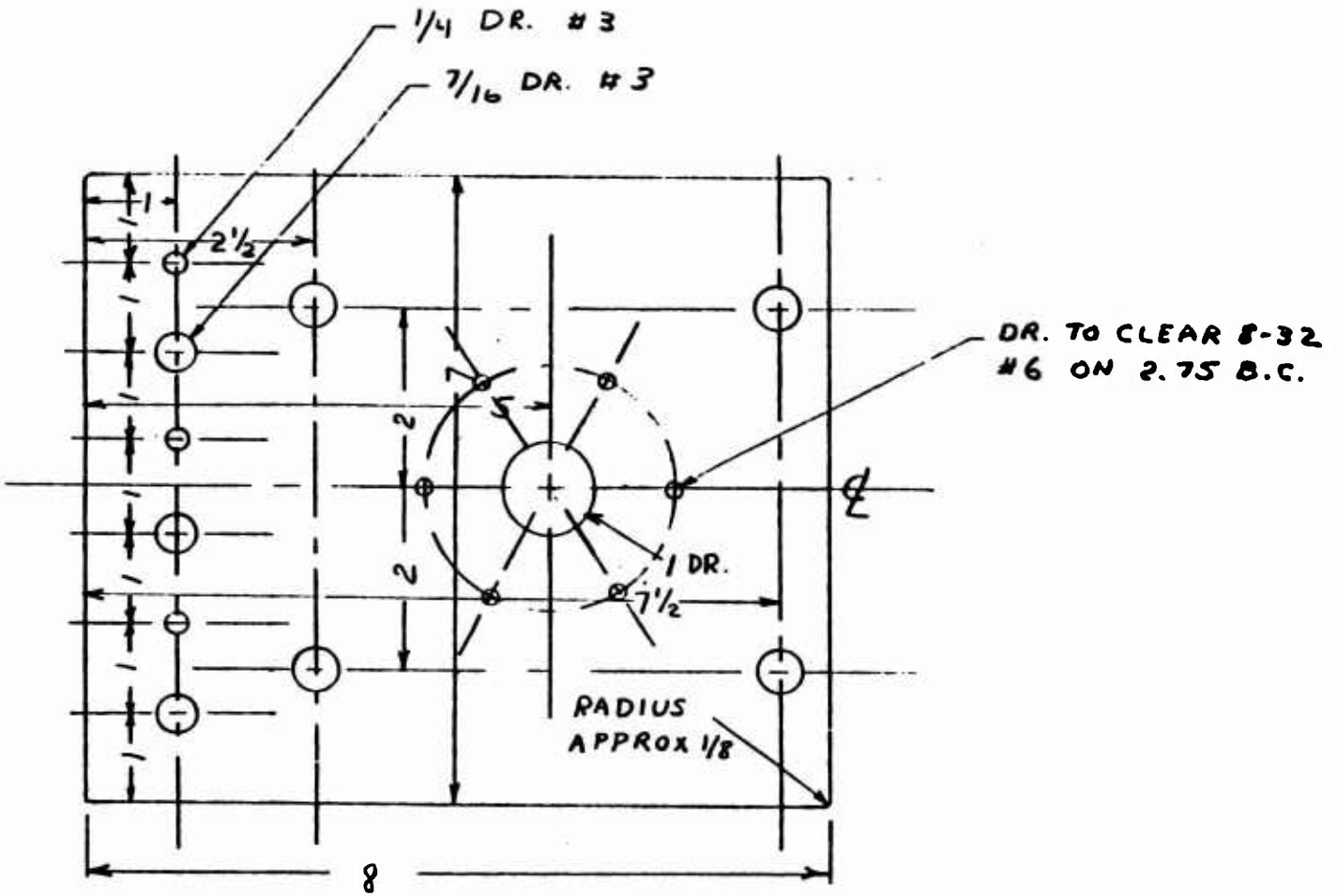

Figure 1. Inner Collector Plate
Scale: one half
Mat: 1/16 brass

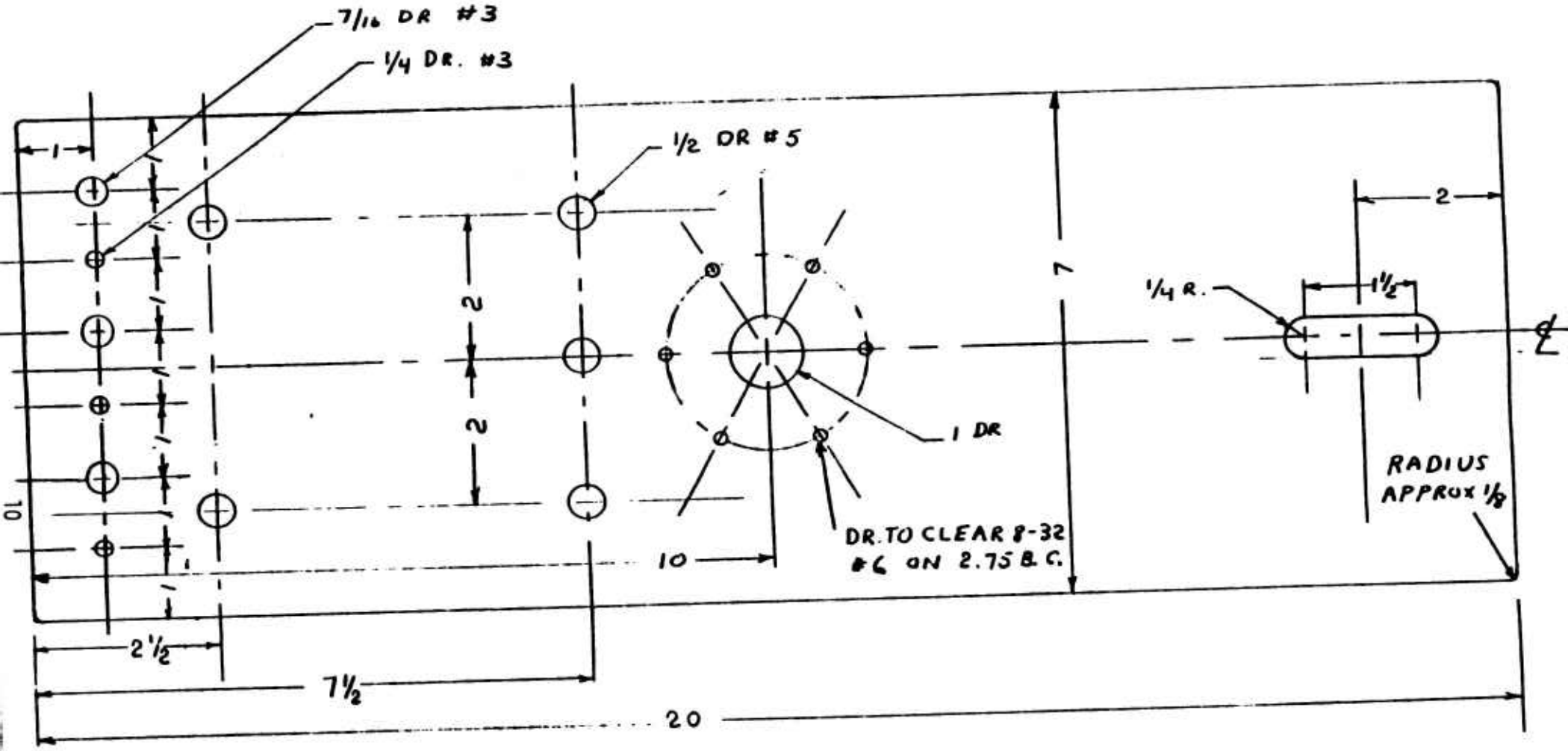

Figure 2. Outer Collector Plate
Scale: one half
Mat: 1/16 brass

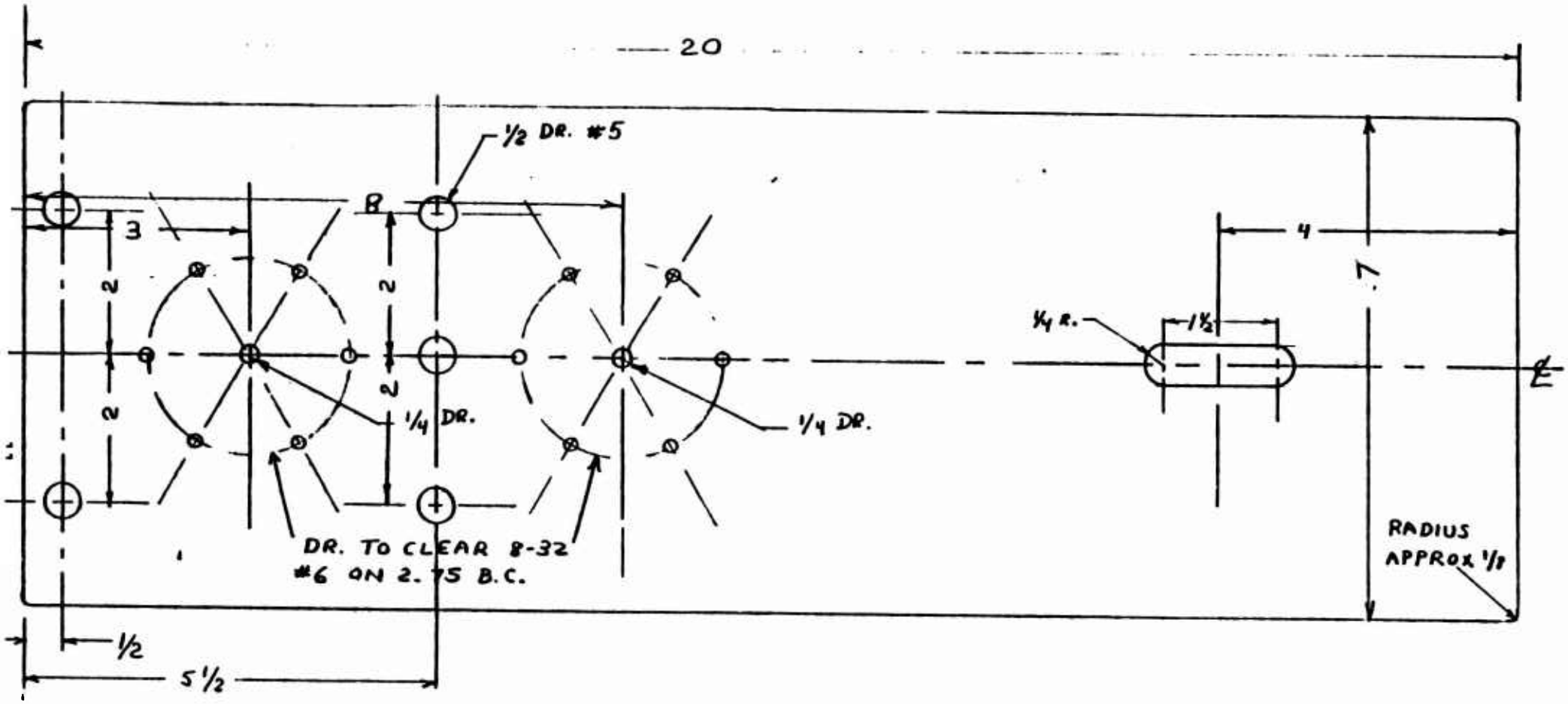

Figure 3. Middle Collector Plate
Scale: one half
Mat: 1/16 brass

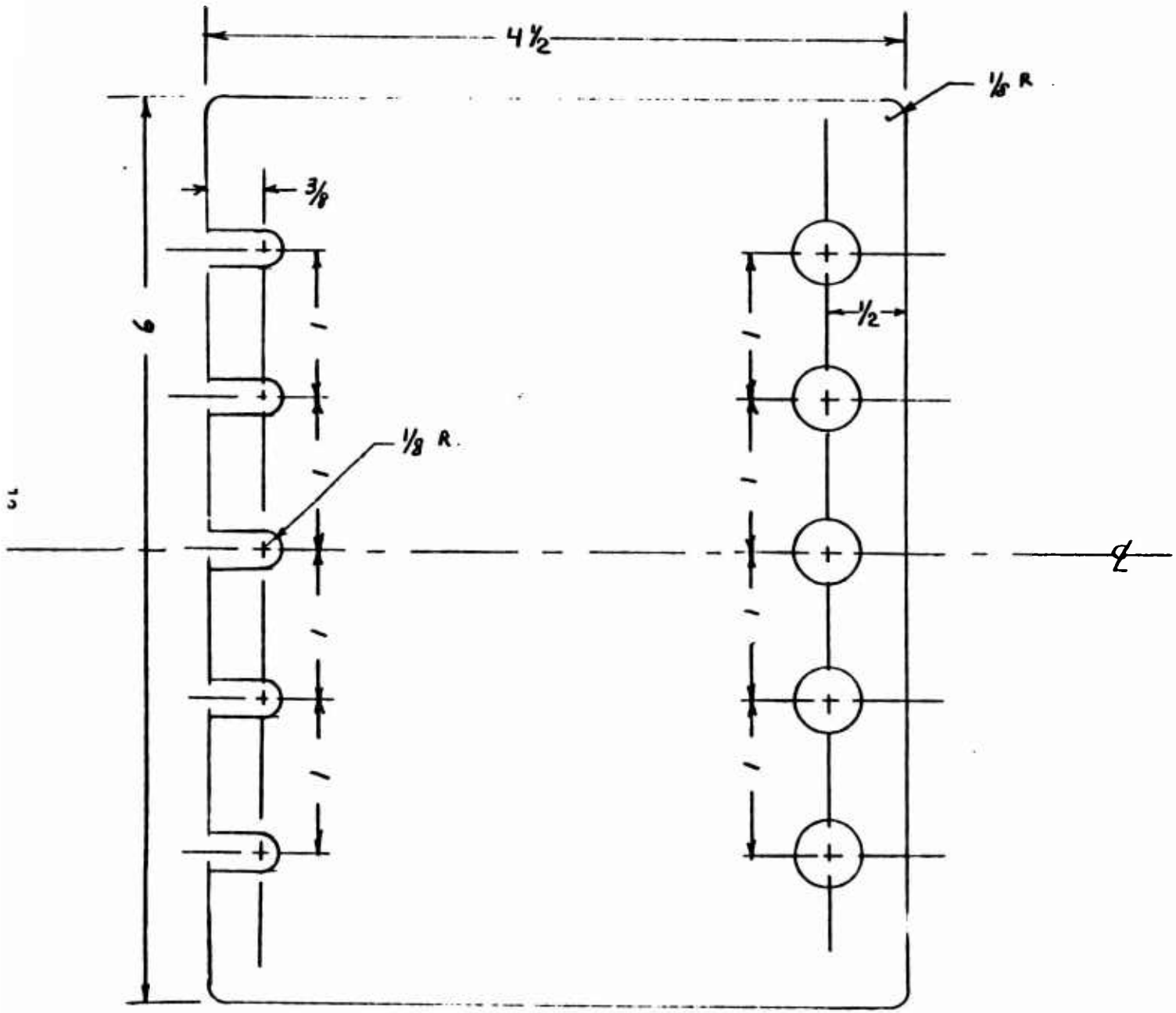

Figure 4. Module Feed Plate
Scale: full size
Mat: 1/16 brass

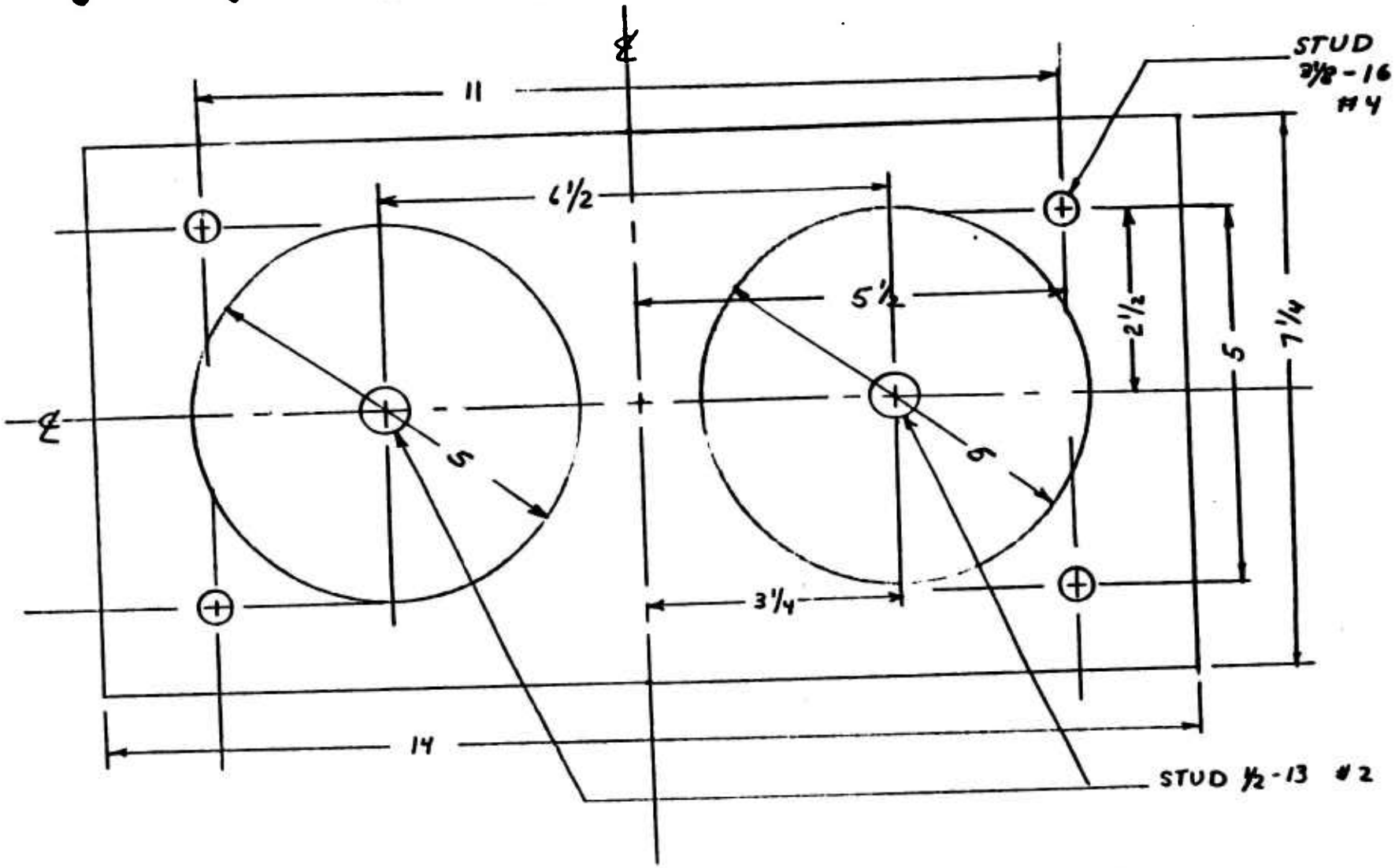

Figure 5. Capacitor Layout
Scale: one half
Capacitor: Aerovox Type No. PX80D18
29 μf, 20 kV, 5.8 kJ

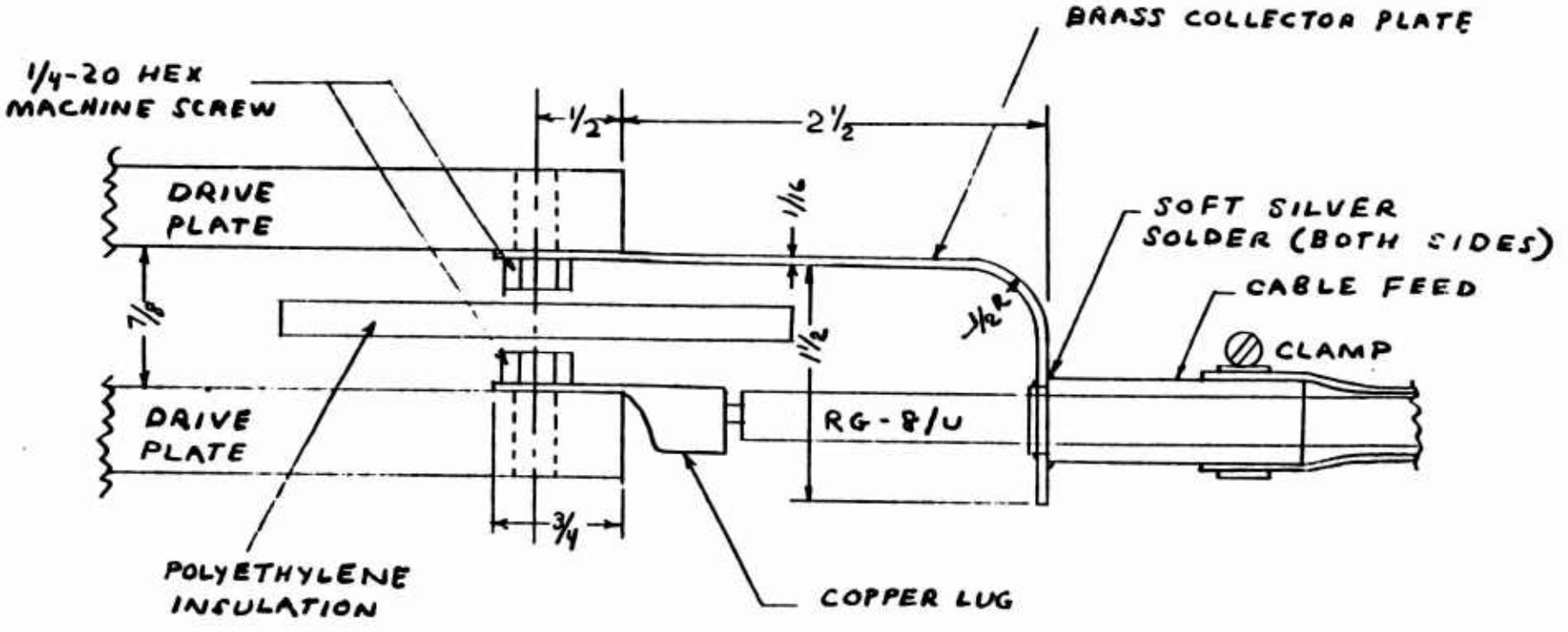

Figure 6. Module Cable Feed Assembly
Scale: full size

Figure 7

Conceptual Design

- bipolar collector plates
- cable connections
- trigger switch
- crowbar switch

Scale: one half

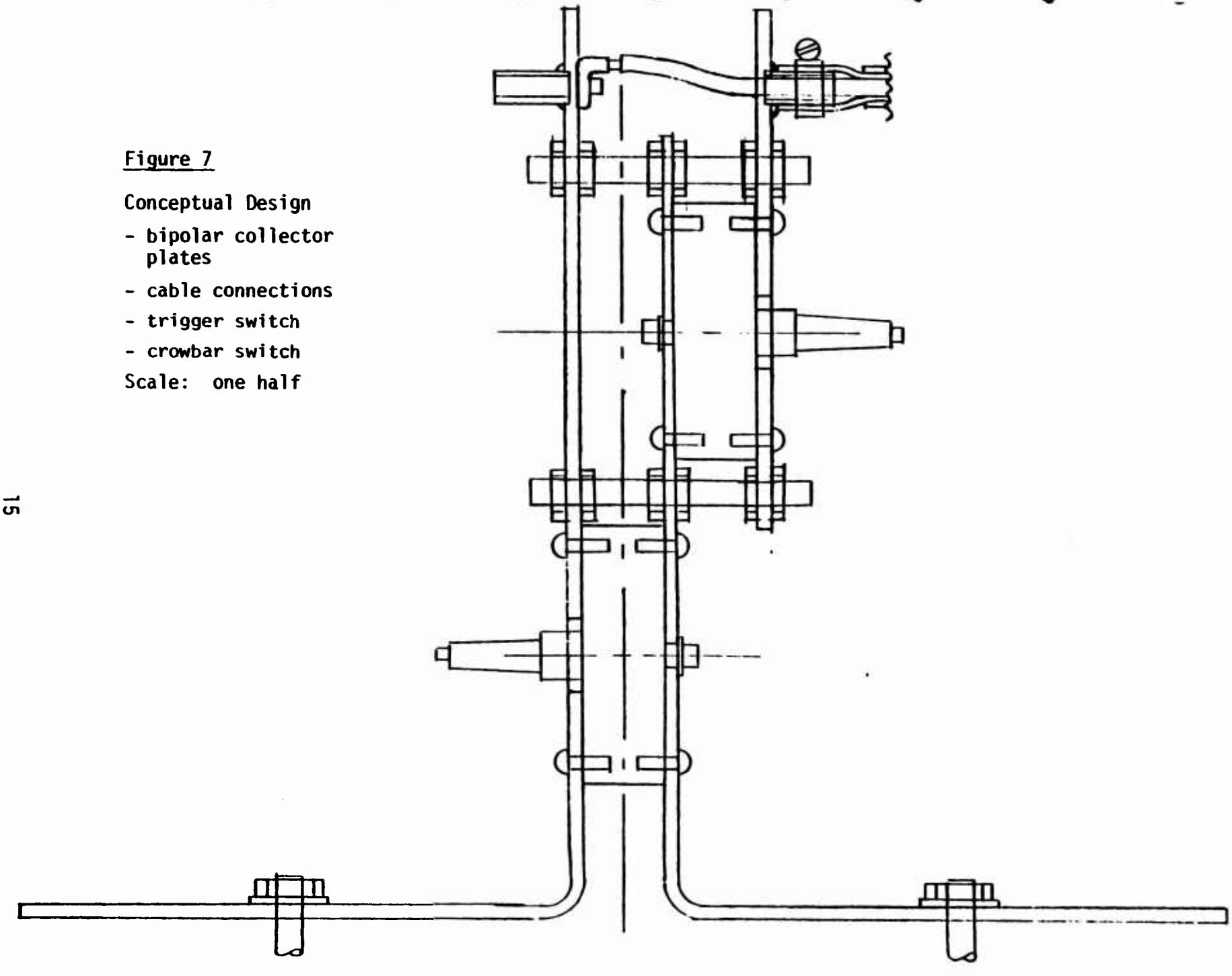

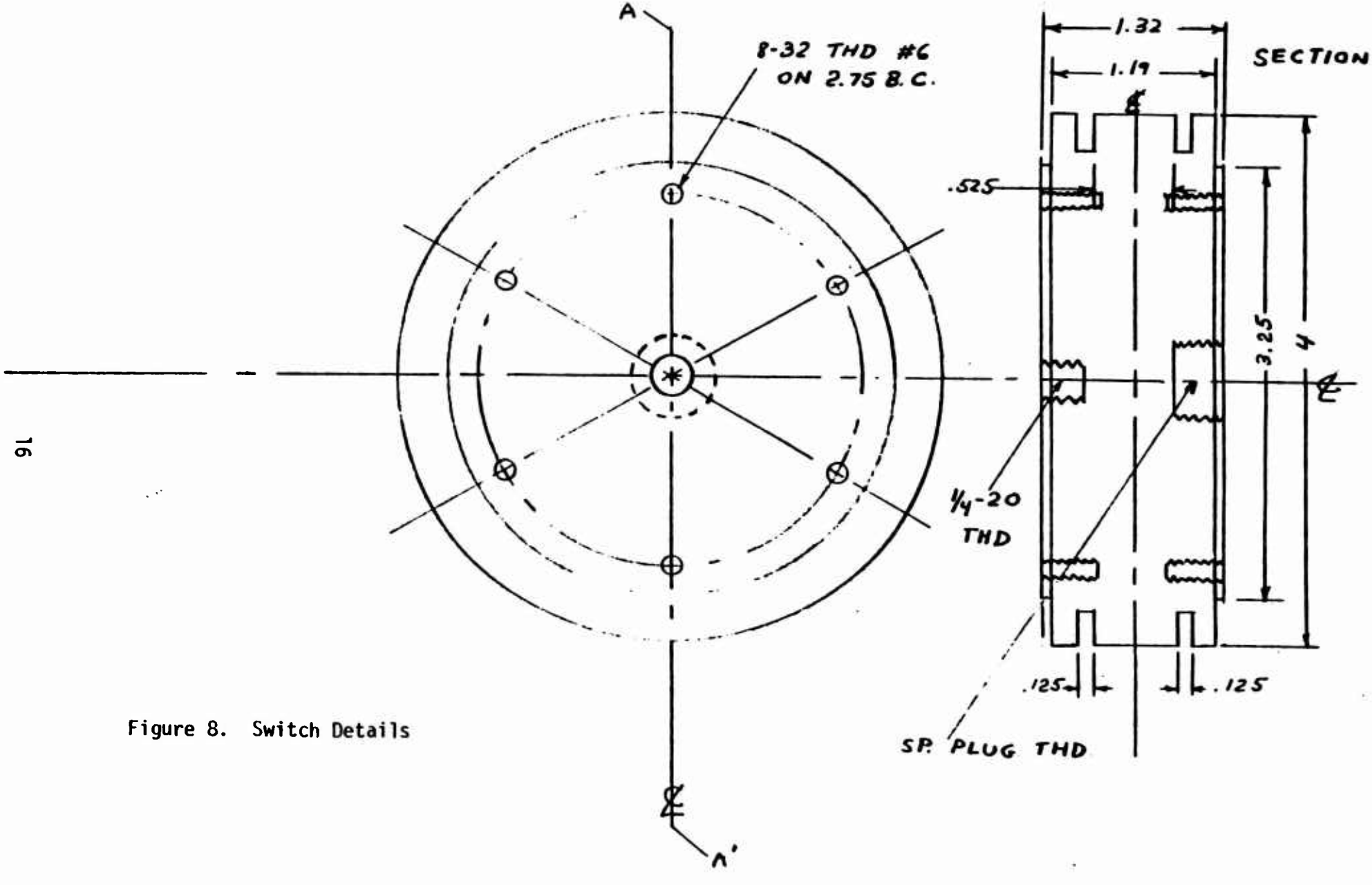

Figure 8. Switch Details

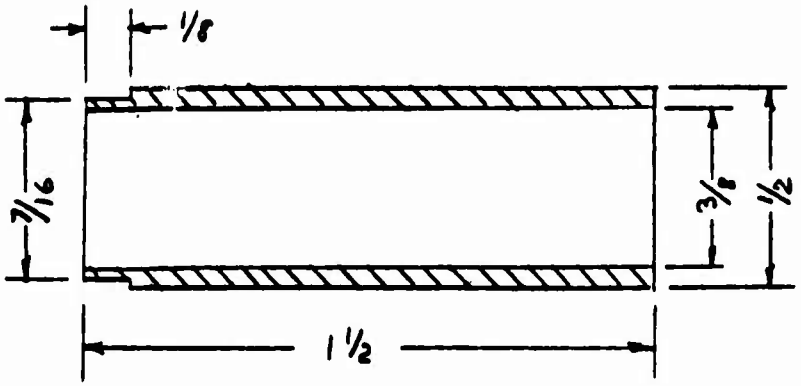

Figure 9. Cable Feed
Scale: 2:1
Mat: brass tubing

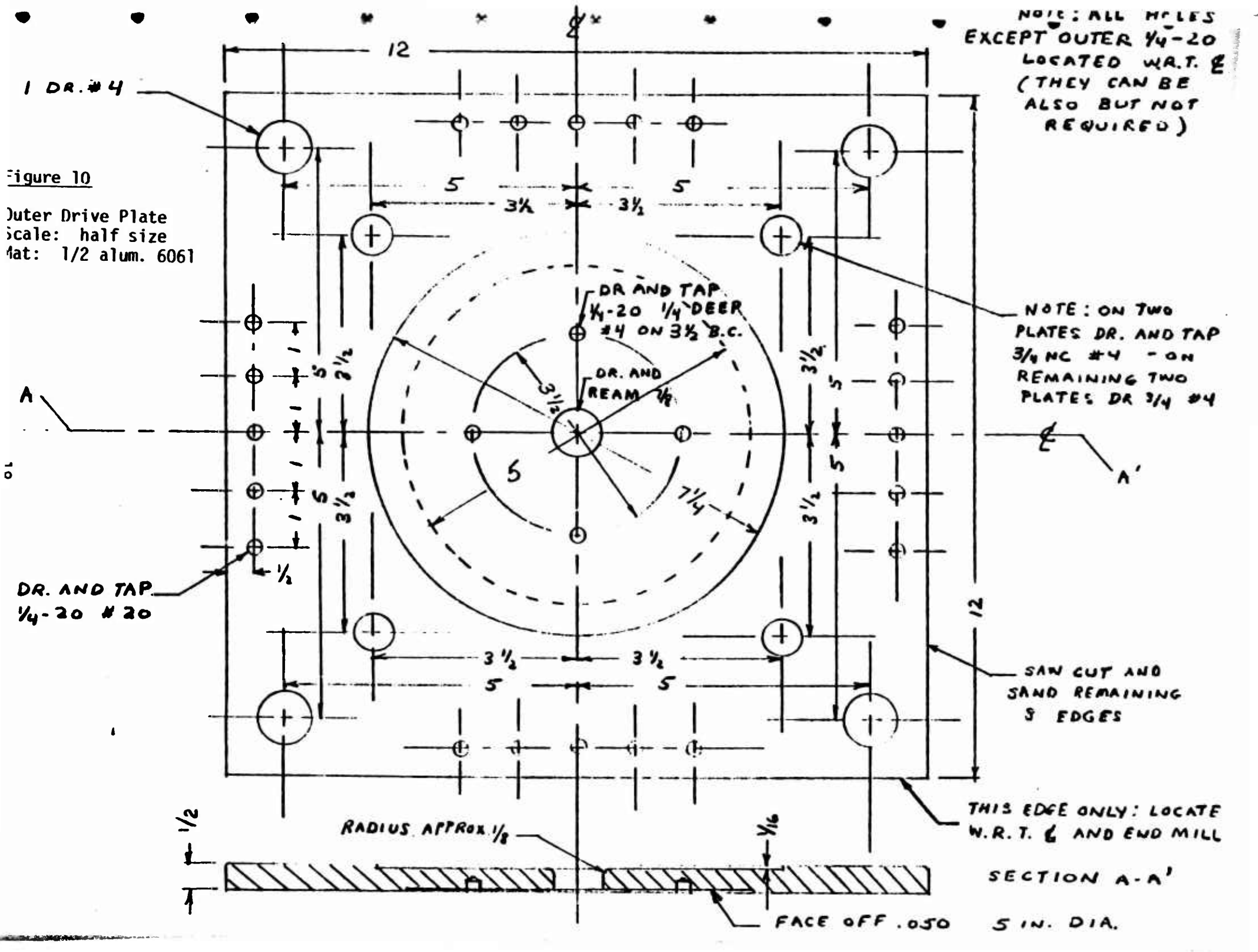

Figure 10

Outer Drive Plate
Scale: half size
Mat: 1/2 alum. 6061

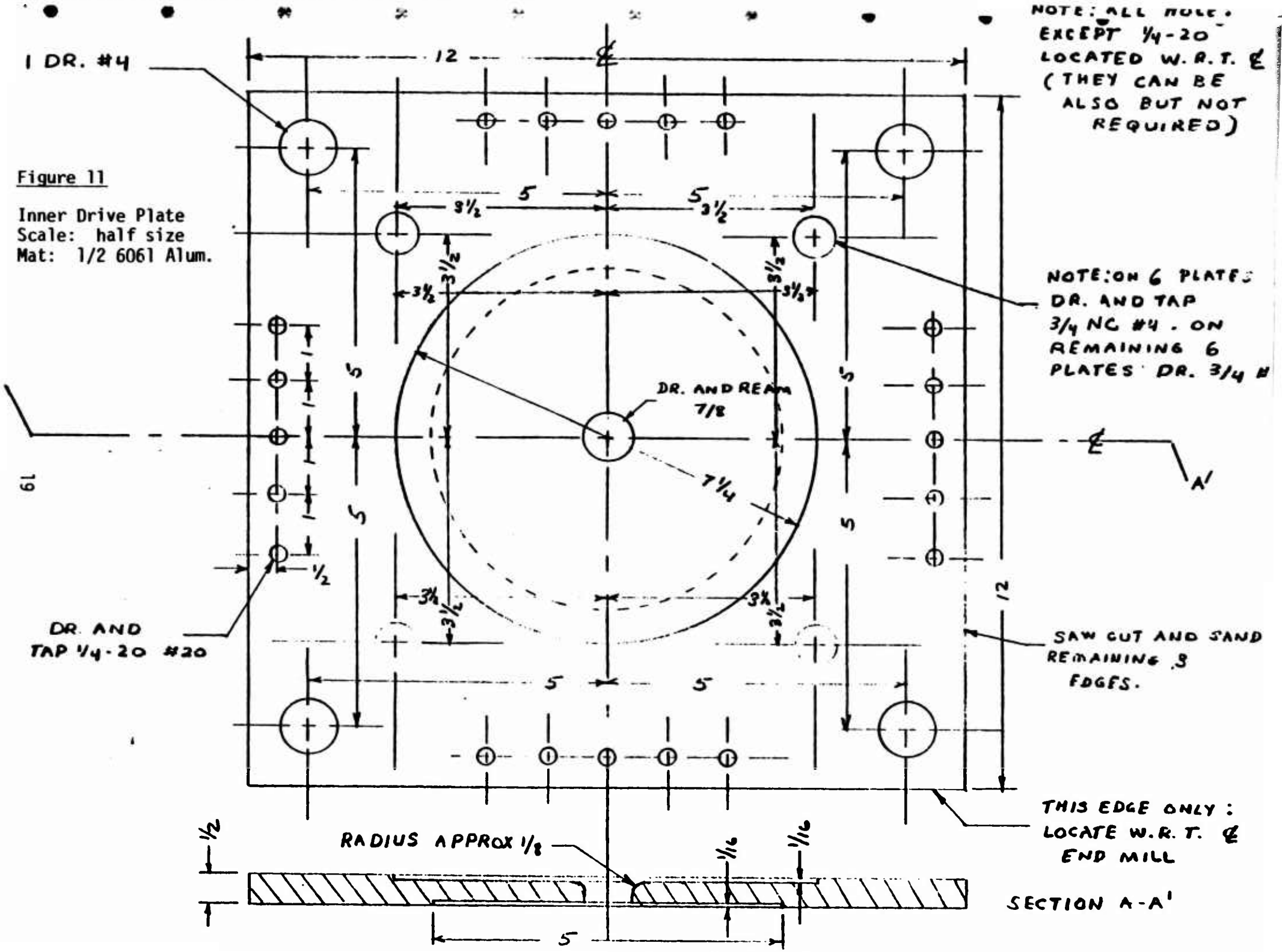

Figure 11

Inner Drive Plate
Scale: half size
Mat: 1/2 6061 Alum.

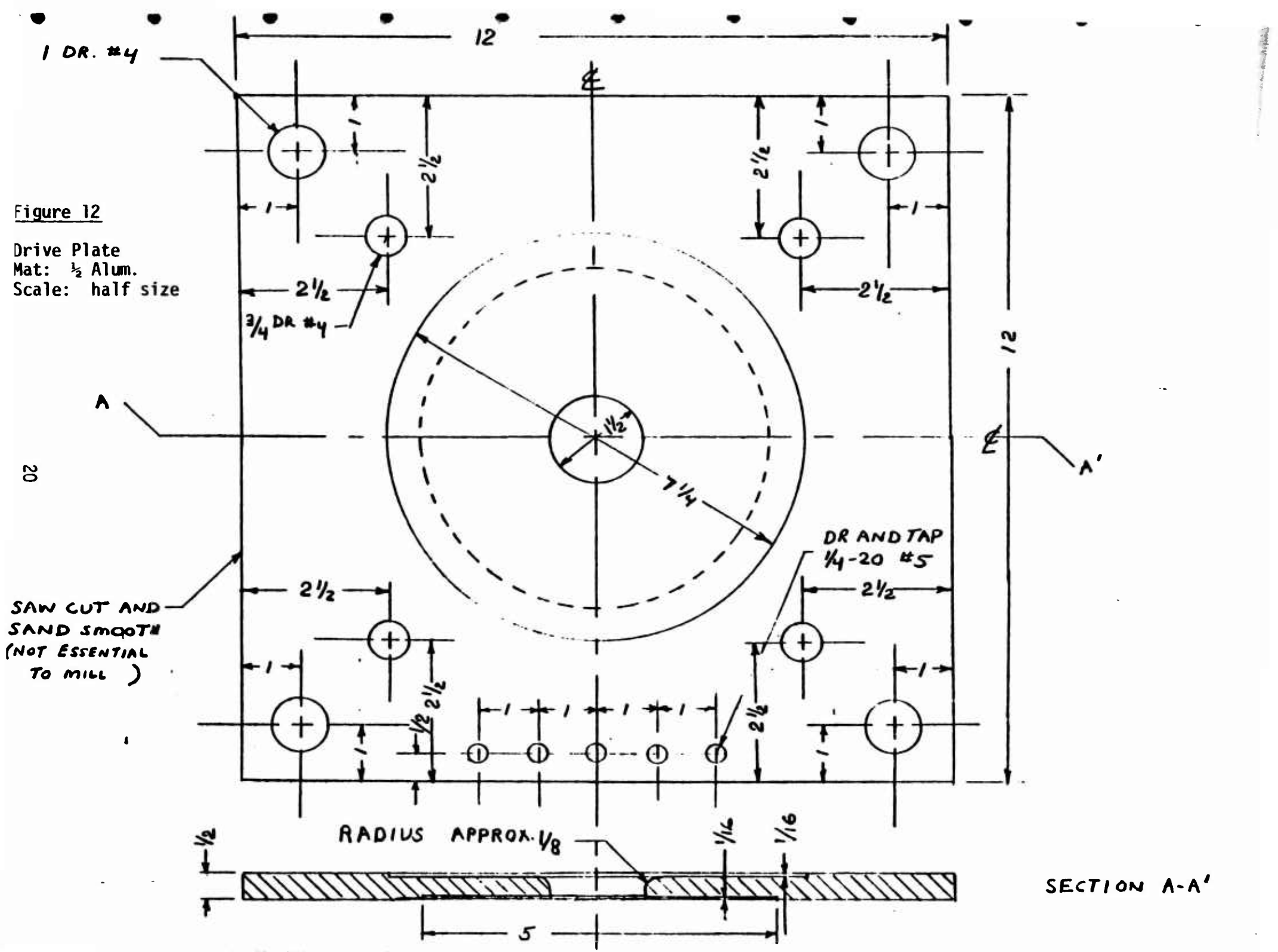

Figure 12

Drive Plate
Mat: ½ Alum.
Scale: half size

SECTION A-A'

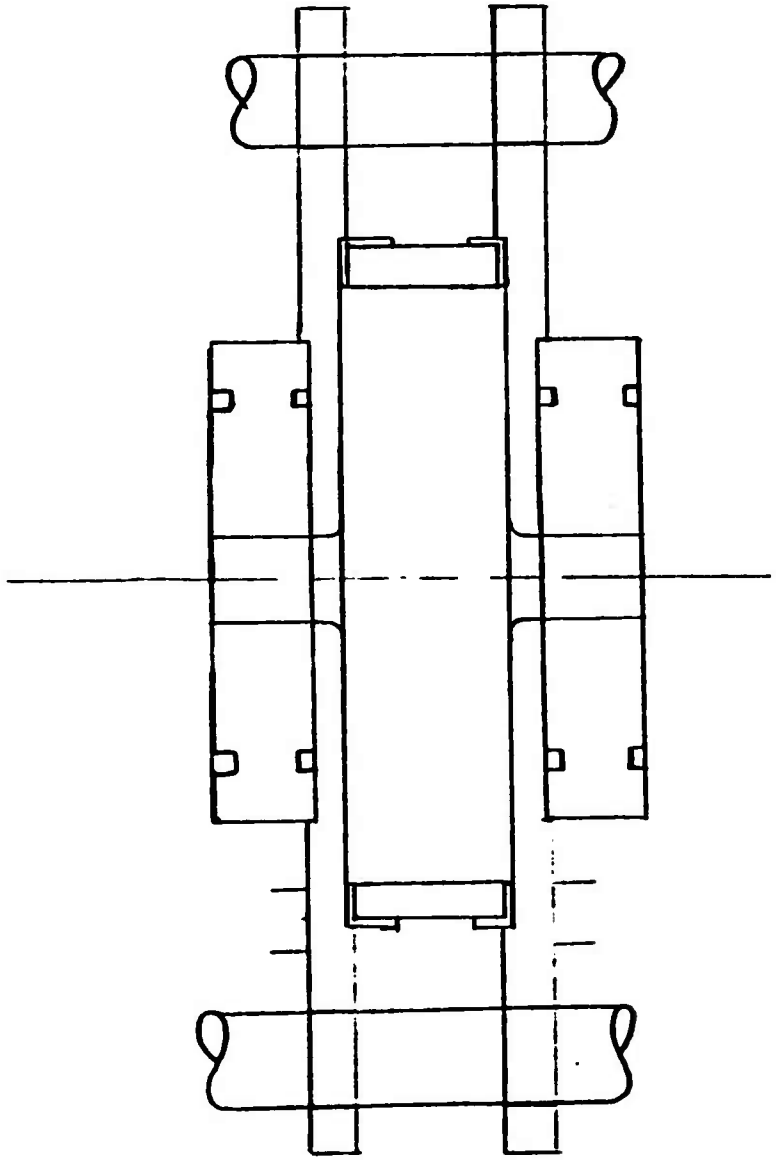

Figure 13. Intermodule Assembly
Scale: one half
(approx.)

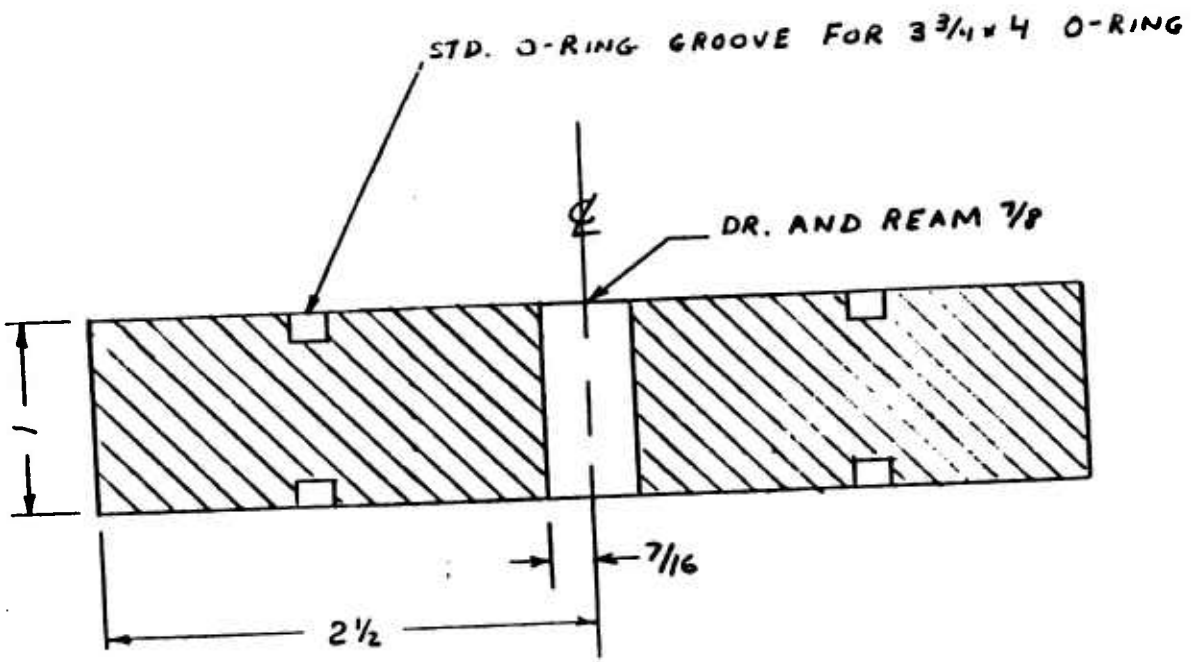

Figure 14. Intermodule Spacer
Scale: full size
Mat: lucite

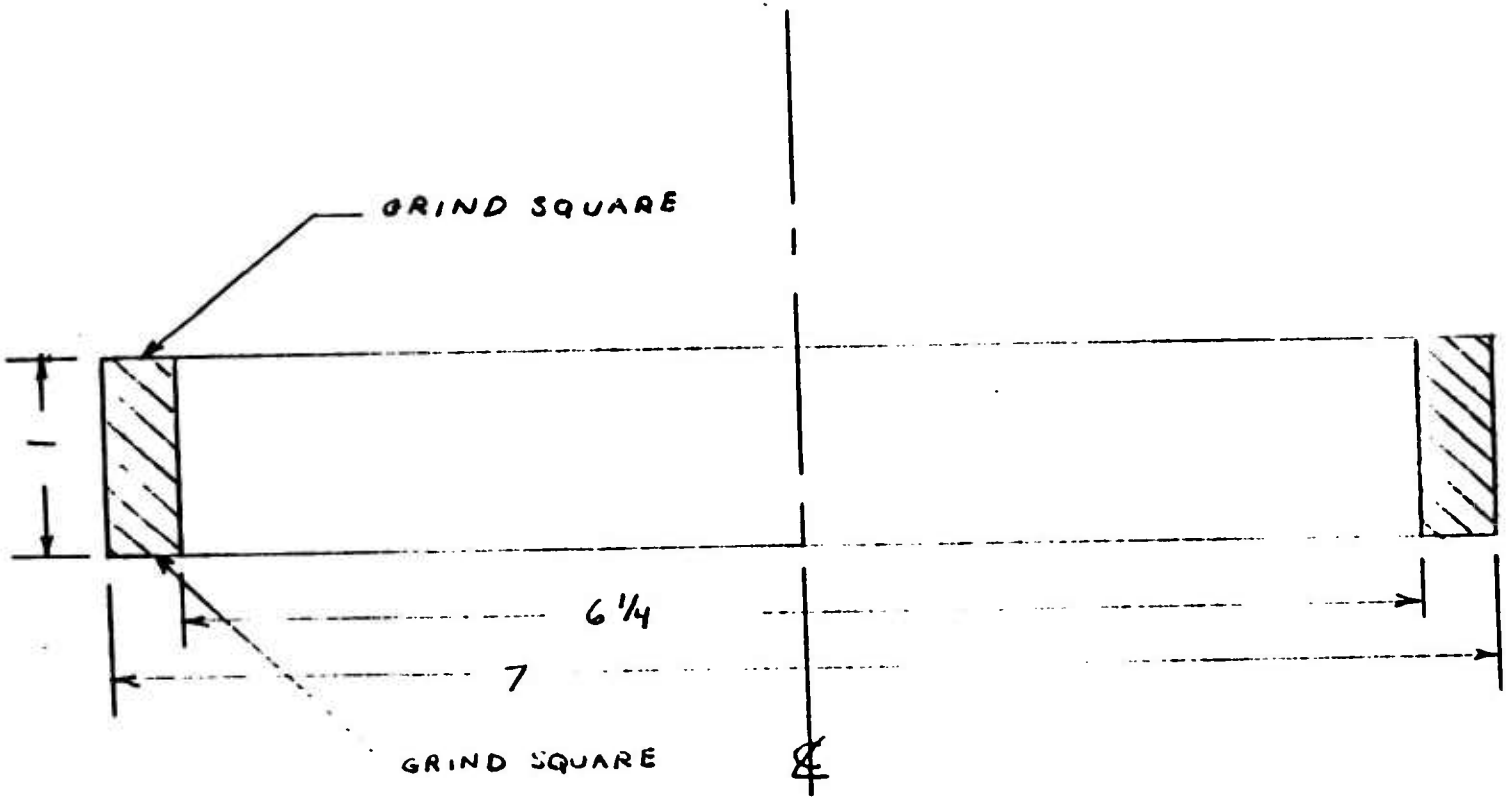

Figure 15. Launch Wall
Scale: full size
Mat: Pyrex

For smaller module radii use thicker lucite wall. Azimuthal sharp breakdown ring at inner edge of launch wall may also also be used to assist in implosion symmetry.

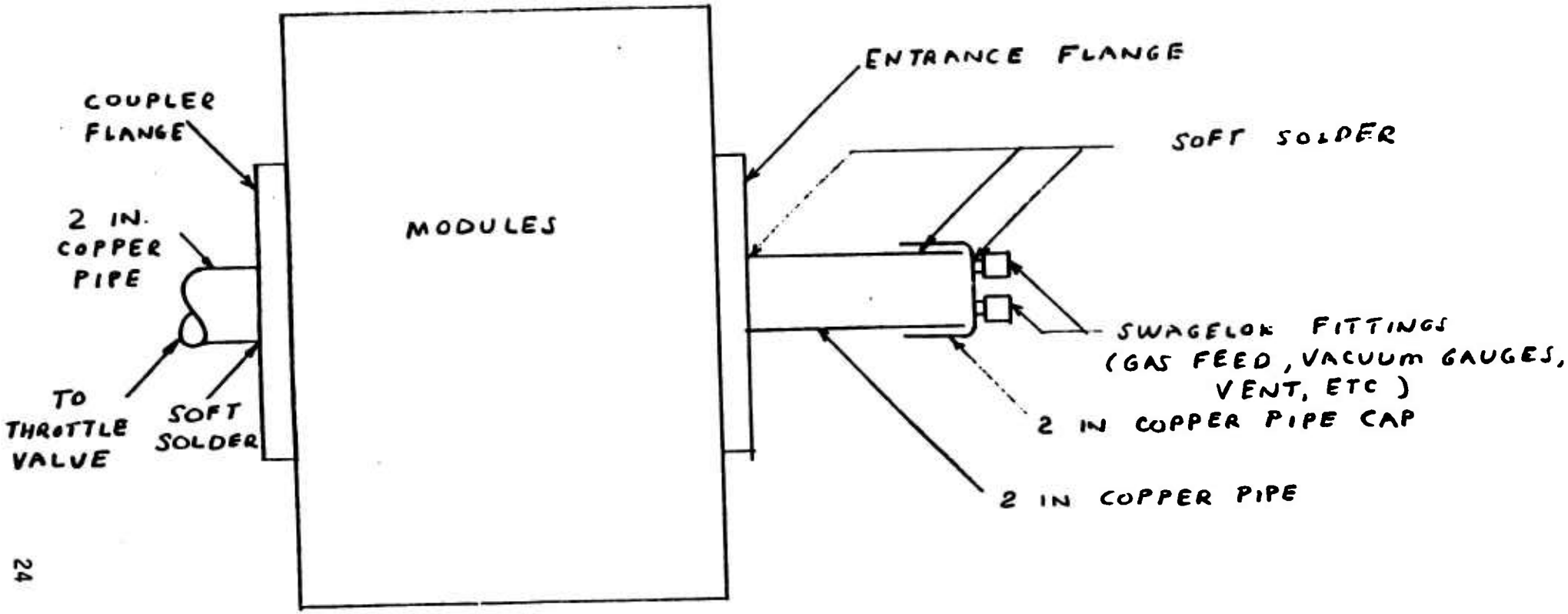

Figure 16. Vacuum Connections

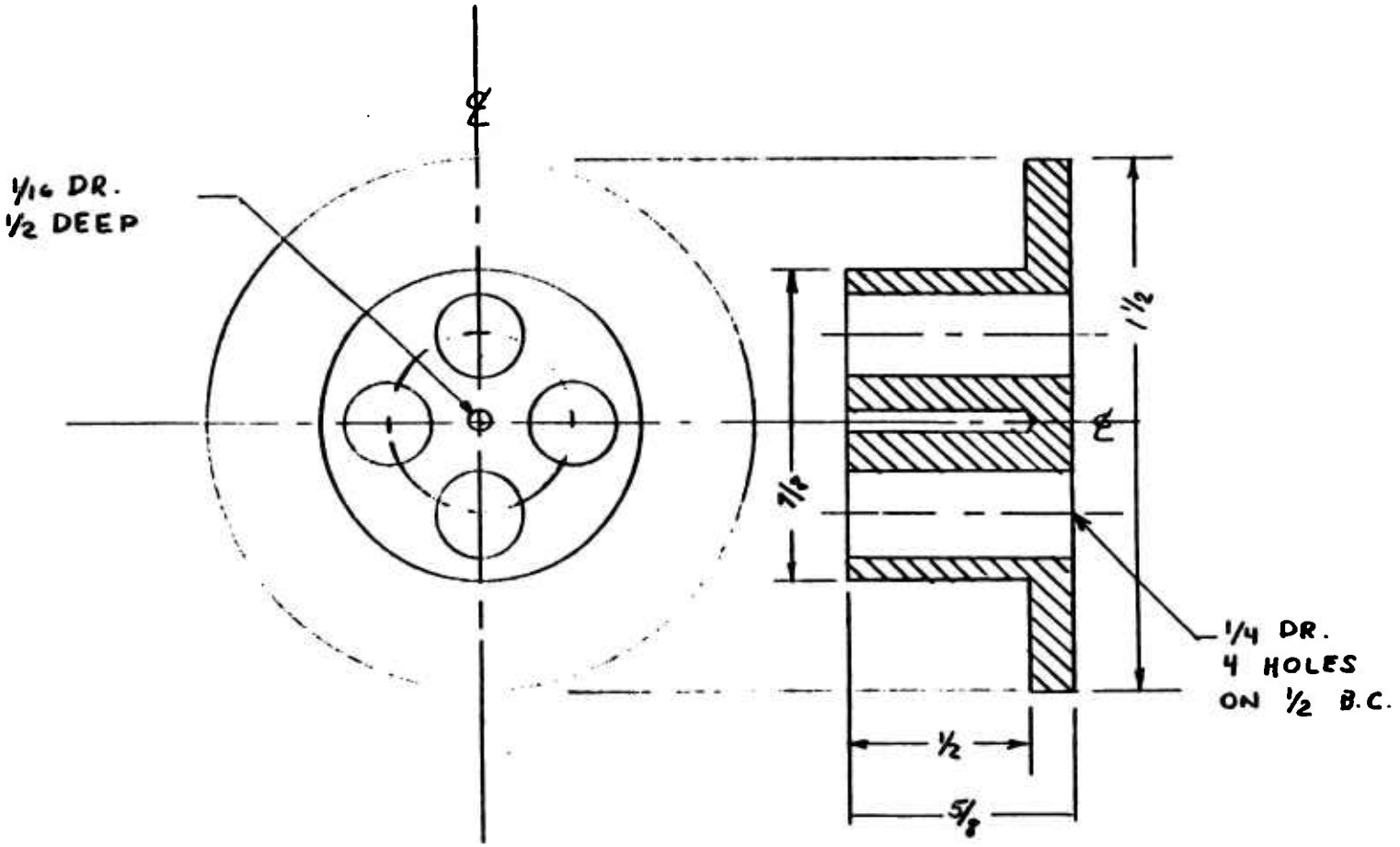

Figure 17. Projectile Support
Scale: 2:1
Mat: Alum.

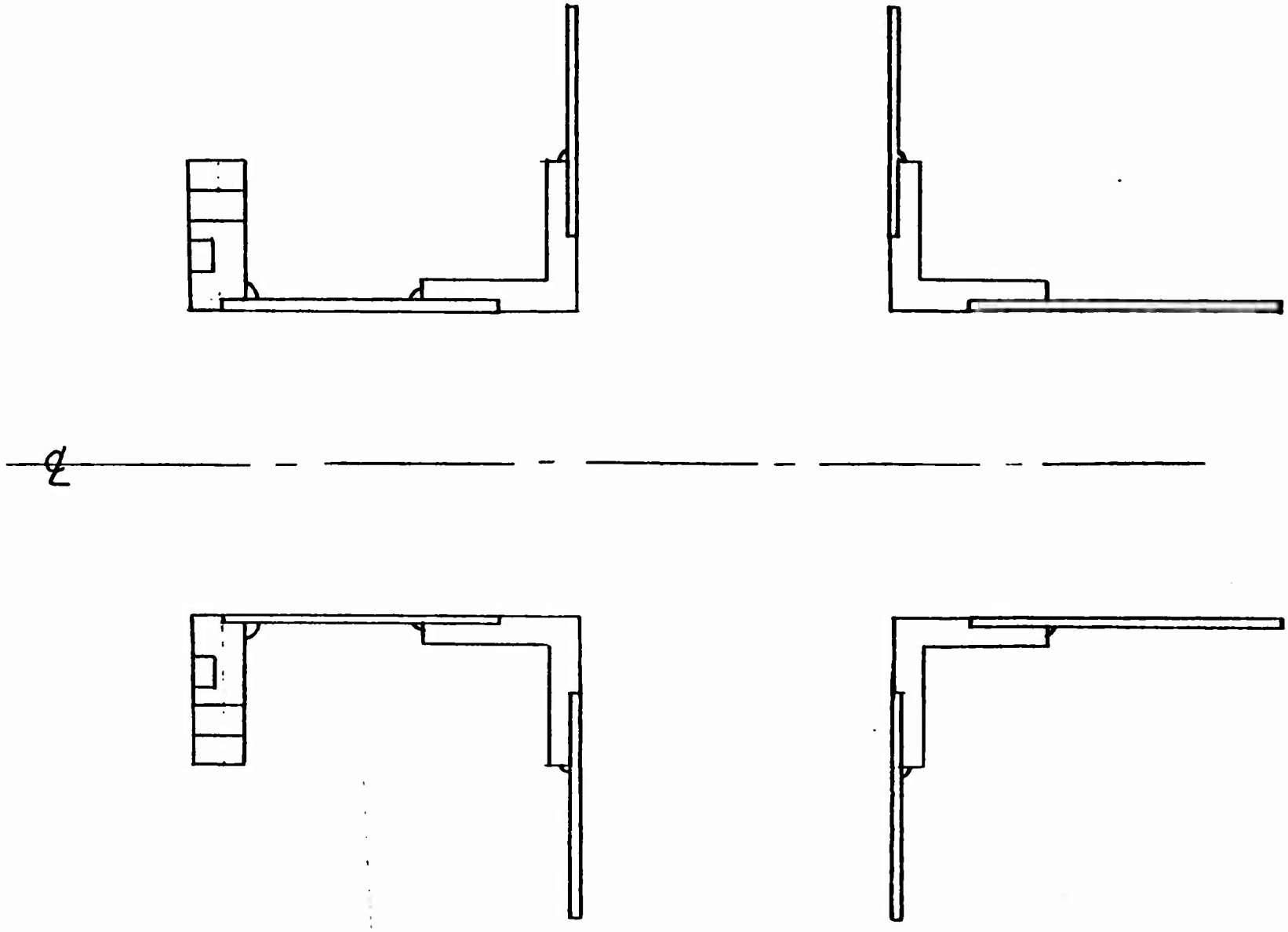

Figure 18. Coupling Assembly
Scale: full size
Mat: brass

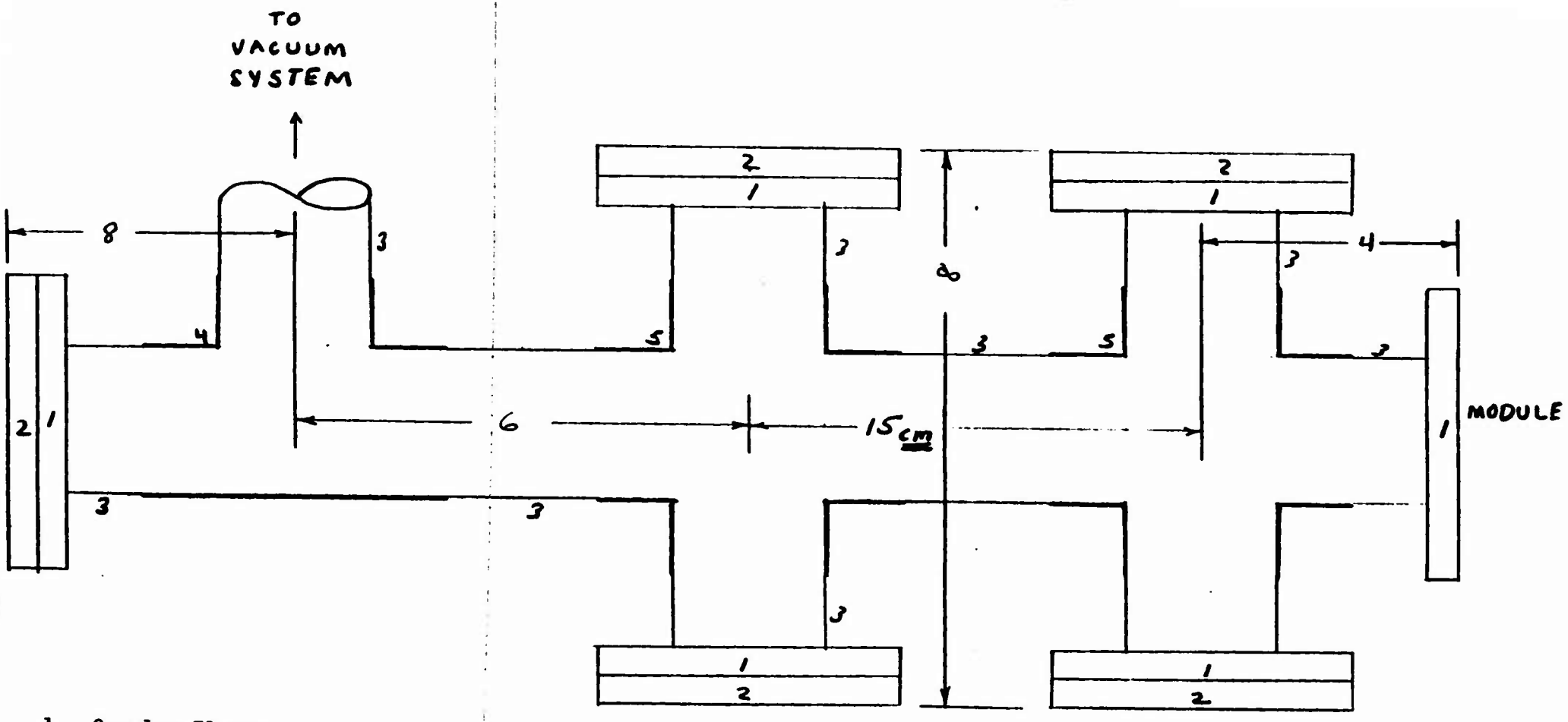

Figure 19. Diagnostic Exit Part Assembly (not to scale)

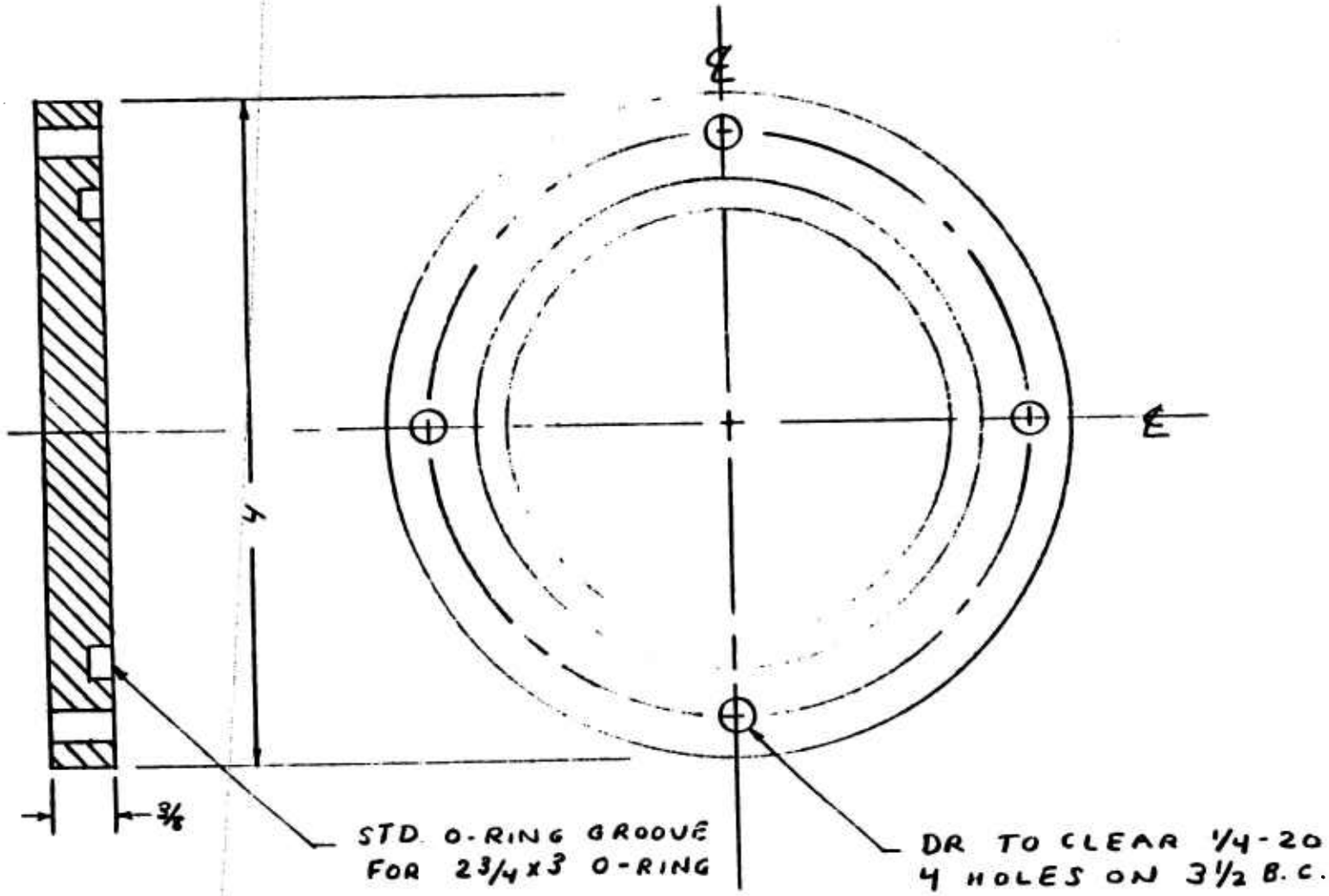

Figure 20. Blankoff Flange for Module Pumpdown and Testing
Scale: full size
Mat: Brass

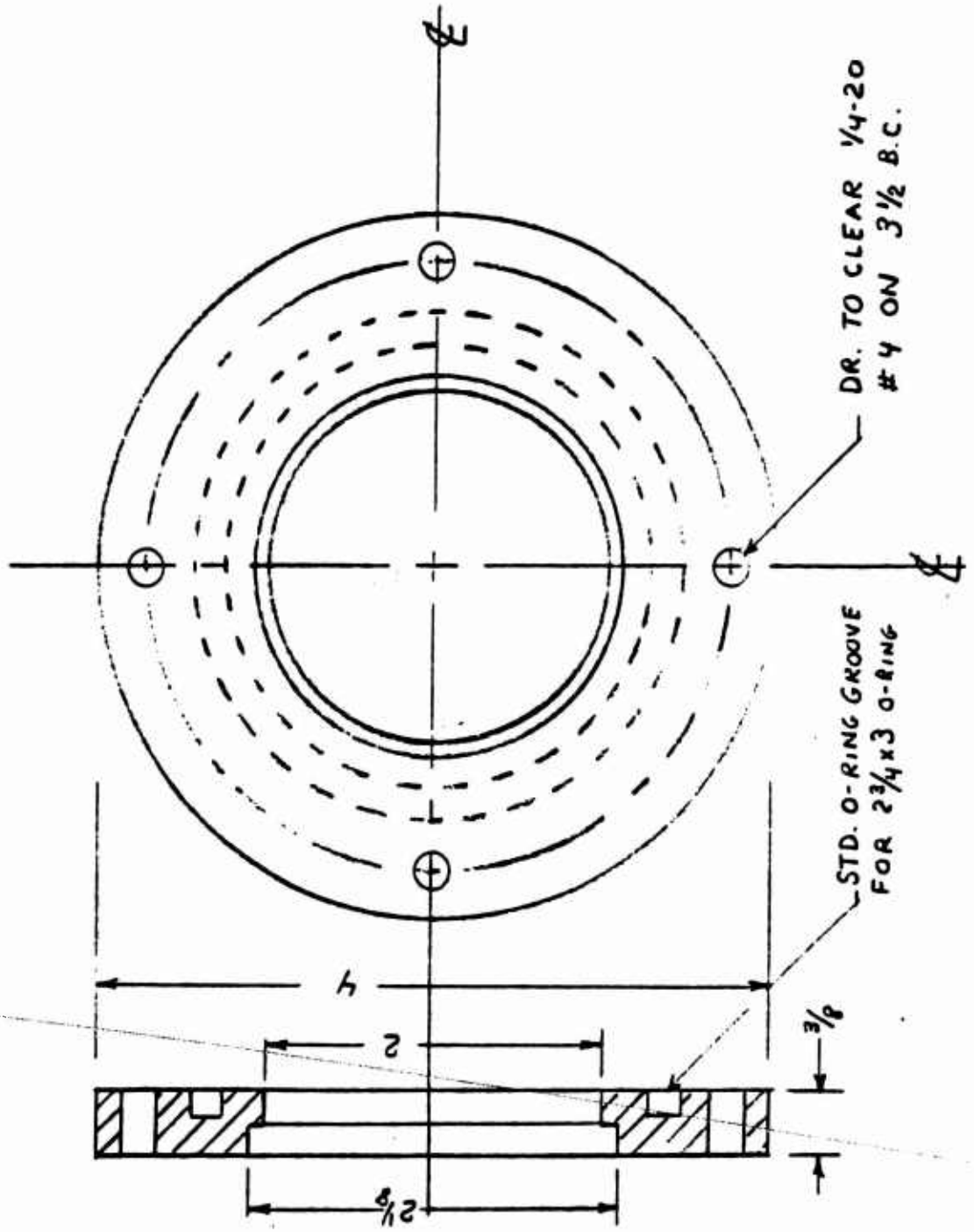

Figure 21. Coupler Flange
Scale: full size
Mat: brass

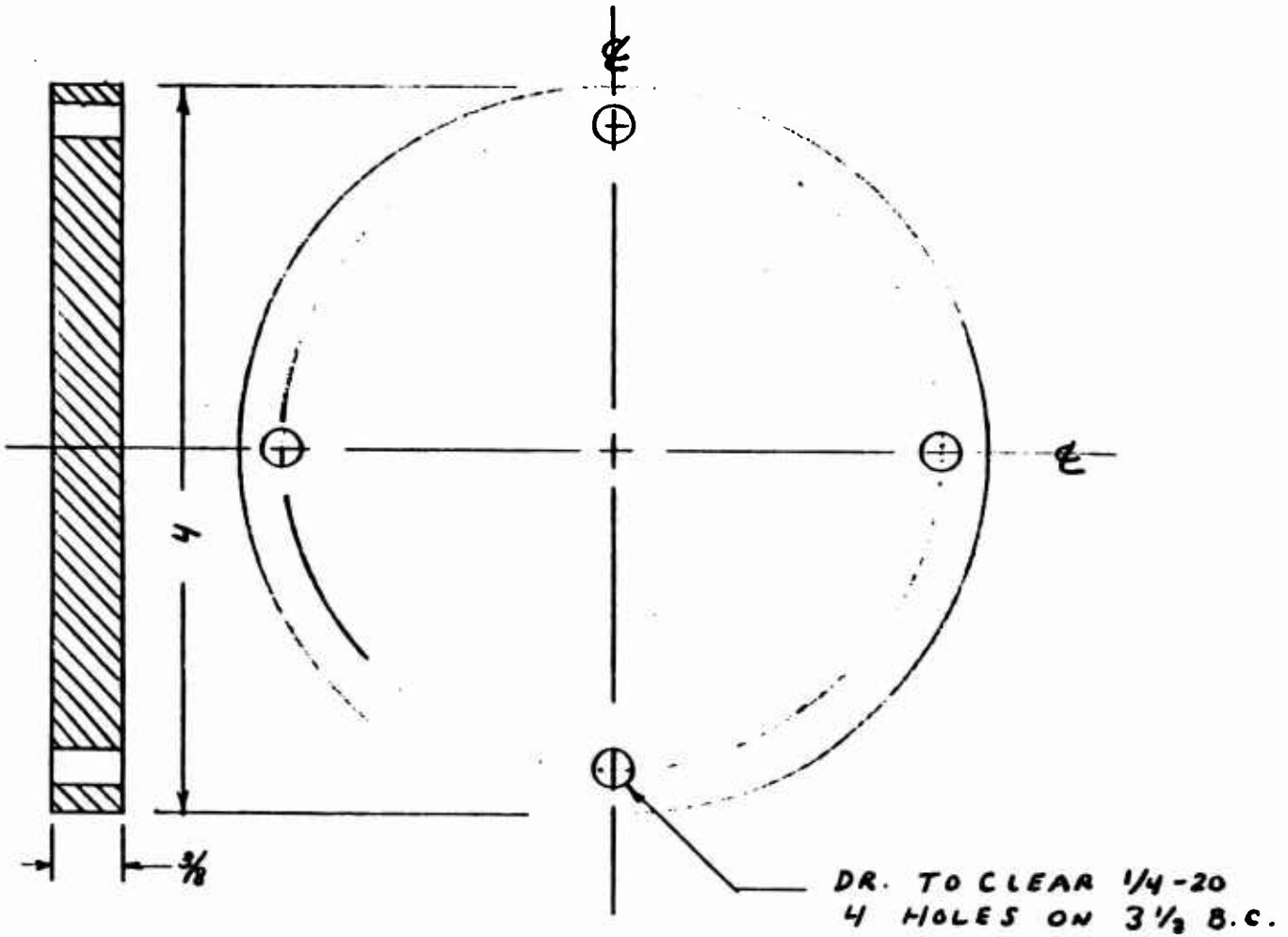

Figure 22. Blank Flange
Scale: full size
Mat: brass

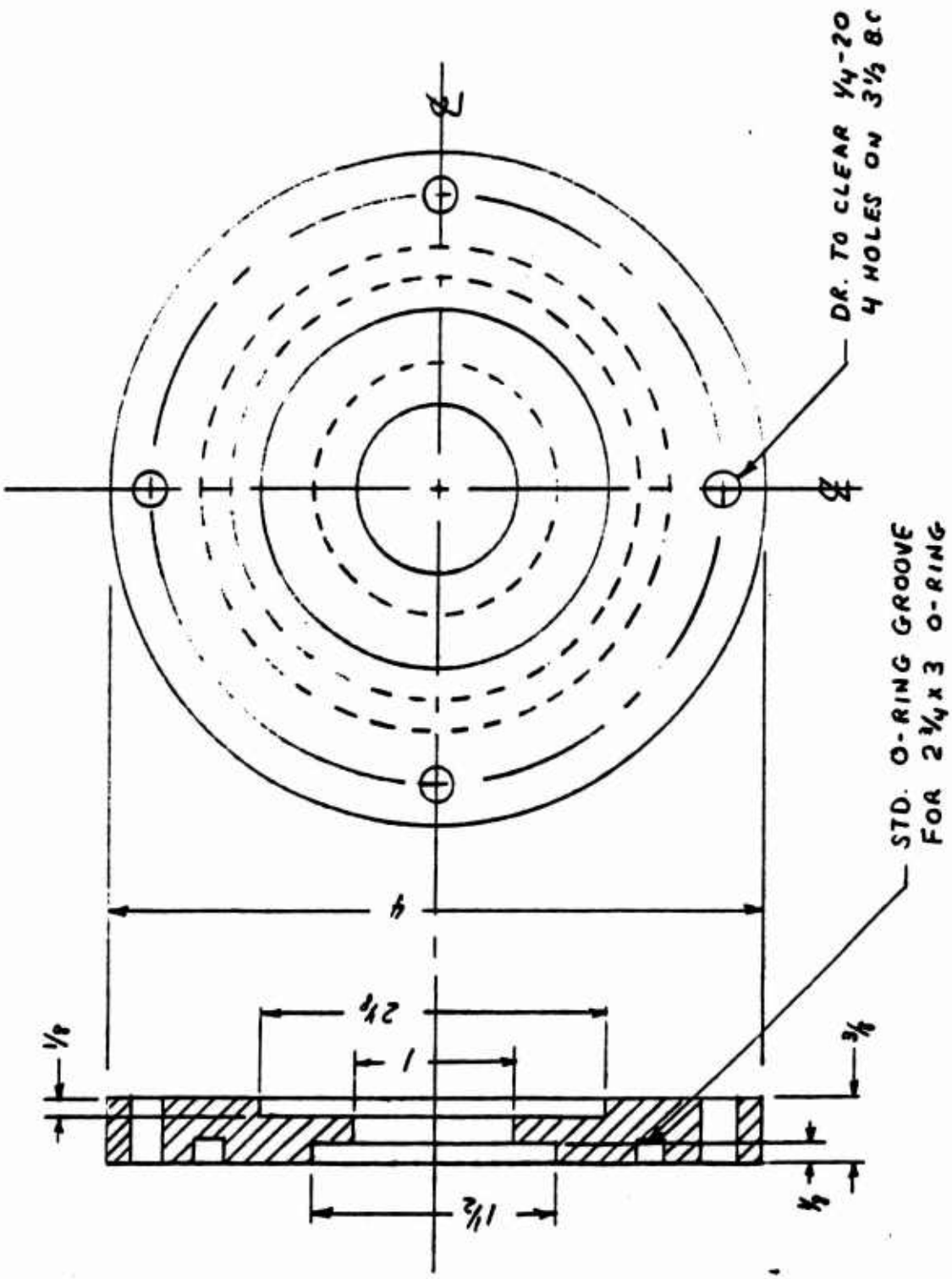

Figure 23. Entrance Flange
Scale: full size
Mat: brass

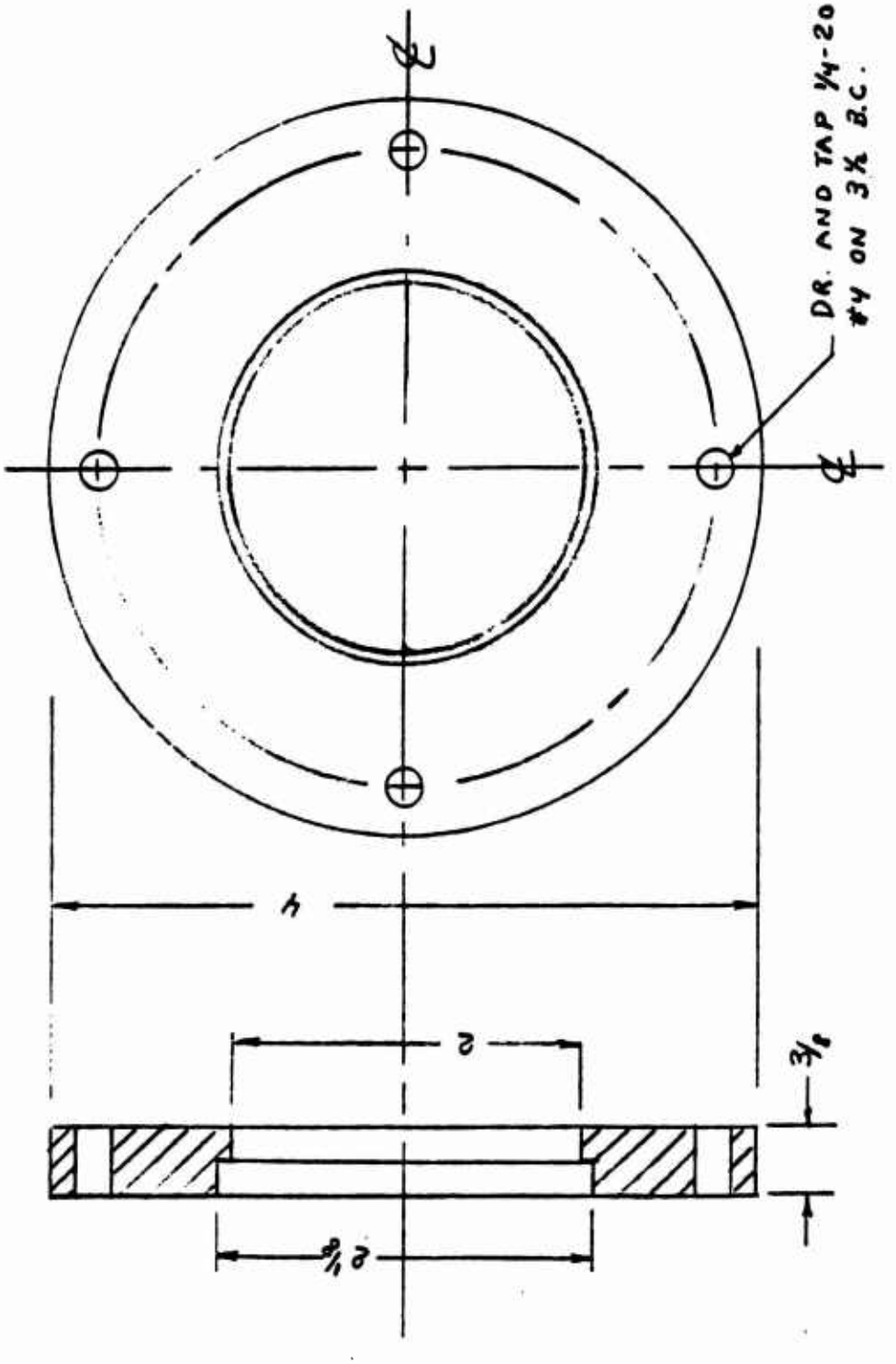

Figure 24. Cover Flange
Scale: full size
Mat: brass

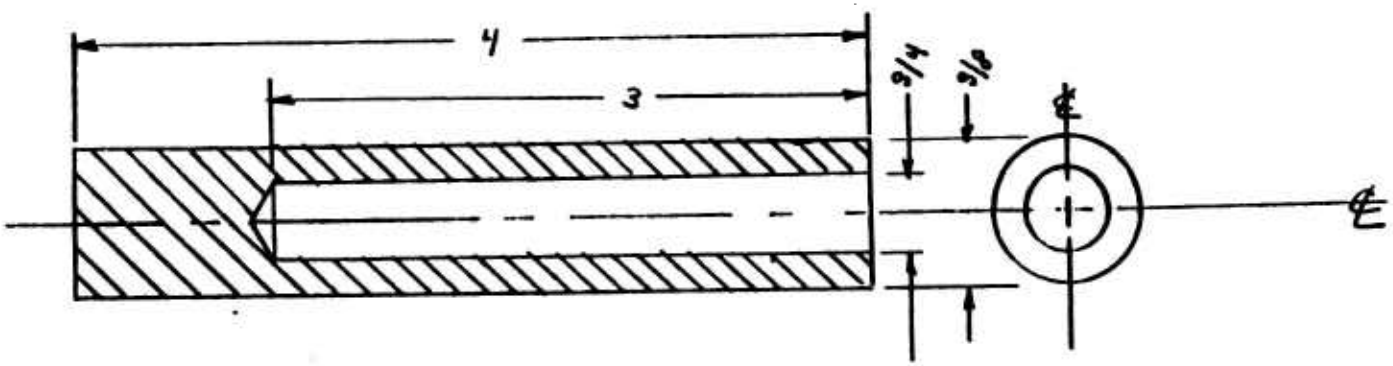

Figure 25. Casing for Magnetic Pickup
Scale: full size
Mat: Lucite

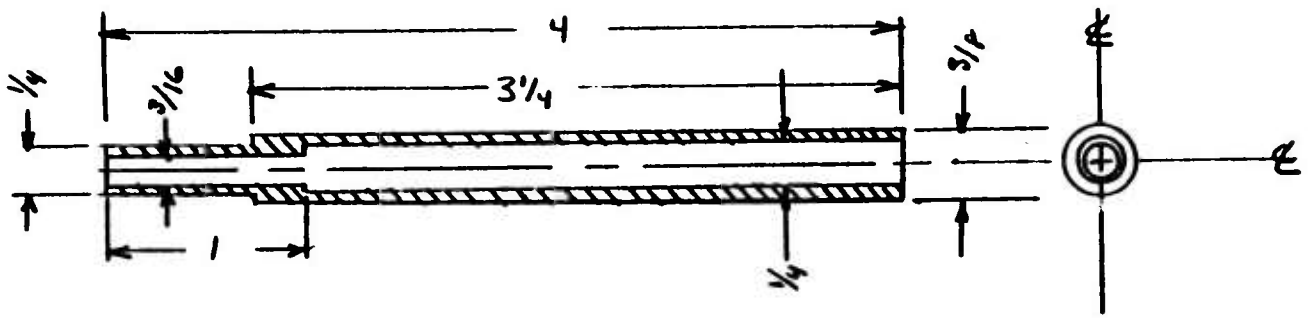

Figure 26. Magnetic Pickup Insert
Scale: full size
Mat: Lucite

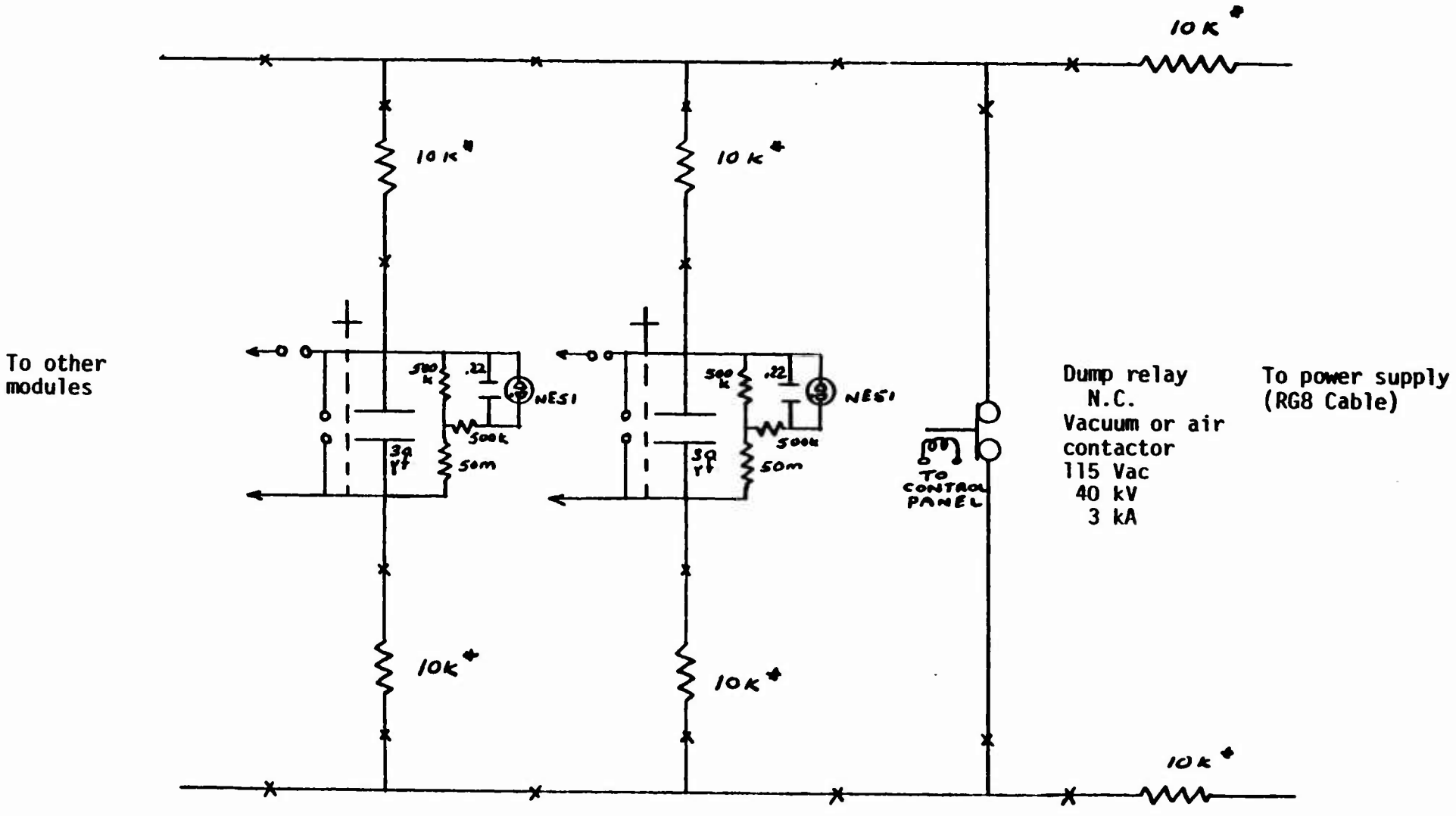

Figure 27. Module charging, discharging, monitoring, and safety system. x - denotes RG8 cable with shield removed. * - 10 1k wirebound 10W in series on circuit board.

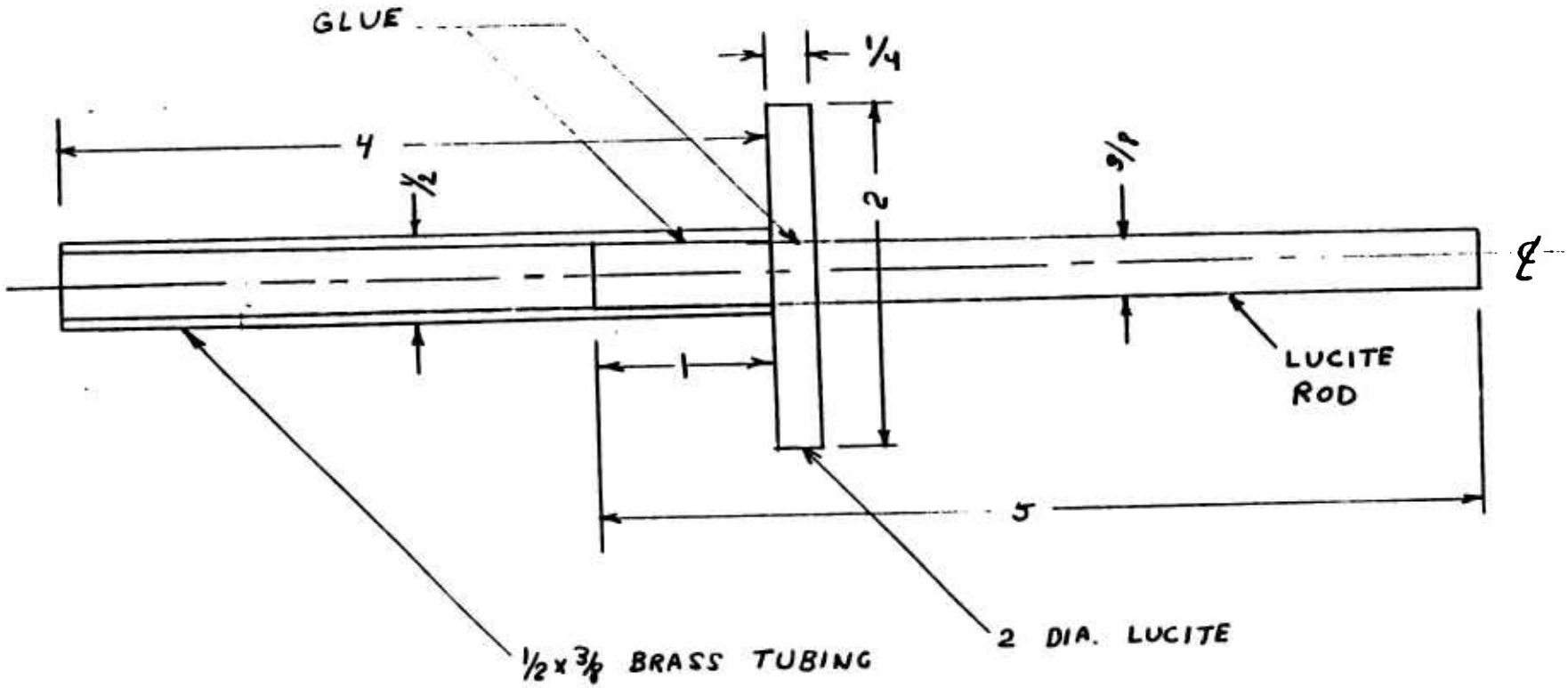

Figure 28. Shorting bar
Scale: full size
Mat: As shown

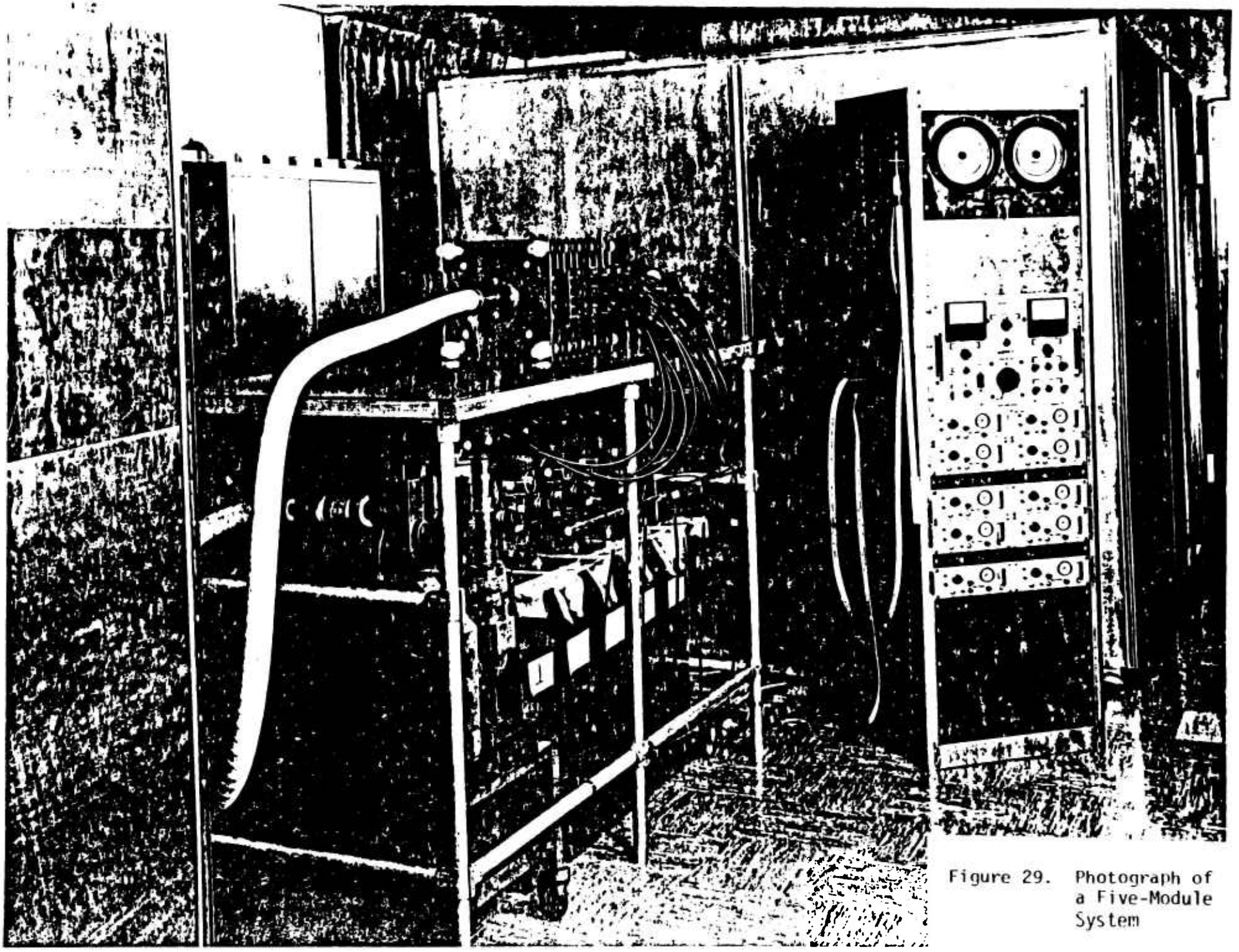

Figure 29. Photograph of a Five-Module System

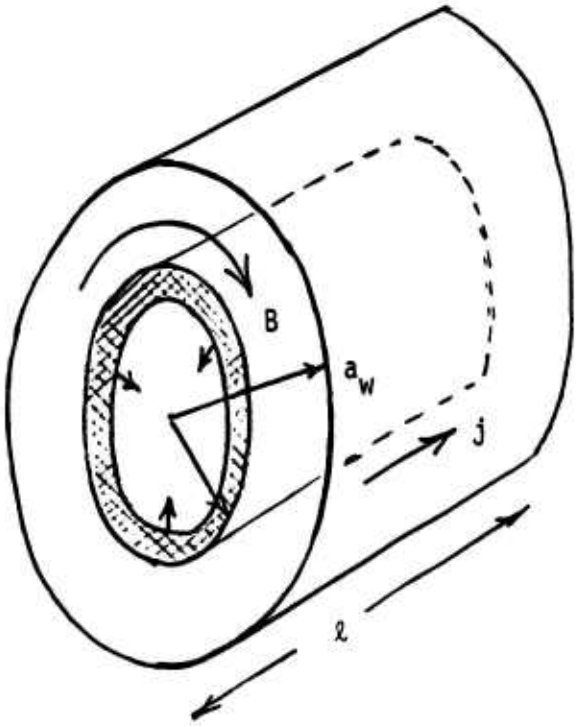

Figure 30. Geometry of Imploding Plasma Discharge

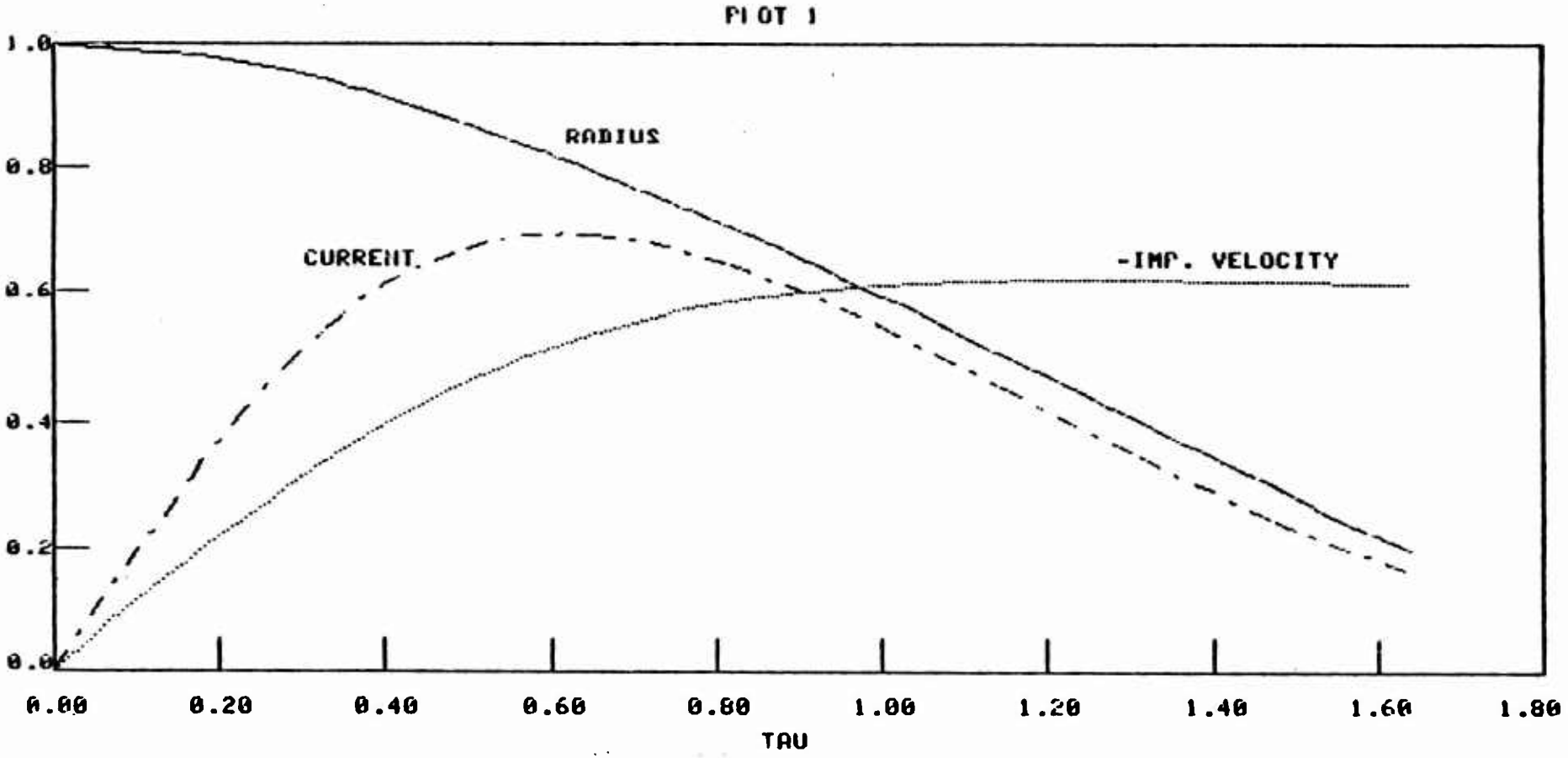

Figure 31. Plot of the dimensionless radius A, current i, and implosion velocity $\dot{A}$ as functions of $\tau = \omega\tau$. System parameters in dimensionless units are shown in Table 1. At $\tau = \tau_{imp} = 1.61$, the plasma radius equals the projectile radius ($a_p = 0.2$), and $\ddot{A}(\tau_{imp}) \approx 0$. Note that the current has not yet reached zero.

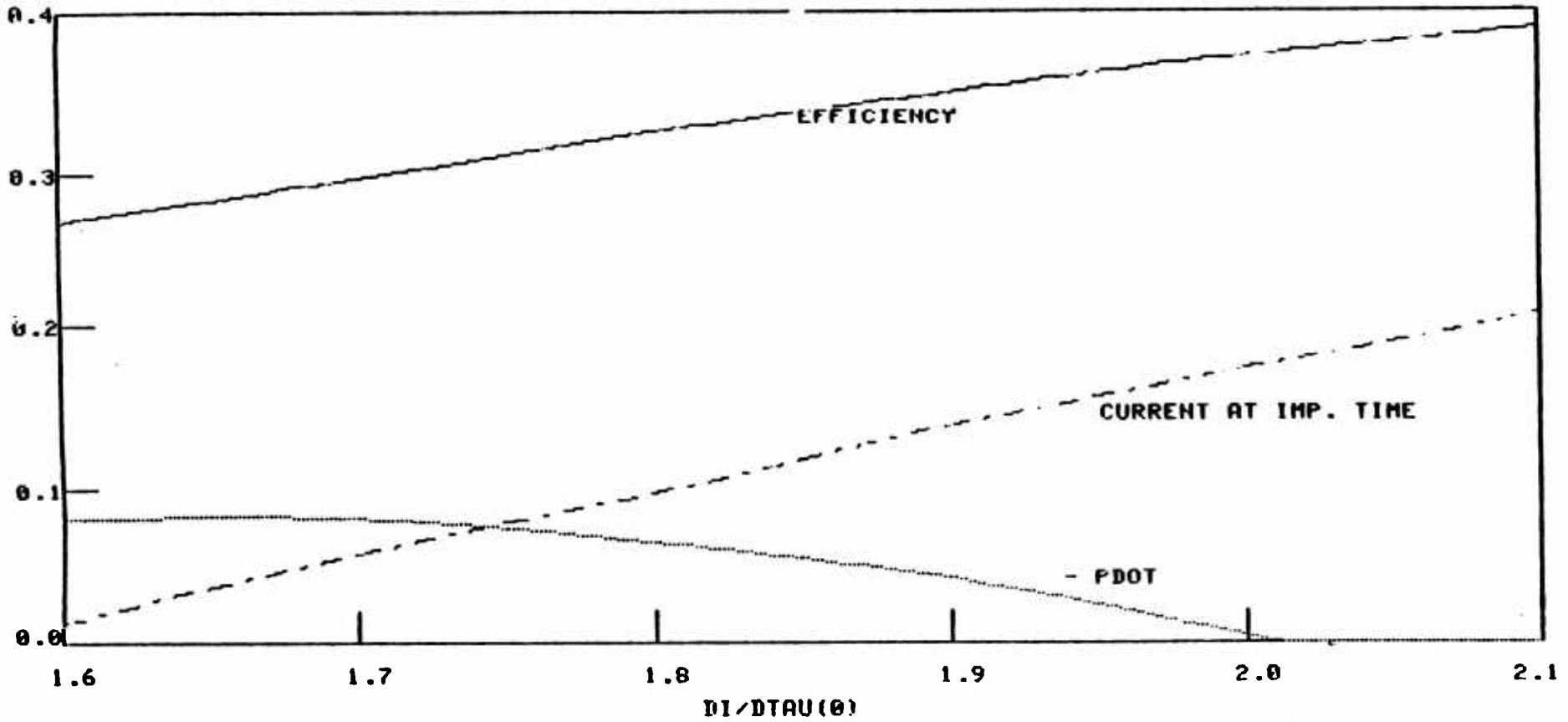

Figure 32. Plot of efficiency ε, current $i(\tau_{imp})$, and $-\ddot{A}(\tau_{imp})$ versus the initial current derivative $\frac{di}{d\tau}(0)$. Other parameters are as in Table 1. As $\frac{di}{d\tau}(0)$ increases, efficiency rises but the strength of the stabilizing potential well (which scales with $\ddot{A}(\tau_{imp})$) decreases.

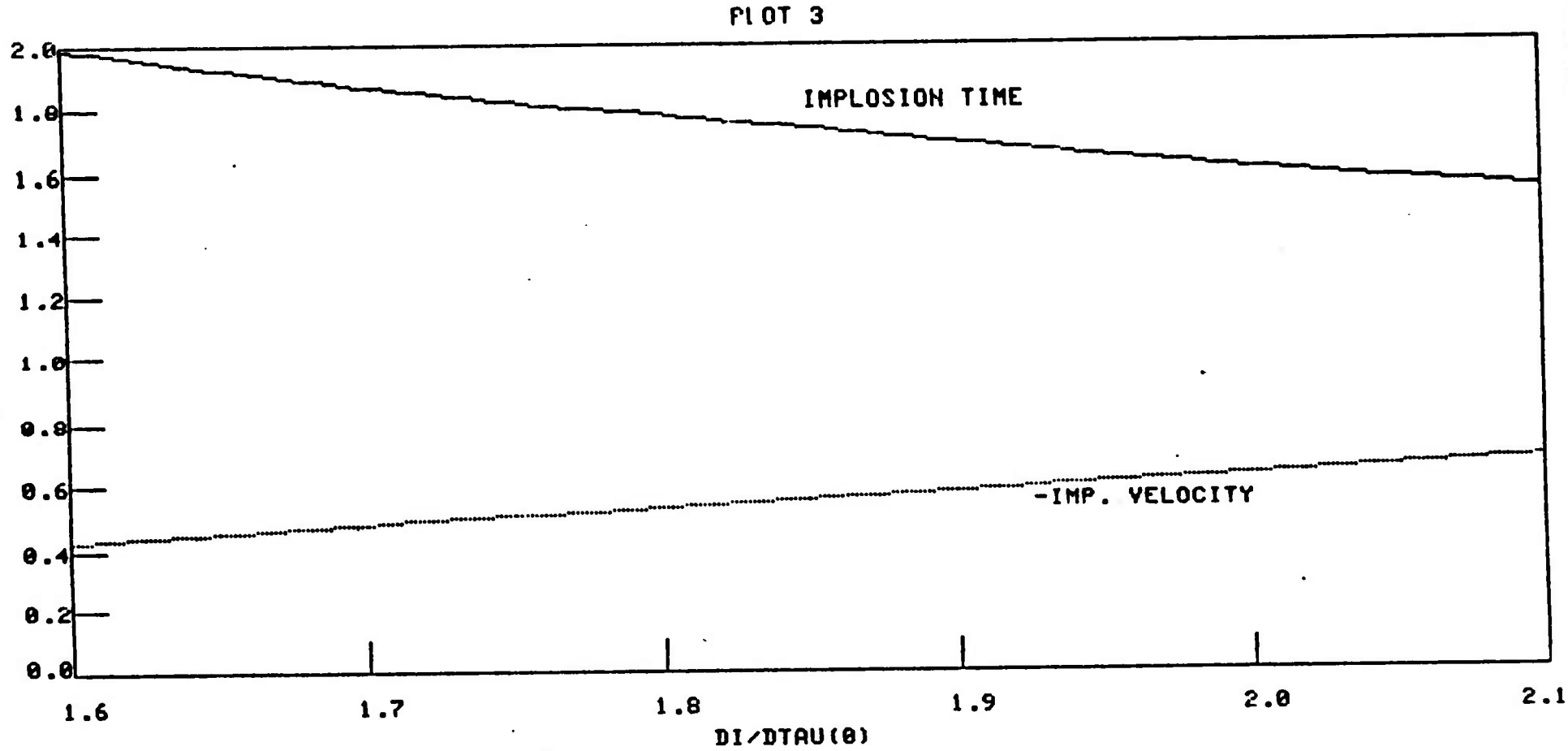

Figure 33. Variation in implosion time τ_{imp} and implosion velocity $\frac{d\Lambda}{d\tau}(\tau_{imp})$ with the initial derivative in the current.

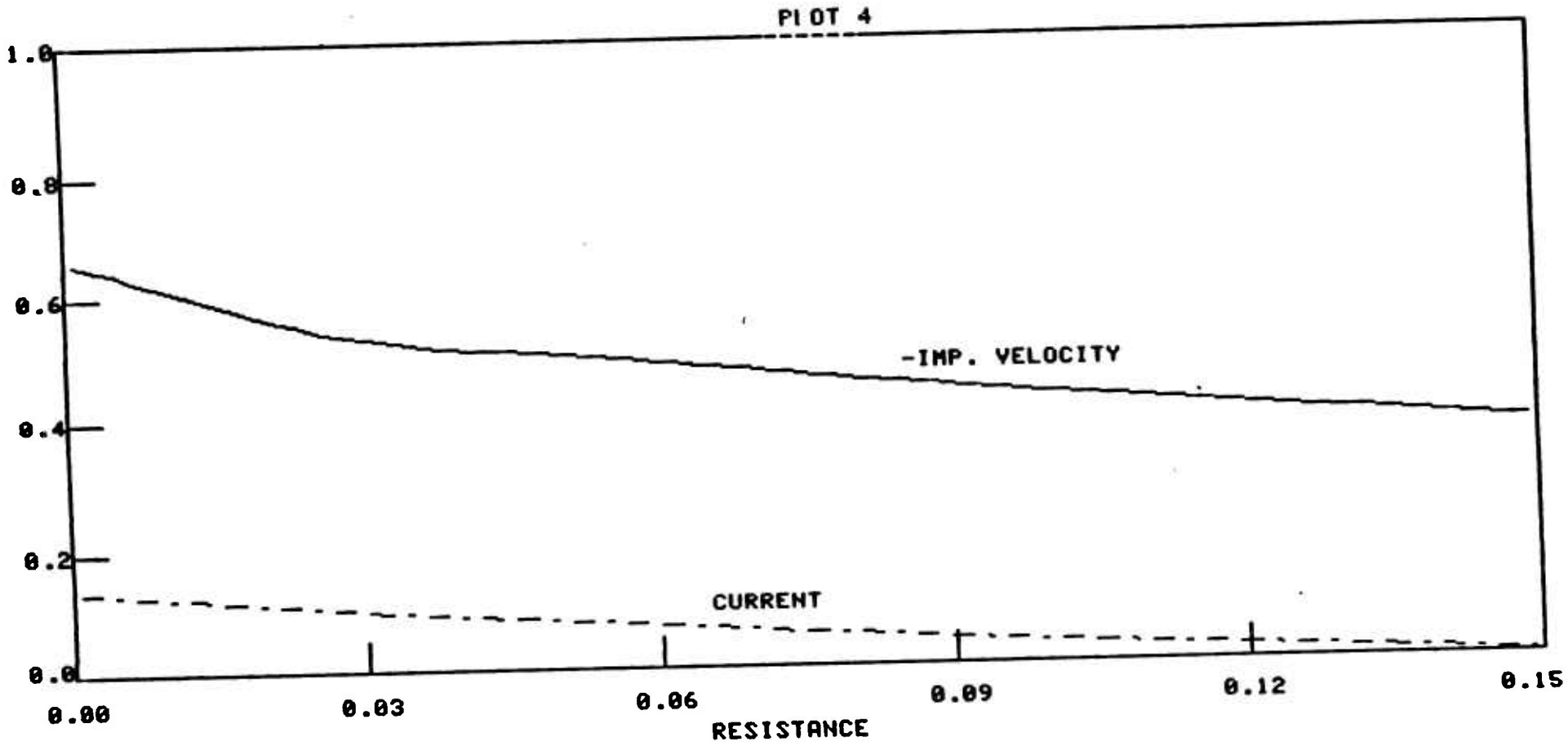

Figure 34. Variation of current $i(\tau_{imp})$ and implosion velocity $\frac{dA}{d\tau}(\tau_{imp})$ versus the dimensionless resistance r. Increasing r lowers current and implosion velocity (and hence efficiency), although some of the energy may be recovered in the form of I^2R heating.

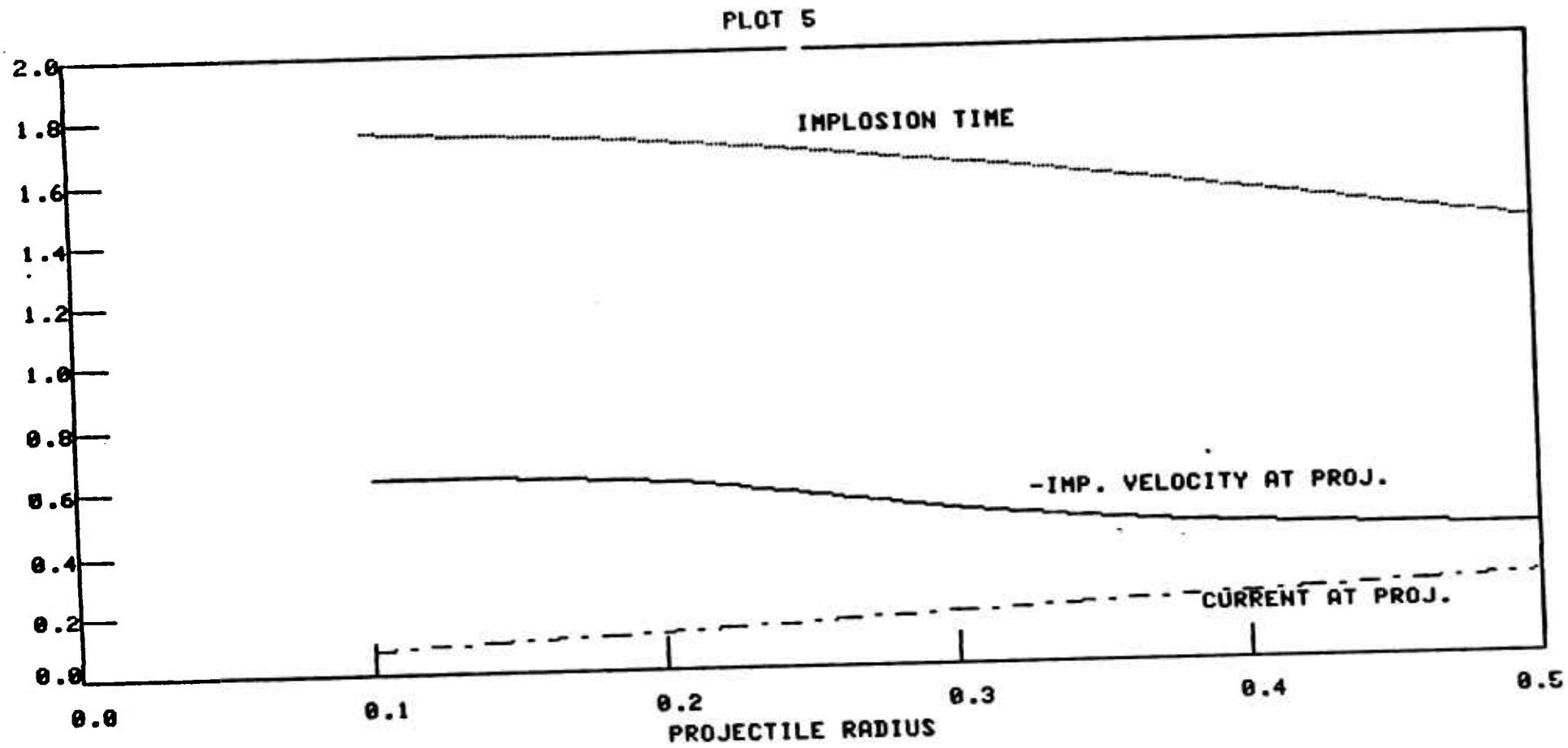

Figure 35. Plot of τ_{imp}, $-\frac{dA}{d\tau}(\tau_{imp})$, and $i(\tau_{imp})$ versus projectile radius A_p. Some of the apparent loss in implosion velocity (or efficiency) could be recovered by allowing the initial derivative of the current to decrease.

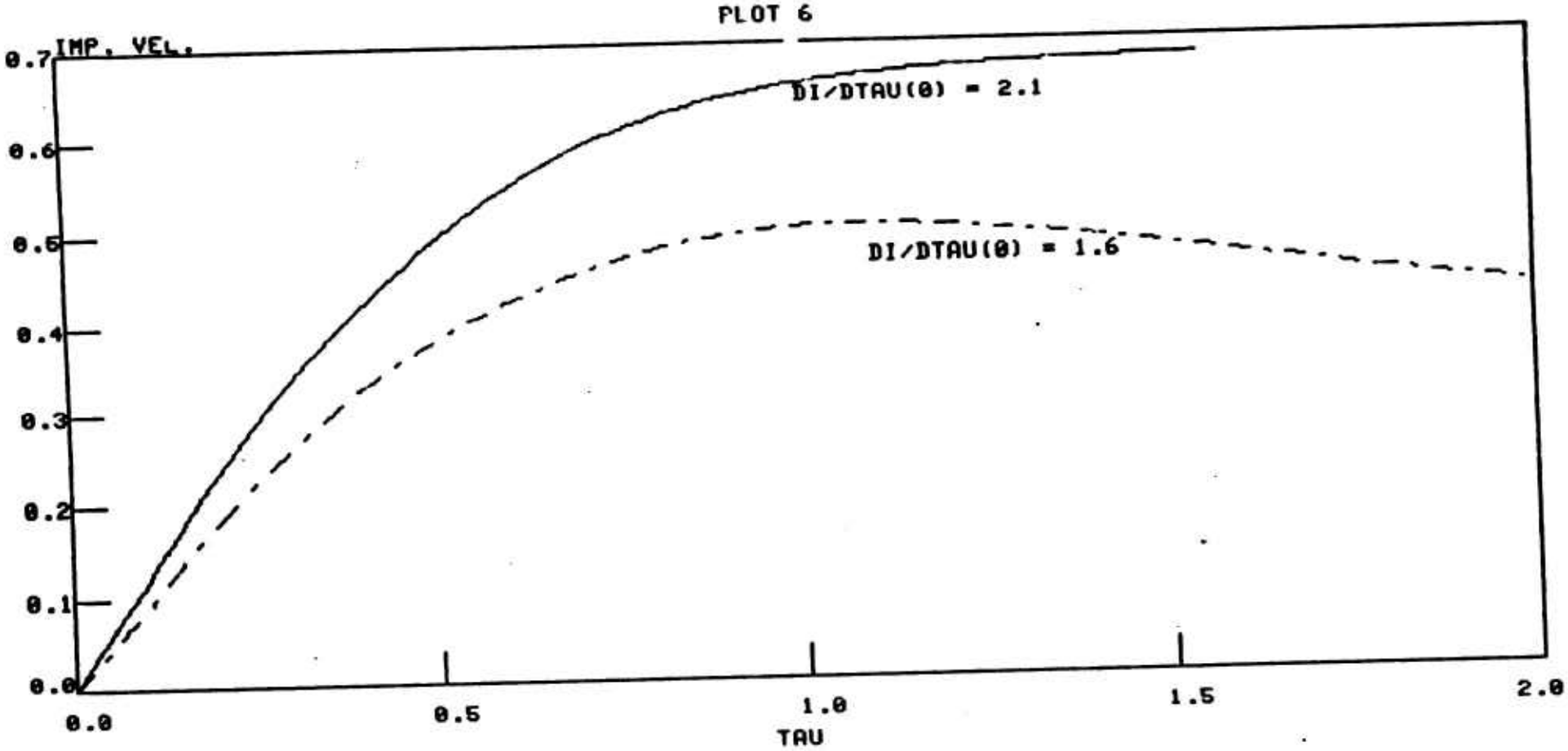

Figure 36. Plot of implosion velocity versus τ for two values of $\frac{di}{d\tau}(0)$. For $\frac{di}{d\tau}(0) = 2.1$, the implosion velocity is higher but there is no stabilizing force on the projectile. Lowering $\frac{di}{d\tau}(0)$ reduces the implosion velocity and efficiency somewhat, but provides a potential well for projectile stability.

APPENDIX

The MAID System -
Data Base and Design Issues

S. A. Goldstein, F. Sandel, D. A. Tidman, D. Massey
GT-Devices (JAYCOR)*

and

I. M. Vitkovitsky, V. E. Scherrer
Naval Research Laboratory†

GTD80-3

Presented at the
Conference on Electromagnetic Guns and Launchers

November 4-6, 1980

San Diego, California

*Work supported by ARRADCOM Contract DAAK10-80-C-0267.
†Work supported by ARRADCOM and the AFWL.

The MAID system stands for Mass Accelerator using Imploded Discharges [see J. Applied Physics 51, 1975 (1980)]. It is designed to accelerate masses of a few grams to velocities at ~ 10^7 cm/s and is based on the fact that plasmas can achieve velocities in that range using very simple pulse power technology. The plasma density, ρ, that impacts on the moving mass and accelerates it is chosen so that the resulting pressure during plasma-solid impact ($P \sim \rho v^2$) should not exceed the crushing strength of the solid. Presently such a system is being tested at JAYCOR and we review here the basic concept, the driving mechanisms, and the features of the system. Recent experiments performed at the Naval Research Laboratory which provide data supporting the feasibility of the MAID concept will also be discussed.

In Figure A a conceptual schematic of MAID shows a set of Z-pinches at different stages of radial implosions towards a common axis. The cone shaped projectile is injected from the left and is engulfed by the collapsing plasma only on its trailing side. The center of action of the pressure pulse on the projectile lies ahead of its center of mass so that stable acceleration in the axial direction is expected (but a variety of projectile geometries will be explored). The sensing units between the modules provide information on projectile location and velocity and via a fast logical system decides on triggering times of the modules ahead of projectile location. The typical axial electrode spacing per module is a couple of cm for projectile masses near one gram. Since crushing strengths are ~ 10^9 dynes/cm^2 the expected increase in projectile velocity will be in the range of 10^3 to 10^4 cm/s per module. About 5×10^3 modules are needed in order to achieve 10^7 cm/s.

The driving mechanisms on the projectile include three major contributors and each one of them can be varied in order to achieve optimum acceleration along the accelerator. These include: (i) collision of the imploding plasma with the projectile, (ii) sustained magnetic pressure due to the Z-pinch current holding on the plasma and (iii) projectile material ablation.

The first mechanism imparts momentum in the axial direction because the plasma is pushed back (lowest pressure holding against it is in the hole towards the previous module). Momentum conservation implies that the projectile velocity increase is approximately equal to the plasma velocity times the plasma-to-projectile mass ratio. Since the plasma is swept radially inwards,

decreasing its radius by an order of magnitude, the plasma mass can be about 10^{-3} g and at a velocity of 10^7 cm/s it will impart 10^4 cm-g/s to the projectile. Notice that the plasma density in front of the projectile is only 10^{-6} g/cm^3 so that the shock generated in front of the projectile does not give rise to a significant drag.

The sustained magnetic pressure (mechanism ii) may be important if high current persists through the Z-pinch which holds the plasma against radial expansion, thereby forcing it to expand axially backwards. The plasma mass may be increased by flow of additional gases from the conducting walls into the Z-pinch replacing the plasma that jets back. This mechanism is useful mostly at the low velocity end ($v < 10^6$ cm/s).

The ablation of material (iii) of the projectile is a result of both radiation and heat transfer from the plasma to the projectile. Part of the outer layer will undergo evaporation (protecting during that process the internal parts by turning into an opaque plasma) and ablate backwards adding to the momentum transfer by rocket action. Since this mass is already moving with the projectile and it is ablated back so that its velocity is reduced in the laboratory frame (ideally to zero!) it works as a very efficient rocket.

A few simple mathematical models treated show that a combination of the above mechanisms can result in efficiencies of $\sim$ 20% for the overall system. In particular, high efficiency is obtained at the high velocity end while dropping, roughly linearly, with velocity at low velocity ($\sim 10^5$ cm/s). The basic reason for this result is that MAID is a momentum driver, imparting a fixed momentum increase. The energy increase of the projectile is $mv\delta v$ and for fixed $m\delta v$ the energy efficiency goes up with v.

The major advantages of the MAID system relate to its use as a long lived device. The projectile has no contact with the walls but is confined radially by the dense plasma. The Z-pinch plates can thus be used for many shots where the lifetime is limited by low current plasma effects and not by the projectile wall interaction. It is thus of major importance to study long lifetime Z-pinch systems for currents of the order of 2 to 3 $\times 10^5$ A.

The projectile survives since no current is driven through it. The distributed power is a very natural consequence of the concept and while the system as a whole can deliver a few tens of megajoules it does so in a time of

order 10^{-3} s and the separate units overlap each other in time (recall the Z-pinches are in various stages of collapse) so that very simple and low power units ~ 10^8 W can be employed. Existing, cheap units having long life can be employed in such a system including a combination of capacitor banks and small homopolar generators.

The geometry of the elongated system allows ease of access, replacing parts, cooling of the system, redundancy in diagnostics and finally, simple, low tolerance requirements. The pressure of ~ 10 Torr allows both a simple vacuum system and no attention to plasma contamination issues, and the system thus recovers fast enough to allow a high rep-rate (1 to 10 Hz are very easy). The aiming of the projectile is achieved by both the centering action of the Z-pinches and by fine tuning plasma puffs that will be distributed with sensing systems over a few meters of post acceleration to aim $\delta\theta < 10^{-4}$. Lengths vary from a few tens of meters for 10^6 cm/s and hundreds of meters for 10^7 cm/s for the applications discussed in the next paper and are in accordance with needs for maintenance, etc.

Presently a five module system (shown in Figure B) has been built using large flat plates with glass insulators to provide Z-pinches from r ≈ 6 cm down to 1 cm. The pinches are driven by capacitor banks and gas switches (shown in Figure C). The system could accelerate projectiles to a few 10^4 cm/s. The physics of plasma-projectile interaction will be studied using this system. We now discuss the NRL experiments using a single Z-pinch that provides a data base for MAID.

Figure Captions

Figure A. Mass Accelerator using Imploded Discharges

Figure B. The five module Z-pinch units assembled.

Figure C. Overview of the lab and the capacitors.

Fig A

MAID

Mass Accelerator using Imploded Discharges

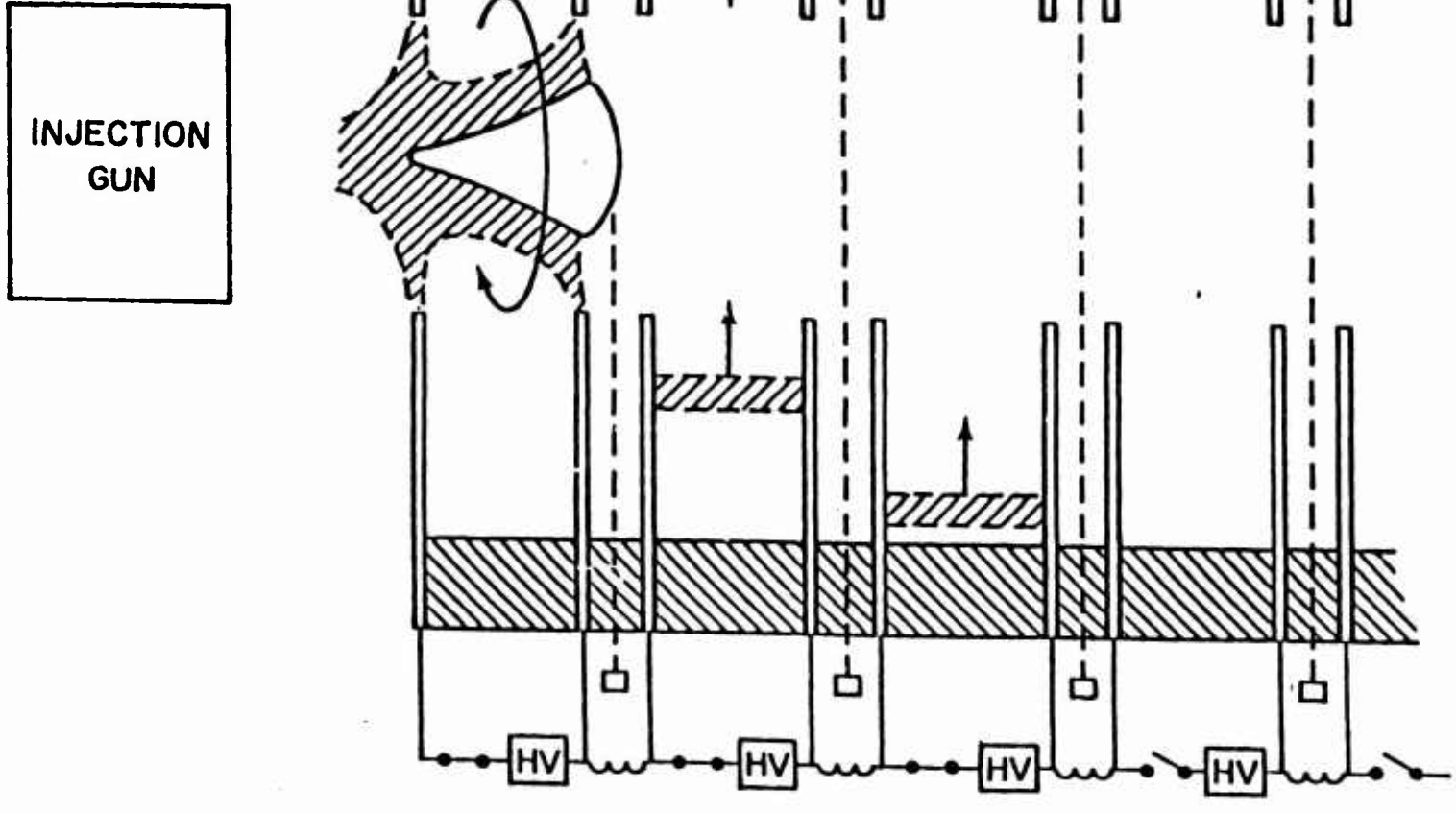

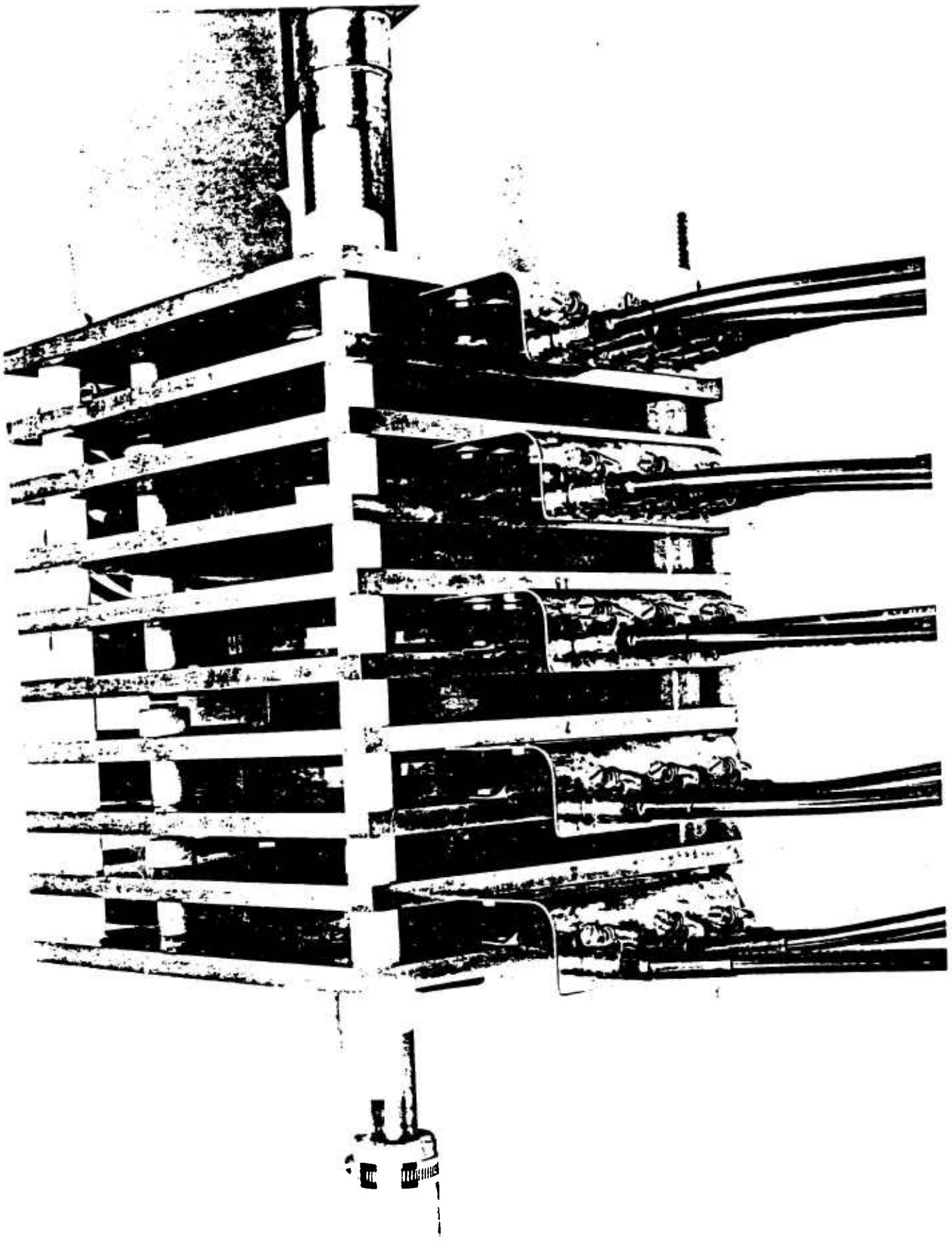

Fig 5.

Fig. 6.

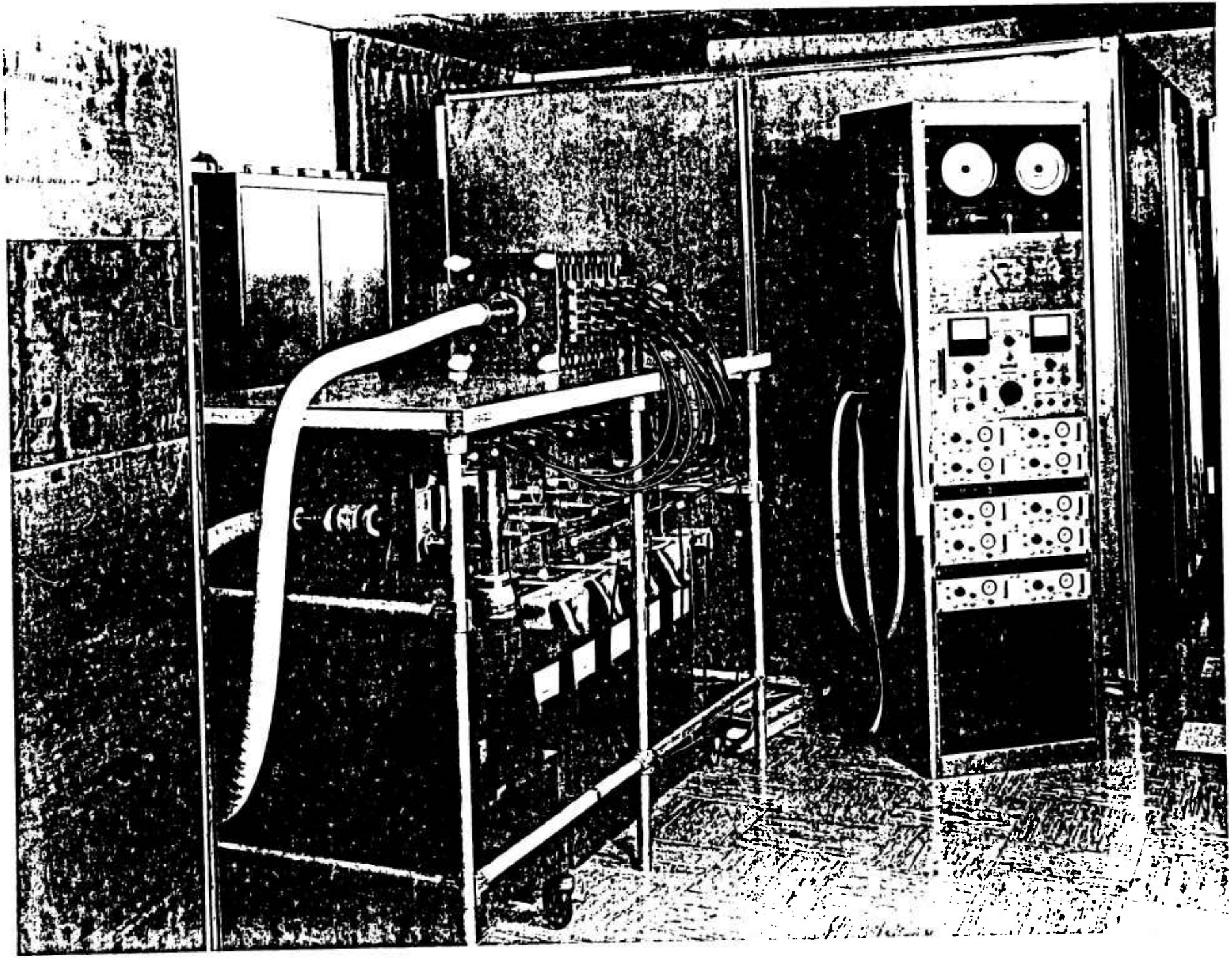

Plasma Implosions Driven by Fuse-Steepened Current Pulses

I. Introduction

In past years, when plasma facilities operated in the submegajoule range, capacitors were favored over inductive storage systems. Recently, with the need for large systems to generate multi-terawatt submicrosecond pulses, the inductive storage techniques[1-4] have been revived to improve performance at lower cost.

The objectives of this research were to model the AFWL Shiva-II inductive storage system with smaller current and power while duplicating rise-time characteristics. The model system was used to study the interaction between inductive storage and the load, such as the time-dependent partition of current between a pulse-steepening fuse and a realistic plasma load. Fast-rising (200 ns) current pulses generated by such techniques produce a more stable, faster moving plasma which, when thermalized, can be expected to yield a more intense, shorter duration, and higher temperature thermal pulse. The faster moving plasma sheath with closely coupled current would generate a larger rate of change of load inductance, L, so that the load current will not be short-circuited through the fuse. To optimize further the improved coupling of energy to the plasma, various methods of matching implosion time to current rise time by selection of fuse and implosion chamber parameters were also investigated.

II. The Facility

A circuit diagram and tabulation of circuit parameters is shown in Fig. 1. 50 kJ were initially stored in a capacitor bank, C, when V_o was 60 kV. The

system consisted of two current loops which shared a common element, the fuse. The fuse was vaporized by current i_1, when the low inductance rail-gap switches S1 were triggered. As the fuse vaporized in a time interval of 200-300 ns, the voltage V_{FUSE} increased by $L_1 \frac{di_1}{dt}$, and the solid dielectric switch S2 broke down by overvoltage, conducting the current i_2 through the load circuit. The imploding plasma load changed its resistance and inductance during the current pulse, leading to a complex interaction with the fuse.

To attain the inductance values tabulated in Fig. 1, to keep the current distribution uniform, and to duplicate other features of the Shiva-II facility, the laboratory layout shown pictorially in Fig. 2 was used. Four identical capacitor banks were coupled to parallel transmission plates by low inductance rail-gap switches. The collector plates, immersed in pure water, connected the capacitors to the fuse and to the implosion chamber at the center.

The arrangement of the i_2 circuit is illustrated in detail in Fig. 3. The fuse was a coaxially symmetric wire array, nominally 100 aluminum wires, each 0.0125 cm in diameter. Each wire was 10 cm long wound coaxially on a torroid having the cross-section shown. It was concentric with the implosion chamber in the center. The output switch S2 was a solid dielectric with multiple pinholes extending part way through; it broke down due to overvoltage at a preselected level.

The implosion chamber geometry and dimensions are presented in Fig. 4. The length was 4 cm and the nominal diameter was 5 cm. Sharp circular electrodes were located 3 mm from the walls to initiate the discharge without vaporizing wall material. The uniformity of initial breakdown appeared to be improved compared to initiation along the insulator surface. One end-electrode was rendered semi-transparent for optical viewing by use of a copper screen

electrode and lucite window. A high speed streak/framing camera was used to view the implosion in visible light. Small (1 mm diameter) $\frac{dB}{dt}$ loops were located at various radii within the implosion chamber to measure the distribution of current flowing there. The currents I_1 and I_2 (shown in Fig. 1) were measured as a function of time with $\frac{dB}{dt}$ loops and Rogowski coil (for i_2). Low inductance resistive dividers were used to measure voltages. The response of one of these dividers is illustrated in Fig. 5 where the output-pulse is superimposed on the signal into the divider. Pulse distortions are minimal even for pulses with 20 nsec risetime.

III. Fuse Design for Current Steepening

For some time, exploding wires and foils[1-5] have proven to be effective circuit breakers for generating electrical pulses with magnetic energy storage systems. More recently high power pulses with rise times in the tens of nanoseconds have been investigated[6,7] with success. The inductive storage technique has recently[7,8] been extended to operate with capacitor banks in the megajoule range. In the study of wire array fuses for inductive storage,[7] it has been found that the rise time and amplitude of the output voltage depends upon the number of parallel elements for a given fuse cross-section when wire array fuses are immersed in water. The time-to-explosion increases as the number of parallel wires is increased for constant cross-section. This result indicates that, the larger the number of wires the more energy is lost to the surrounding water, and the rise time of the output voltage is thereby increased. On the other hand, a minimum of 10 wires are needed in the fuse to retain symmetric current flow around the Z-pinch so that uniform breakdown and implosion are obtained. The skin depth is also a factor in determining the maximum wire radius. If the wire radius is larger than the skin-depth for the charging

frequency of the storage inductor, one would expect the time-to-burst to increase because of non-uniform radial distribution of wire heating.

We have adopted a procedure in which numerical methods of circuit analysis[10] were used to determine the circuit currents, voltages, and output power as a function of time for a given constant load inductance and resistance, fuse cross-sectional area, and fuse length. One computer run was required for each set of input parameters. From a number of such computer runs, optimum fuse parameters were determined. Experiments were then performed in which the diameter, number, and length, of fuse wires were varied. The experimental results were compared to computer calculations, and those of other experimenters[7,11] to confirm our choice of optimum fuse parameters.

The schematic diagram which illustrates the computer calculations is presented in Fig. 6. Input to the computer program include L_1, L_2, L_3, i_1 the peak current in L_1, the fuse length, and cross-sectional area, and V_s the voltage at which switch S2 closed. Each of the above parameters was varied separately. The computer output was i_1, i_2, V_{LOAD}, load power, and fuse resistance R_F, as a function of time for each set of circuit parameters, fuse cross-section and length. In this analysis the characteristic time t_o is defined as:

$$t_o = 6 \times 10^{16} \frac{S^2}{I_1^2} \quad \text{(sec)} \qquad \text{(Eq. 1)}$$

where S is the cross-sectional area of the fuse in m^2 and i_1 is the peak charging current in amperes; t_o is the "time-to-burst" of the fuse determined from data given in Ref. 9, for Al foils exploded in water with a time to explosion of 200 μsec. For the example of Fig. 7, the value of R_2 was chosen to correspond to the case having a negligible value of $\frac{dL}{dt}$, leaving only the resistivity of the imploding plasma. The other input parameters were:

100 fuse wires, each 12.7×10^{-3} cm in dia., 20 cm long Al wires. This results in $t_o = 2.4 \times 10^{-8}$ sec. When the following quantities are used,

$L_1 = 31$ nh $\quad L_2 = 25$ nh $\quad L_F = 10$ nh

$i_1 = 10^6$ amps $\quad V_s = 50$ kV $\quad R_2 = 0.01\,s$.

The calculated quantities i_1, i_2, V_L and fuse conductivity plotted in Fig. 7 as a function of time are obtained. The switch S2 was assumed to close early in the rise of V_F, at about 50 kV, allowing current i_2 to flow through the load. As the fuse conductivity approached zero causing the current i_1 to decrease, V_{FUSE} increased rapidly by an amount $V = V_1 L \frac{di_1}{dt}$ also causing i_2 to rise. When the fuse conductivity reached zero all of the circuit current was flowing through the load and $i_1 = i_2$.

Similar computer runs were made in which the number of 5 mil diameter fuse wires were varied from 40 to 500. Other input parameters were the same as the example plotted in Fig. 7. That is, the load resistance was small compared to the inductive reactance. Another set of computer calculations indicated similar results when the load resistance was increased to 0.5 Ohm when it was large compared to the inductive reactance. The curves of Fig. 8 indicate that power and voltage are optimized for 100 wires. This fuse wire array however transfers less than optimum energy. It has been shown[2] that optimum energy is transferred from the capacitor to the load when:

$$\frac{W_o^{3/2}}{V_0 L_1^{\frac{1}{2}} S} = k_1 a \qquad \text{(Eq. 1)}$$

where: V_o = Capacitor Voltage

W_o = Stored Energy

L_1 = Storage Inductance

S = Fuse Cross-Sectional Area (m^2)

$1 < k_1 < 3$

$a = 2.2 \times 10^{16}$ Joules/kG for Al.

When: $V_o = 40$ kV

$W_o = 24$ kJ

$L_1 = 26$ nh

$k_1 = 2$ (kV/micron)

From Eq. 2, $S = 2.4 \times 10^{-6}$ m^2.

This corresponds to 280, 5 mil diameter wires. Since the computer calculations were based on experimental data accumulated under different conditions (200 μsec charging time) than the present ones, experimental fuse data was needed to compare, first with an experiment in which multiple wire fuses were exploded[11] in air and then one in which similar arrays were exploded in water.[7] In a later section, our present experimental results are compared with computer runs where a "dummy load" of fixed inductance and zero resistance was used.

The effect of the surrounding medium on fuse vaporization has been investigated by Kosalyn, et al.,[11] for wires exploded in air. They found that the initial rate-of-rise of fuse resistance was described by the following formula:

$$\frac{dR}{dt} = \frac{16\ell v\rho}{\pi n d^3} \qquad \text{(Eq. 3)}$$

where ρ is the cold resistivity, ℓ is the wire length, n is the number of parallel fuse wires, d is the diameter of each wire, and v is the velocity of the vaporization wave.[12] The only quantity in Eq. 3 that should be affected by the environment surrounding the fuse is the vaporization velocity v. The only data[12] available for v were the wires exploded in air at atmospheric pressure. If we assume that the vaporization wave velocity is the same for wires exploded in air and water, we can compare experimental values with those calculated using Eq. 3. This has been done for arrays of copper and aluminum wires and the results are presented in Table I where the ratio

of our experimental data to that calculated using Eq. 2 is shown in the last column.

TABLE I: SUMMARY OF FUSE PERFORMANCE

Wire Material	Number of Wires	Diameter (MILS)	Length (CM)	Maximum Fuse Resistance	Experimental dR/dt	Calculated dR/dt	Experimental Calculated
CU	70	5	5	0.10	5.2×10^3	6.2×10^3	0.8
CU	70	5	5	0.60	1.0×10^4	6.2×10^3	1.7
CU	100	5	10	0.75	2.5×10^4	0.86×10^4	3.0
CU	400	1.8	10	0.11	4.0×10^4	4.5×10^4	0.9
AL	100	5	10	0.70	5.0×10^4	2.5×10^4	2.0

The table summarizes results for several shots using copper and aluminum fuses, with tabulations of the number of wires, diameter, length, and maximum fuse resistance. The experimental dR/dt was taken from the initial straight-line portion of the resistance-time curve (about 200 ns). When a comparison is made between the experimental dR/dt values and those obtained by substituting values into Eq. 2, they agree within a factor of 3, and we conclude that our data for fuse wires exploded in water do not differ significantly from those of a simple model that was developed for explosions in air. The "time-to-burst" is defined as the time interval between initial current flow in the exploding wire, and when current cut-off occurs due to wire vaporization. It was previously established[7] that:

$$t_o = 0.0094\ (N-1)^2 + .37 \qquad \text{(Eq. 4)}$$

where t_o is the time to burst and N = the number of 1 mil diameter copper wires immersed in water. Eq. 3 was confirmed for the range ($1 < N < 24$).

In Fig. 9 for our experimental data "time-to-burst" (t_o) is plotted versus the number of 5 mil diameter copper wires ($40 < N < 80$) immersed in water. Our data also support the variation described by Eq. 3.

The build-up of fuse resistance as a function of time is illustrated for three different wire fuse arrays in Fig. 10. The peak resistance recroded during any of the events was 0.7 Ohm for a 5 mil diameter aluminum wire.

IV. Transfer of Current to an Inductive Load

The calculations of fuse performance by computer analysis of circuit constants described previously and shown schematically in Fig. 6 can be checked experimentally by placing a short circuit in the implosion chamber in place of the plasma arc. Then the load inductance is 15 nH and the load resistance is approximately zero. A typical example of experimental results obtained with such an arrangement are shown in Fig. 11 where oscilloscope signals of fuse currents are shown in the upper picture and output current is reproduced in the bottom. I_1 was 1 MA; I_2 reached 600 kA in 200 ns. Experimental results obtained with aluminum fuse wires and a fixed inductive load are compared with theory in Fig. 12. The significance of this comparison is that for the same wire array parameters I_2/I_0 experimental exceeds I_2/I_0 theoretical nd has a slightly faster risetime. We conclude that the fuse works as predicted.

V. Transfer of Current to an Imploding Plasma Load

When the "dummy load" described above was replaced with a Z-pinch, the interaction between fuse and load plasma were much more complex, and experiments with plasma diagnostic measurements were required. Streak/framing photography and dB/dt probes were used.

An example of such an implosion driven by the capacitor bank without a fuse, is presented in Fig. 13. The chamber was filled with hydrogen having an ambient pressure of 0.38 Torr; current at minimum plasma radius was 500 kA. A streak picture displays radius versus time and two-dimensional pictures

were obtained at the times indicated. The leading edge of the plasma sheath imploded in a time t_{cl} = 700 ns. In the frames shown, part of the field-of-view was obscured by vacuum and dB/dt loop connections. The framing pictures show that the plasma formed and imploded uniformly.

Since some of the details of the implosion are lost in photo-reproduction a schematic representation of the streak picture has been sketched in Fig. 14. This illustrates that the plasma sheath was initiated uniformly at the sharp electrodes and retained this form as it accelerated inward. The leading edge of the plasma appeared to continually accelerate and collapse to the center line, where an expanding or reflected shock wave was immediately generated. The following plasma in the sheath appeared to slow down before interacting with the expanding shock, and the process of plasma thermalization was "stretched out" in time.

In contrast to the previous example, Figs. 15 and 16 illustrate a plasma driven by a fuse-steepened current pulse. The chamber of Fig. 4, filled with hydrogen having an ambient pressure of 0.38 Torr, was used. The nominal fuse contained 100-5 mil diameter, 10 cm long aluminum wires. As indicated in Fig. 15, the load current reached 500 kA in 200 ns. The streak picture in Fig. 16 shows that the leading edge imploded to the center line in 160 ns. In comparing the two examples with and without fuse, we note that the fuse driven plasma imploded more than twice as fast and the sheath thickness was less by more than a factor of two. The picture of Fig. 16 shows wall heating due to radiation, indicating possible electrical breakdown. Values of r and $\frac{dr}{dt}$ were derived from the leading edge of the plasma and are plotted as a function of time in Fig. 17. The curves show that most of the acceleration occurred in the final few millimeters of travel and that the leading edge

reached a $\frac{dr}{dt}$ of 5×10^5 m/sec as r approached zero. If we assume that $Z_p = dL/dt$, it is possible to calculate the effective radius of current flow versus time from measurements of dr/dt and V_L.

$$Z_p = \frac{V_L}{I_2} = dL/dt = -2 \times 10^{-7} \ell \frac{dr/dt}{r}$$

$$\frac{d}{dt}(\ell n r) = \frac{V_L/I^2}{2\times10^{-7}\ell}$$

$$r = r_o \ell \frac{V_L/I^2\, t}{2\times10^{-7}\ell} \qquad \text{(Eq. 5)}$$

In Fig. 18, we plot r(t) for the leading and trailing edges of the imploding plasma. Shown also in the graph is a plot of r(t) calculated by using Eq. 5 and the measured quantities V_L and I_2. A correction was made to V_L for the L_p di/dt voltage drop within the implosion chamber. This graph shows that the effective radius of the current lags behind the plasma for most of the implosion time but catches up during the last 1 cm of travel. Measurements obtained with dB/dt probes placed at two radial positions also indicate that current lags behind the current sheath. This subject will be discussed in detail later.

The performance of the inductive storage system depends upon the fuse resistance versus time characteristic and its ratio to the load impedance. The fuse resistance is plotted against time for the previous example in Fig. 19. Resistance increased from zero to 0.36 Ohms in 160 ns. This is approximately equal to the risetime of load current. For the application of model data to Shiva it is important to understand the roll of fuses in transferring current from the inductive store to the load. We expect this transfer to be optimized when Z_L/R_F is much less than 1. The previous example is completed by presenting this data.

The ratio of load and fuse impedances Z_L/R_f is plotted as a function of time for the above example in Fig. 20. The ratio is much less than 1 during the critical final compression time. This is a very important result, since the ratio must be small for efficient energy coupling to the load. We do not presently know the effects of the higher ratio at early times on the coupling.

In order to understand the mechanisms of energy absorption in imploding plasmas, we would like to know the distribution of mass and current as a function of time during the Z-pinch implosion. It is generally assumed that the snowplow model of the Z-pinch[13] applies and that the mass is swept up and contained within the plasma sheath. The current would also follow the ionized channel defined by the plasma sheath. However, measurements in conventional Z-pinches[14] indicate that at times current flows elsewhere in the implosion chamber. Since the current distribution determines dL/dt, including its final value, we decided to measure the current at two positions in the chamber and to correlate the current measurements to the plasma sheath position. Small loops 1 mm in diameter were mounted 1.2 and 3.2 cm from the center line of the chamber, midway between electrodes. The results are shown for a no-fuse experiment in Fig. 21. The plasma profile, extracted from the streak image, is plotted at the top, and currents are plotted on the same time scale at the bottom. The results show that for each dB/dt loop, current begins to flow immediately when the leading edge of the plasma passes, as expected. However, the current is small at this time and at t_c is only 50 kA, 14% of the load current. Only 10 kA flows inside dB/dt. A similar result is obtained when a fuse steepened current drives the Z-pinch as shown in Fig. 22.

These results confirm that current distribution of imploding plasma systems have a substantial thickness in comparison to initial plasma radius. Additionally, most of the current does not appear to flow in the imploding

plasma sheath as predicted by early theory.[13] There are several possible explanations. First, there may be a basic measurement problem with dB/dt loops in the plasma. They may substantially perturb the plasma flow. Second, radiation induced ionization at the walls may produce a conducting path that "short circuits" the plasma sheath and finally, an imcomplete ionization at early times may cause gas to be left behind, later becoming conducting.

It is not certain that radiation induced breakdown along the walls is detrimental. It has been shown[17] that wall breakdown causes circulating currents within the implosion chamber. That is, the wall breakdown acts like a crowbar, trapping energy inside the chamber. If this breakdown can be timed to occur at peak current, energy present in the implosion chamber may be dissipated in the imploding plasma. Our current traces shown in Figs. 21 and 22 also indicate circulating currents. The dB/dt 1 and dB/dt 2 currents exceed the circuit current when $t \cong 2.8$ μsec (Fig. 21).

Despite the apparent problem of current distribution, it is evident that current steepening fuses greatly increase power flow in imploding systems. This is illustrated in Fig. 23 which compares streak images for implosions with and without fuse steepening. The ambient pressure of hydrogen was the same in both cases and load current at t_{c1} was 500 kA in both cases. The fuse steepening decreased the implosion time from 340 ns to 160 ns while the sheath thickness was decreased by more than a factor of 2. These results are shown more quantitatively in Fig. 24 where radius of the leading edge is plotted against time for the two cases.

In general, the implosion time follows the classic relation for Z-pinch implosion time:

$$t_c = K(m/\ell)^{\frac{1}{4}}(di/dt)^{-\frac{1}{2}}10^{-8} \text{ sec.} \qquad \text{(Eq. 6)}$$

where K is a constant and ℓ is the length of the implosion, M is mass/unit length and di/dt is the current rise at $t = 0$. This linear dependence has been published[15] for $t \geq 3$ μsec and is reproduced as a solid line in Fig. 25.

Shown also in the figure are points obtained at NRL with and without fuses. The dotted line extension of data from Ref. 15 passes through the NRL points. Although Eq. 5 was fitted to gas Z-pinches it is interesting that Shiva imploding foil data[16] have t_c values less than those predicted by Eq. 5.

In general, the technique using fast-opening fuses to increase the power flow a storage system to the imploding plasma has been proven to be successful. The wire array fuse immersed in water performed as predicted when precision drawn wires were used. The measured load current and rise-time agreed with values calculated by circuit analysis. The time-to-burst agreed with previously published[7] semi-empirical formulas for wires exploded in water. The initial rise fo fuse resistance dR/dt, agreed with calculated values using a published formula[11] for wires exploded in air. The implosion time for gas Z-pinches powered by inductive energy storage is proportional to $(dI/dt)^{-\frac{1}{2}}_{t=0}$ in agreement with published results.[15] The plasma sheath thickness decreased and and was reduced by use of the wire fuses, indicating the possibility of increased radiation output during final plasma thermalization. Major difficulty in optimizing the heating of the plasma was indicated by dB/dt loop measurement at various radii in the implosion. They showed only a small fraction of the load current to flow through the plasma sheath, as has also been observed by others.[14] To understand this problem fully would require additional research studying the methods to restrict the current flow to a thin plasma sheath for better assembly as well as methods to further increase the speed of implosions to obtain higher thermal output pulses.

Our measurements show that during the later stages of the implosion most of the output current flows through the load and not the fuse.

References

1. H. C. Earily and F. J. Martin, RSI 36, 7, 1000 (1965).
2. C. H. Maisonnier, J. G. Linhart, C. Gourlan, RSI 37, 10, 1380 (1966).
3. L. Liebing, Z. Eng. Physics 26, 345 (1969).
4. S. A. Nasar et al., Proc. of the Sixth Symposium of Engineering Problems of Fusion Research, IEEE Pub. No. 75CH1079-5-NPS (Includes extensive bibliography).
5. Ch. Marjannia, J. G. Linhart, C. Gourlas, RSI 37, 1380 (1966).
6. Yu. A. Kotov, N. G. Kolganov, V. S. Sedor, B. M. Kovaltchuc, and G. A. Mesyats, Proc. International Pulsed Power Conference, Lubbock TX, 1976, PIAI.
7. D. Conte, R. D. Ford. W. H. Lupton, and I. M. Vitkovitsky, Prod. of the Seventh Symposium on Engineering Problems of Fusion Research, Knoxville, TE, 1977, Vol. II, p. 1066.
8. D. L. Smith, R. P. Henderson, R. E. Reinovsky, 2nd IEEE International Pulsed Power Conference, Lubbock, TX, 1979, p. 287.
9. D. Conte, R. D. Ford, W. H. Lupton, I. M. Vitkovitsky, 2nd IEEE International Pulsed Power Conference, Lubbock, TX, 1979, p. 276.
10. W. Lupton, NRL-unpublished work.
11. Article in Russian, B. M. Kosalyn et al. (1972).
12. F. D. Bennettand G. D. Kohl, in Exploding Wires, Vol. 4, p. 1, ed. by W. G. Chace and H. K. Moore, Plenum Press, NY (1968)
13. M. Rosenbluth et al., USAEC Report LA-1850 (1954).
14. I. F. Kvartshava et al., Nuclear Fusion 11, 385 (1971) (Additional references given)
15. L. A. Artsimovich, "Controlled Thermonuclear Reactions", p. 115, Gordon Research Science Publishers, NY, NY, 1964.

16. William L. Baker, Miles, C. Clark,James H. Degnan, Gerald F. Kiuttu, Charles R. McClenahan, and Robert E. Reinovski, JAP 49 4694 (Sep 1978).

17. T. Oppenlander, IAEA VII Conf. Int. Physique Plasmas et al Recherche Concurnant la Fusion Nulearre Controlee, Innsbruck, 1978.

Figures Captions

Fig. 1. Schematic diagram of Shiva model.

Fig. 2. Picture of the Shiva model facility.

Fig. 3. Implosion chamber and current-steepening fuse.

Fig. 4. Schematic of implosion chamber.

Fig. 5. Response of resistive divider to a fast input pulse.

Fig. 6. Calculations of circuit performance.

Fig. 7. Results of a typical computer run.

Fig. 8. Variation in number of 5 mil Al fuse wires.

Fig. 9. Time to burst (t_o) vs. number of wires.

Fig. 10. Fuse resistance vs. time for copper and aluminum wire arrays.

Fig. 11. Transfer of current to an inductive load.

Fig. 12. Comparison of experiment and theory for transfer of current to an inductive load.

Fig. 13. Streak/framing picture of plasma implosion.

Fig. 14. Schematic diagram illustrating features of streak picture of imploding plasma Z-pinch (no fuse).

Fig. 15. Electrical measurements of Z-pinch (no fuse).

Fig. 16. Streak picture of plasma implosion (with fuse).

Fig. 17. Plasma position and velocity during implosion.

Fig. 18. Implosion driven by fuse steepened current.

Fig. 19. Fuse resistance vs. time.

Fig. 20. Ratio of fuse to load impedance vs. time.

Fig. 21. Comparison of current profile to plasma sheath (no fuse).

Fig. 22. Electrical measurements for plasma implosion driven by fuse steepened current.

Fig. 23. Dependence of implosion velocity and sheath thickness on current risetime.

Fig. 24. Comparison of implosion with and without fuse (leading edge of plasma)

Fig. 25. Dependence of implosion time on di/dt and m/ℓ.

Fig. 1 SCHEMATIC DIAGRAM OF SHIVA MODEL

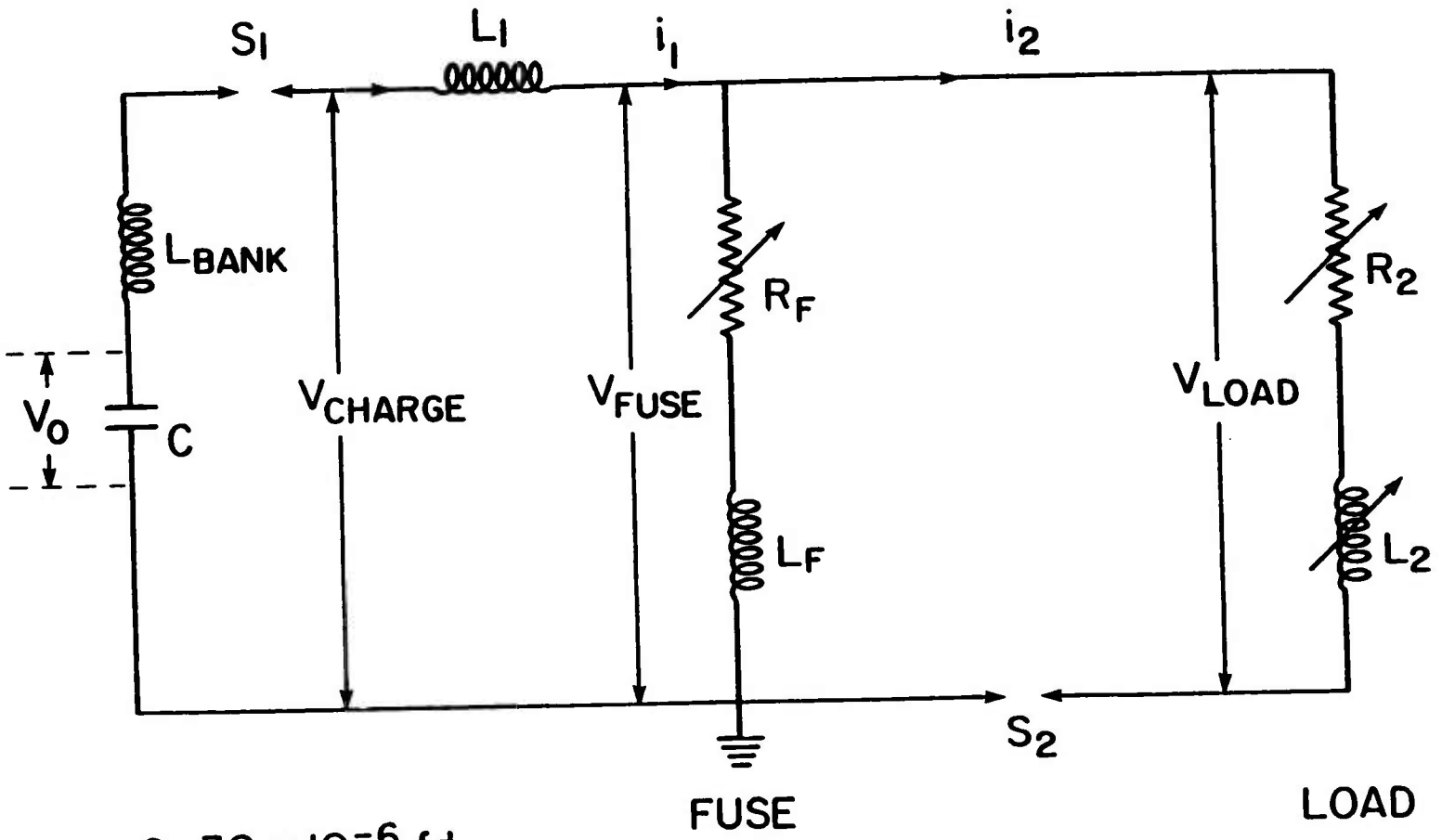

$C = 30 \times 10^{-6}$ fd

$L_{BANK} = 5$ nh

$L_1 = 16$ nh

$L_F = 10$ nh

$L_2 = 15$ nh

FIGURE 2

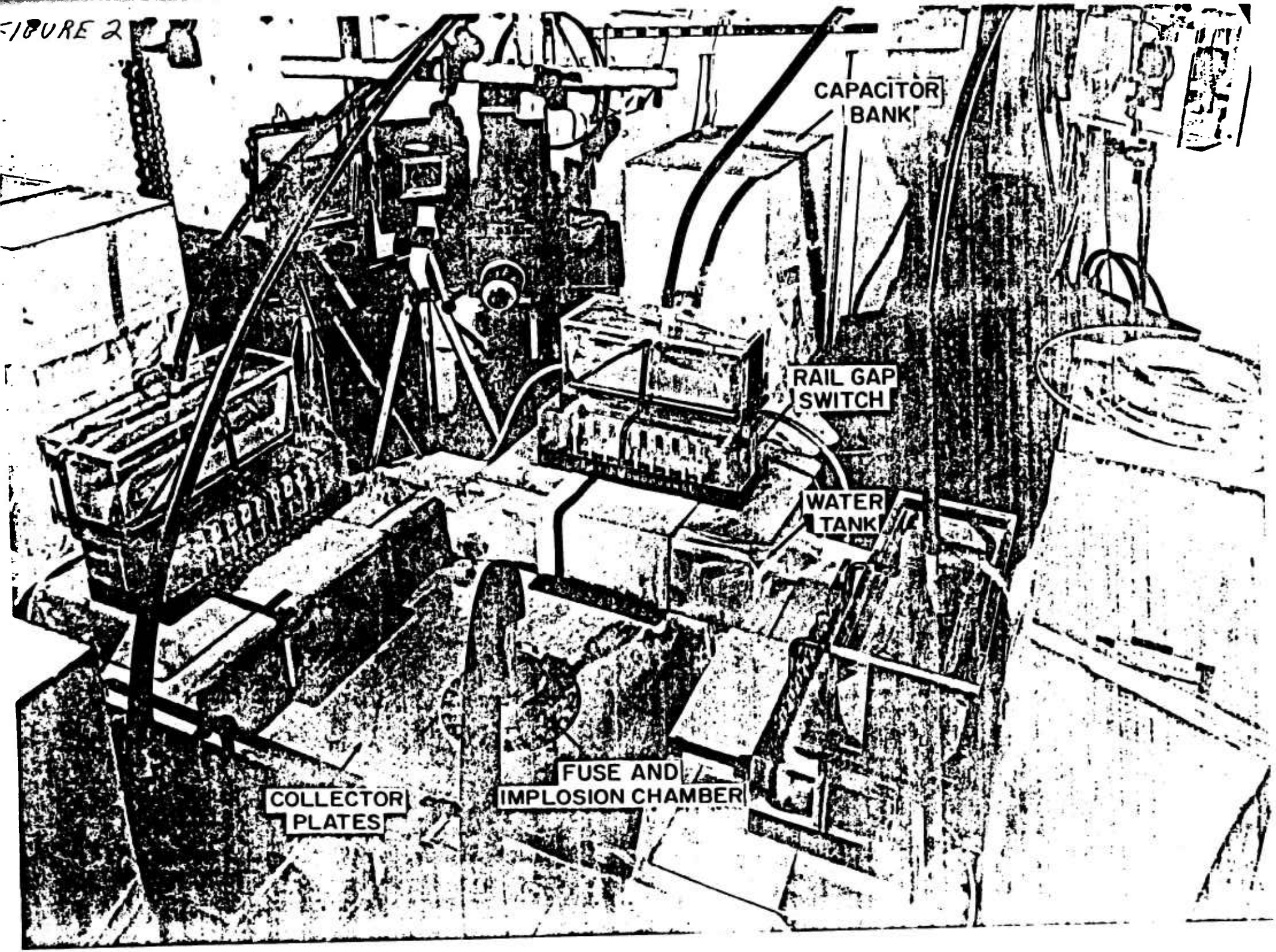
CAPACITOR BANK
RAIL GAP SWITCH
WATER TANK
FUSE AND IMPLOSION CHAMBER
COLLECTOR PLATES

FIGURE 3 IMPLOSION CHAMBER AND CURRENT-STEEPENING FUSE

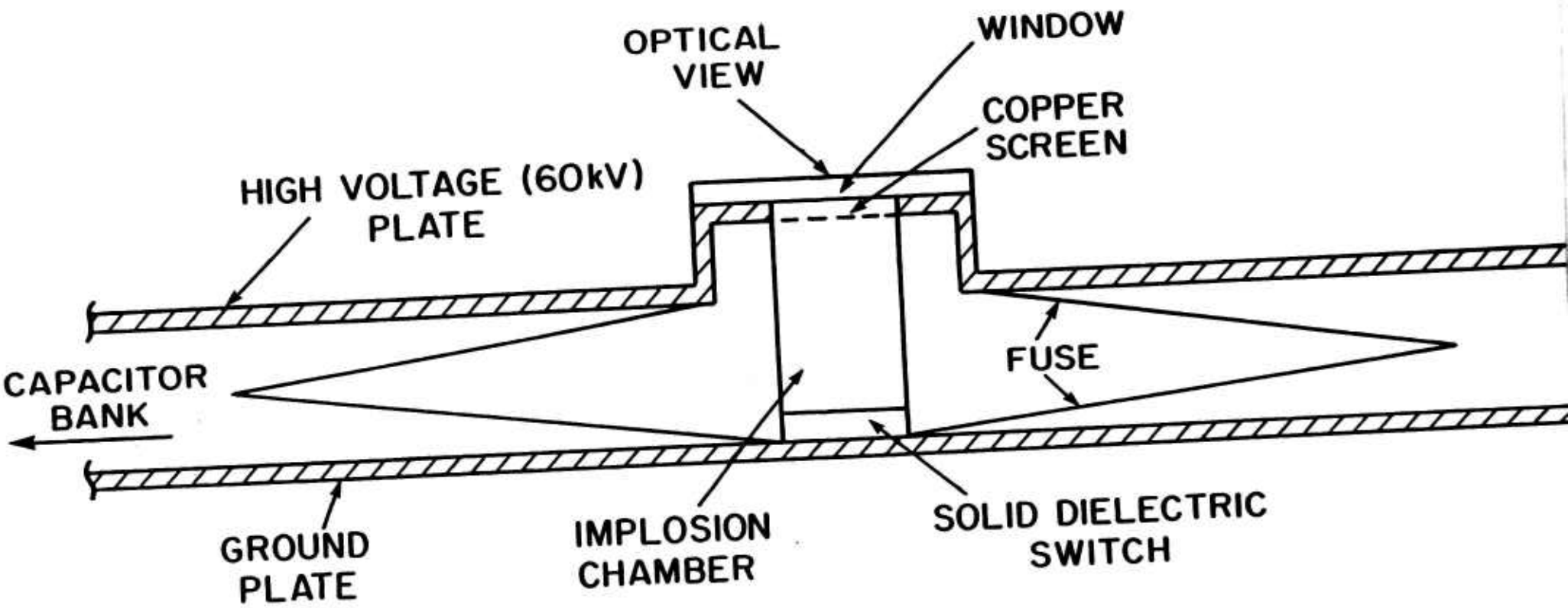

FIGURE 4 SCHEMATIC OF IMPLOSION CHAMBER

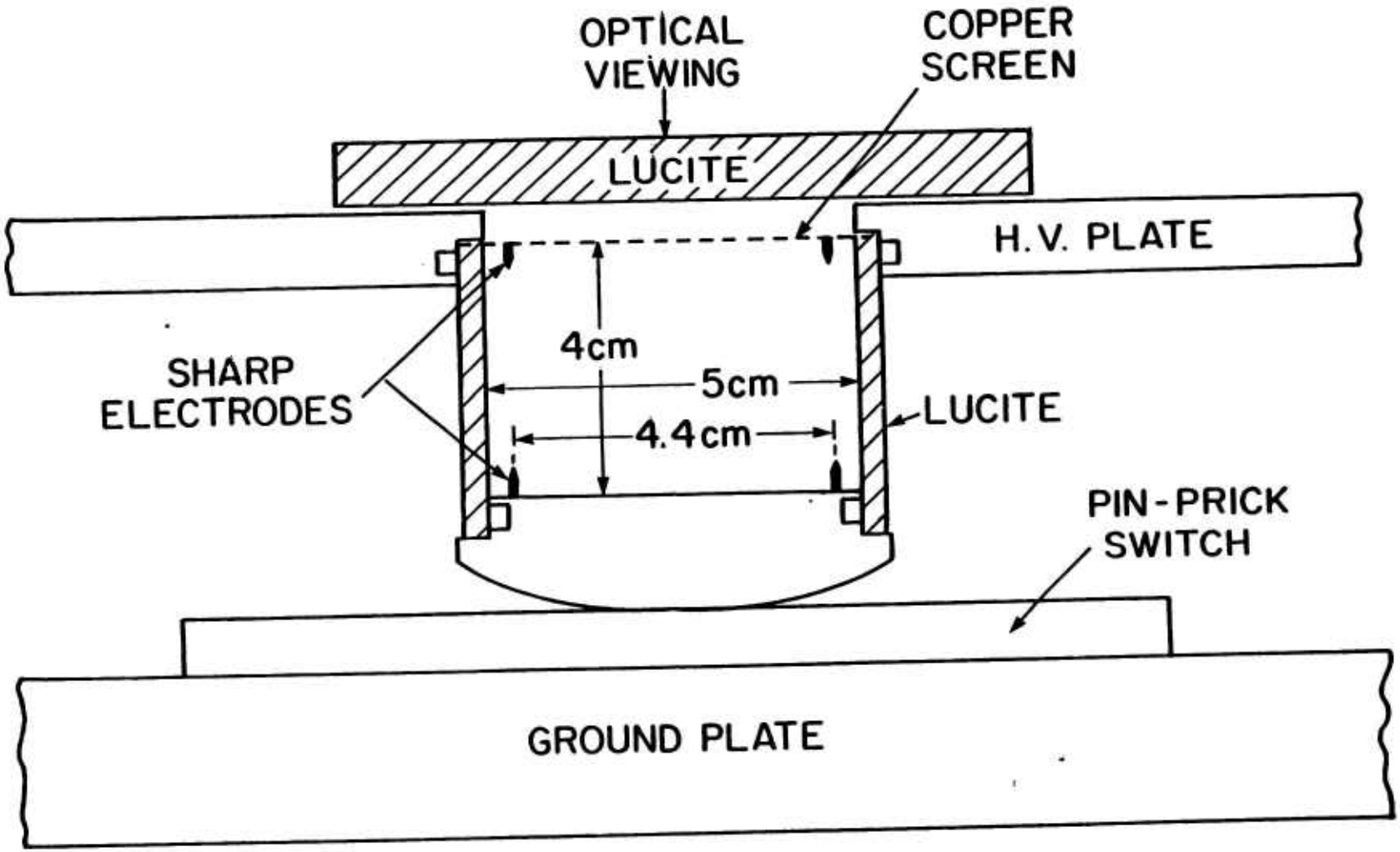

Fig 5 RESPONSE OF RESISTIVE DIVIDER TO A FAST INPUT PULSE DIVIDER IV (UNSHIELDED)

DIVIDER OUTPUT PULSE IS SUPERIMPOSED ON INPUT PULSE

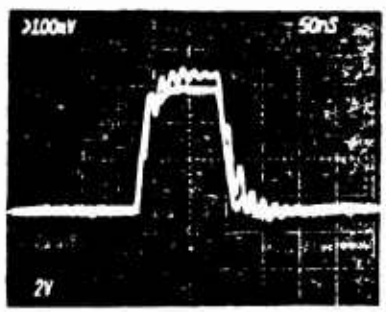

50 ns/DIV
INPUT 2V/DIV
OUTPUT 100 mV/DIV

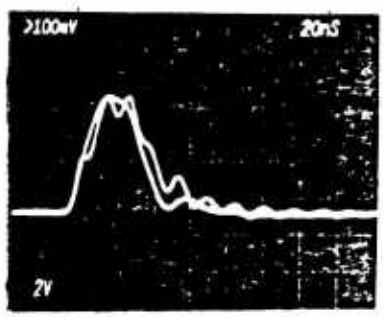

20 ns/DIV
INPUT 2V/DIV
OUTPUT 100 mV/DIV

FIGURE 6

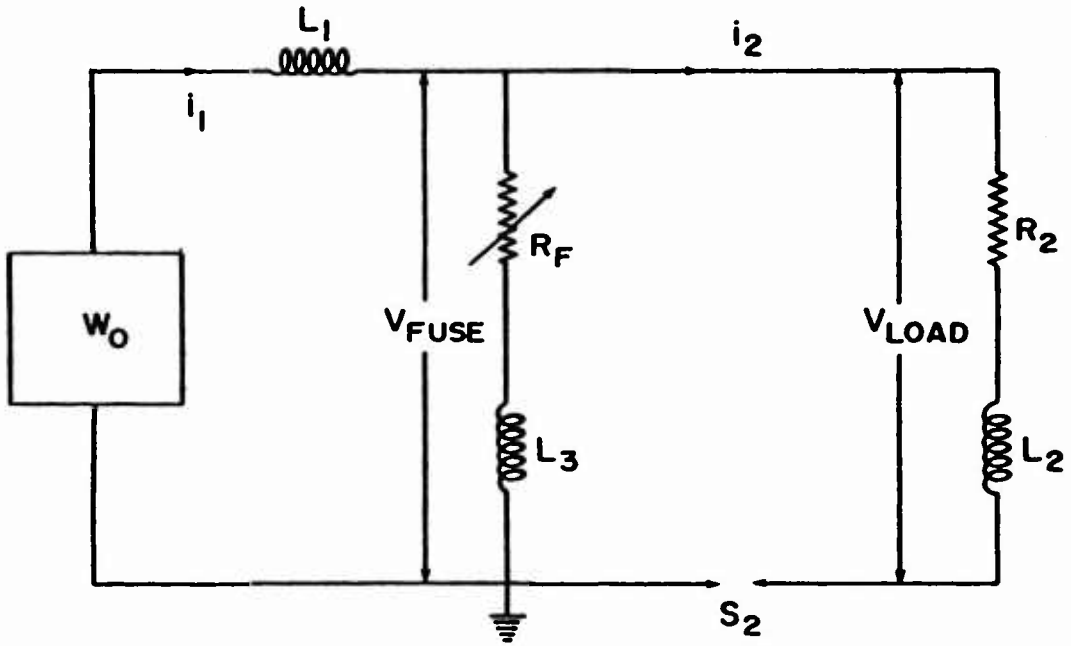

FIGURE "1

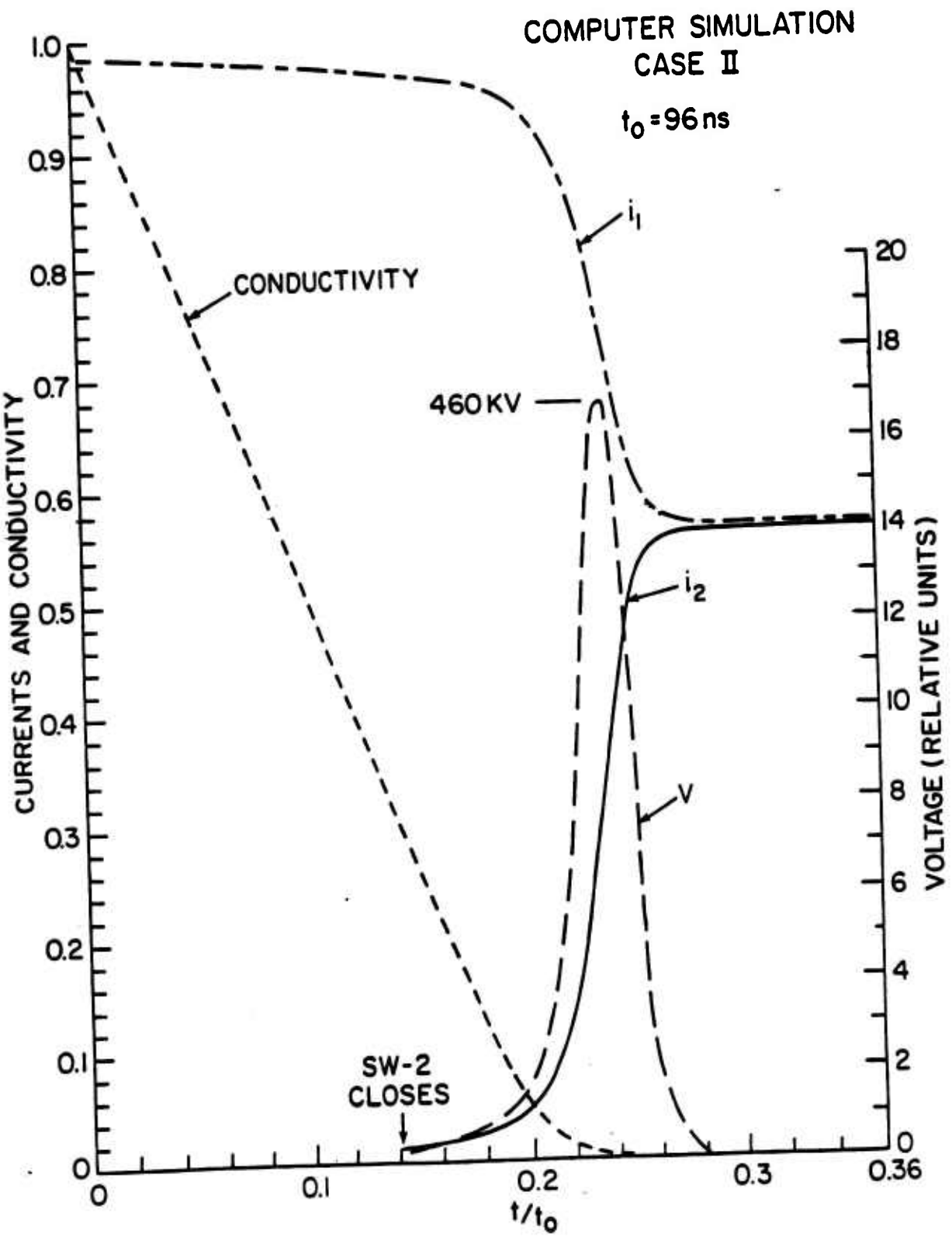
COMPUTER SIMULATION
CASE II
t_0 = 96 ns
i_1
CONDUCTIVITY
460 KV
i_2
V
SW-2
CLOSES
CURRENTS AND CONDUCTIVITY
VOLTAGE (RELATIVE UNITS)
t/t_0
0
0.1
0.2
0.3
0.36
0.4
0.5
0.6
0.7
0.8
0.9
1.0
2
4
6
8
10
12
14
16
18
20

FIGURE 9 VARIATION IN NUMBER OF 5 MIL AL. FUSE WIRES (EACH 10 cm LONG)

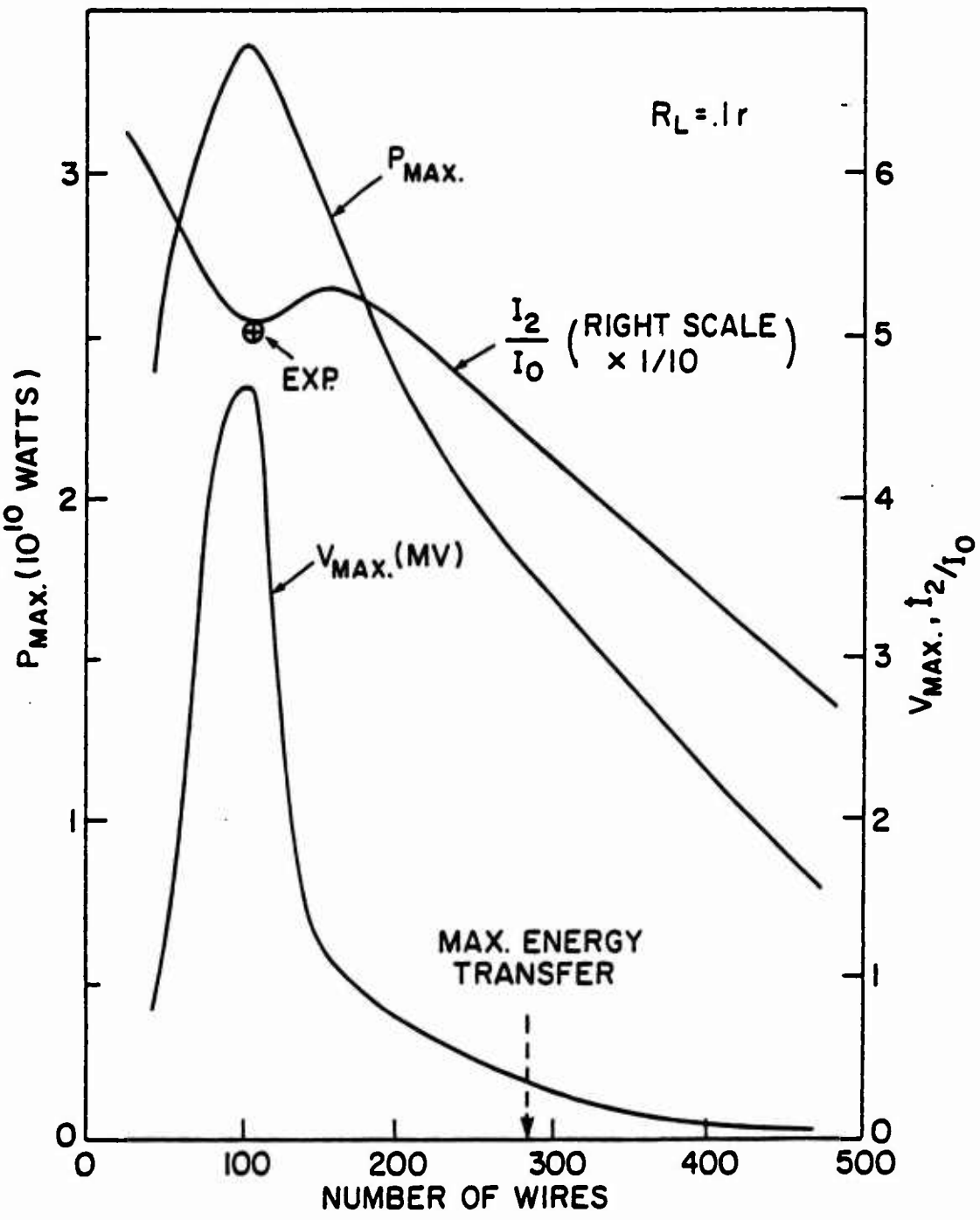

Fig 9 TIME TO BURST (t_0) vs. NUMBER OF WIRES
5 MIL DIA. CU 10 CM LONG

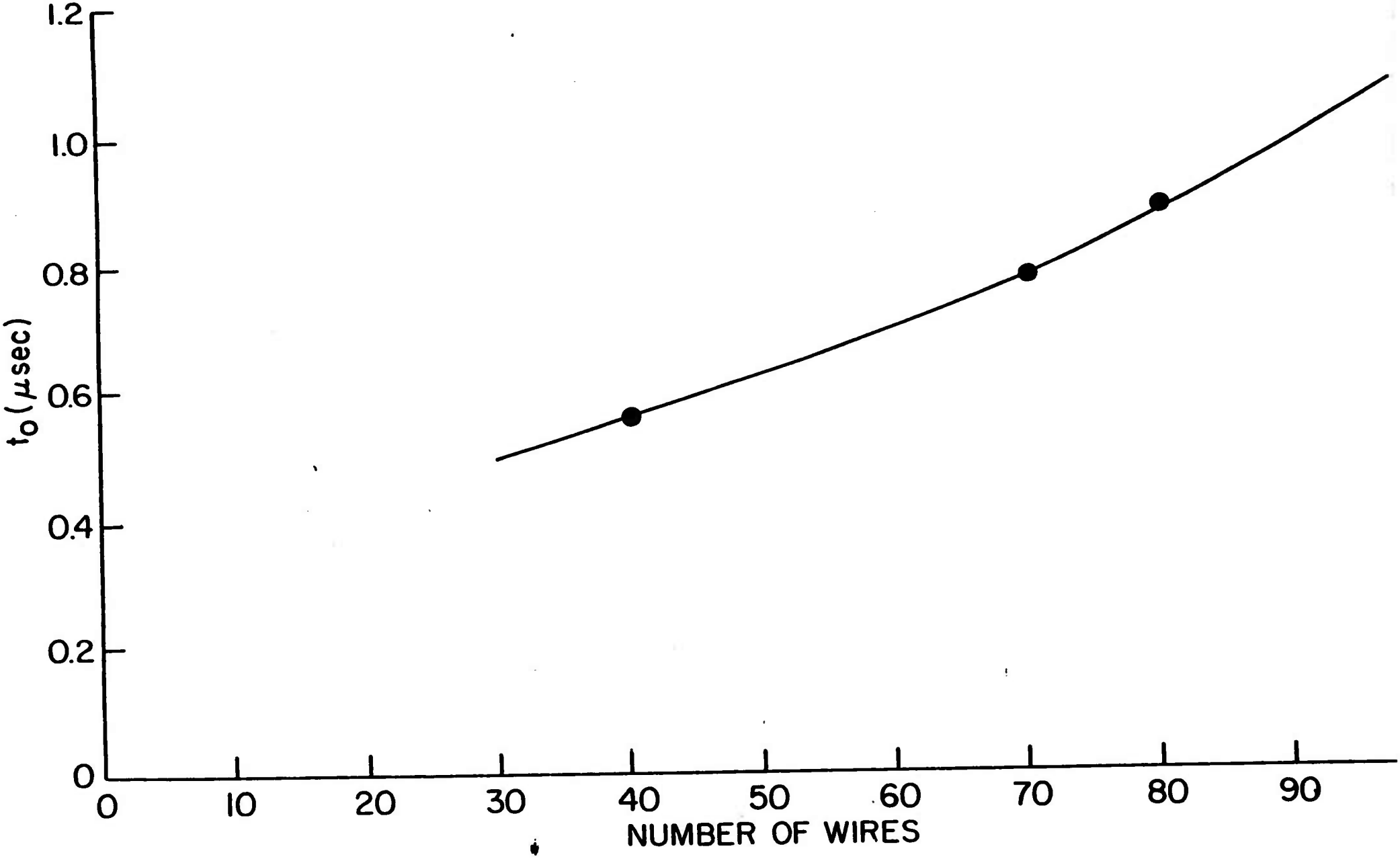

FIGURE 10

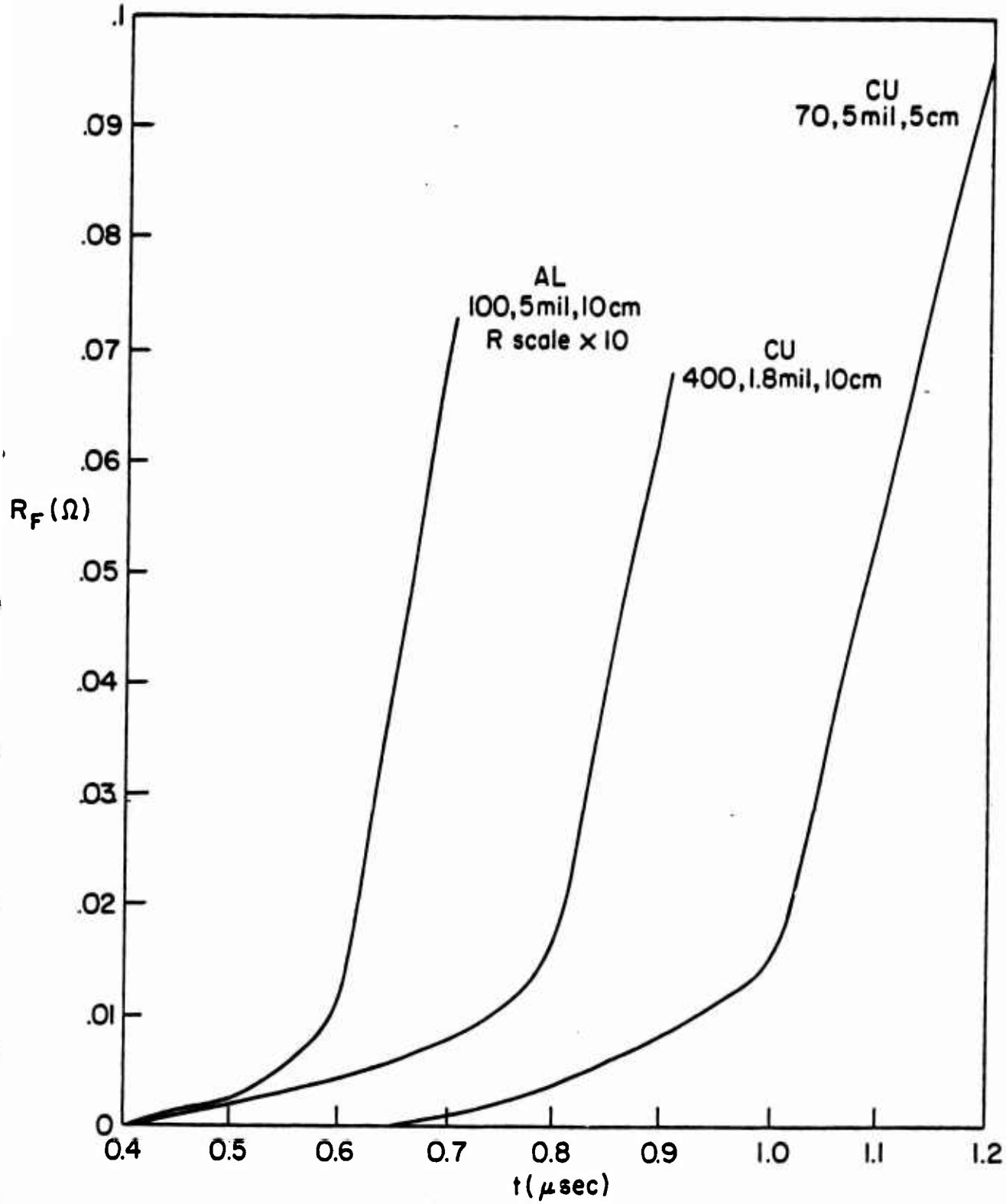
.1
.09
.08
.07
.06
.05
.04
.03
.02
.01
0
$R_F(\Omega)$
0.4
0.5
0.6
0.7
0.8
0.9
1.0
1.1
1.2
t(μsec)
CU
70,5mil,5cm
AL
100,5mil,10cm
R scale × 10
CU
400,1.8mil,10cm

FIGURE 11 TRANSFER OF CURRENT TO AN INDUCTIVE LOAD (MULTI-SHOT)

FUSE: 70, 5 MIL DIA., 5 CM LONG, COPPER WIRES
SWITCH: S-2 THICKNESS = 6 MILS OF POLYETHYLENE
V_{BANK} = 25 KV

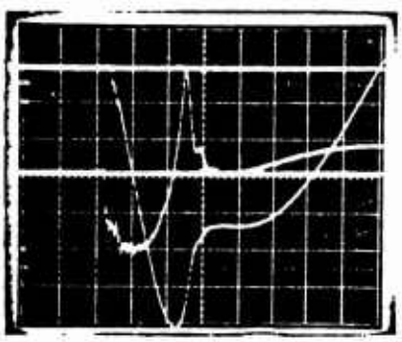

FUSE CURRENT
SWEEP = 500 ns/DIV
TOP TRACE I(t)
LOWER TRACE di/dt

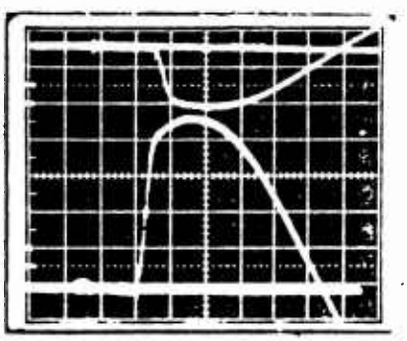

LOAD CURRENT
SWEEP = 500 ns/DIV
TOP TRACE - ROGOWSKI LOOP 1 INTEGRATED
LOWER TRACE - ROGOWSKI LOOP 2 INTEGRATED

FIGURE 12 COMPARISON OF EXPERIMENT AND THEORY

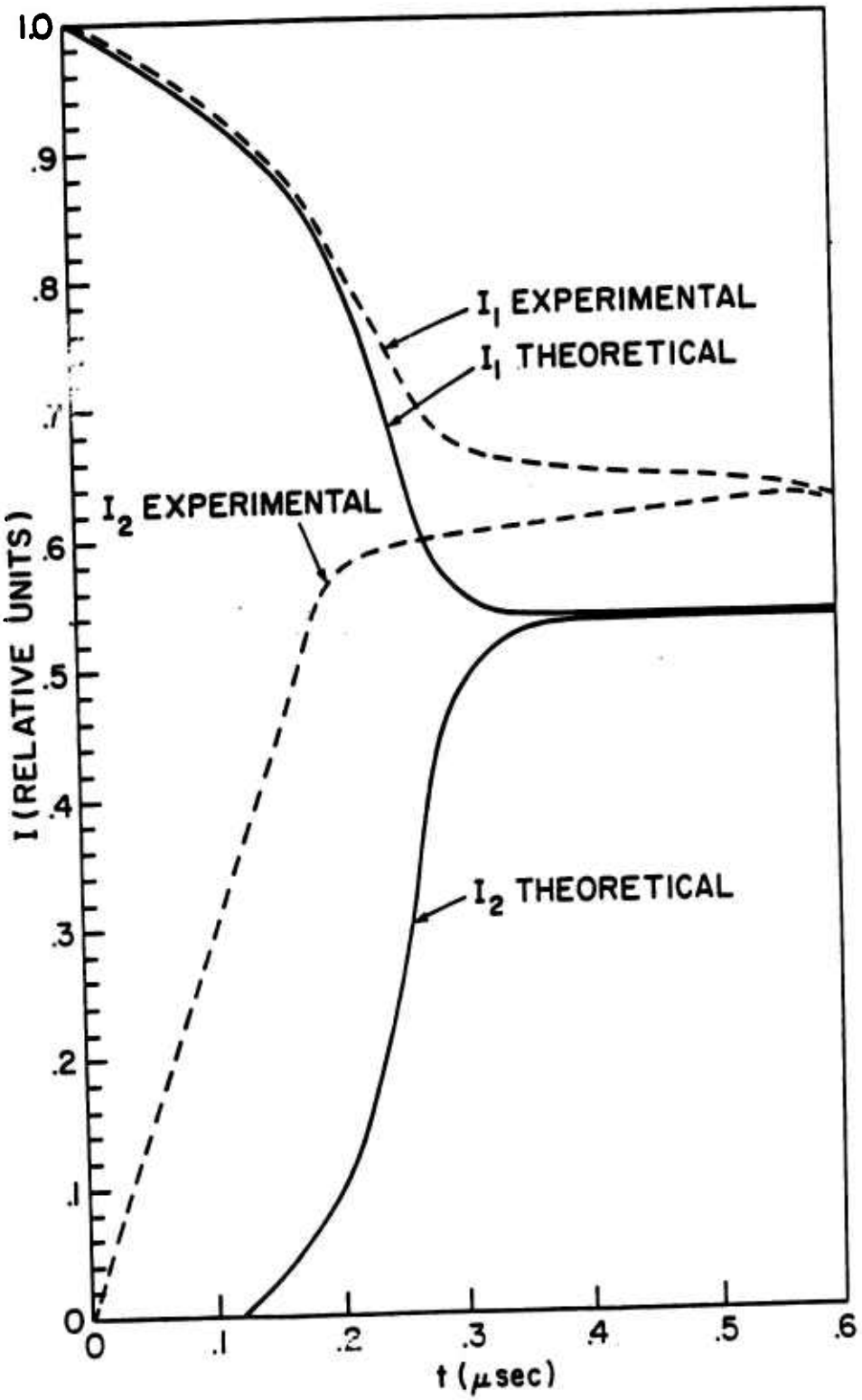

FIGURE 13 STREAK/FRAMING PICTURES OF PLASMA IMPLOSION

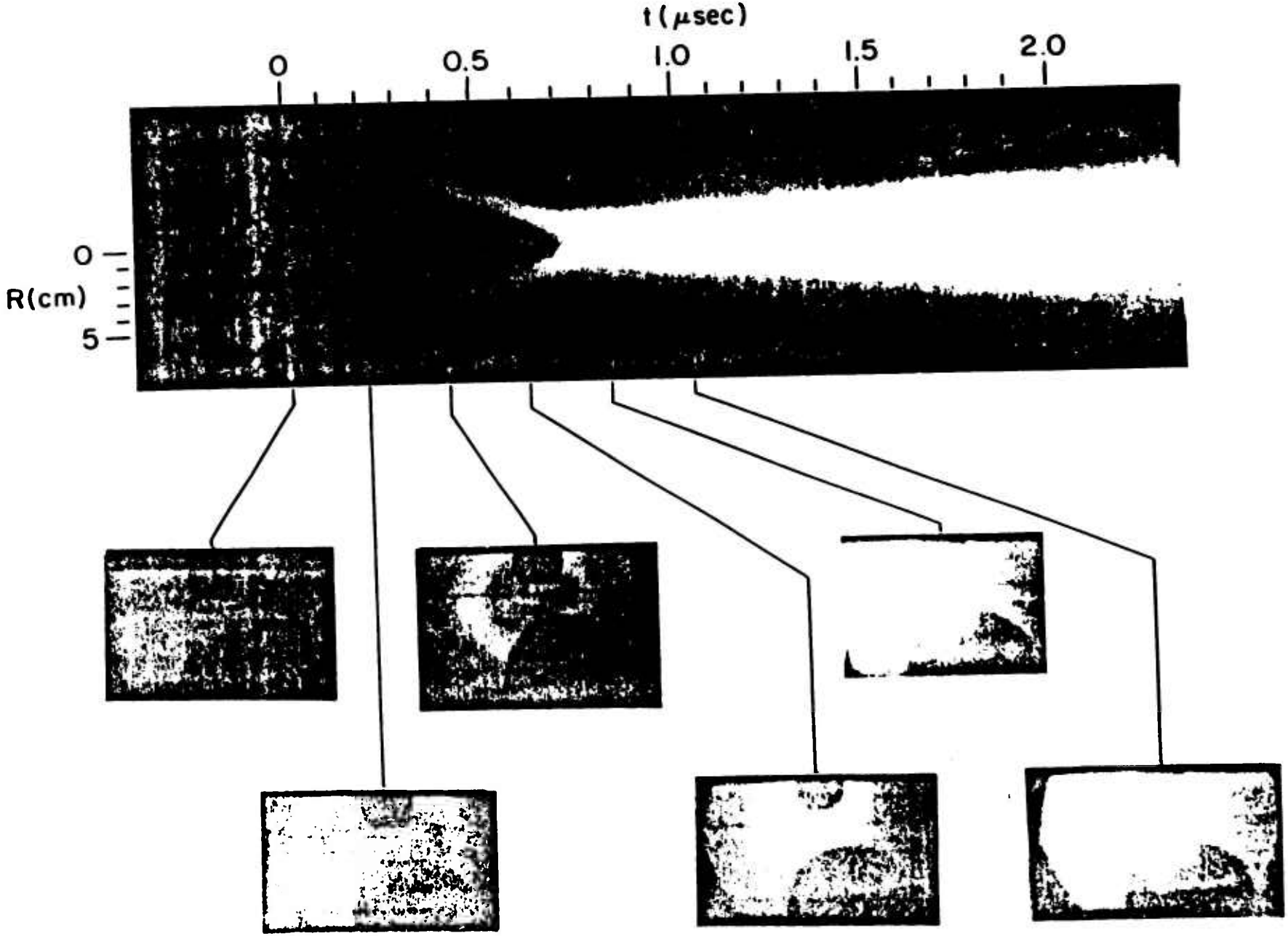

FIGURE 14 SCHEMATIC DIAGRAM ILLUSTRATING FEATURES OF STREAK PICTURE OF IMPLODING PLASMA IN A FAST Z-PINCH (NO FUSE)

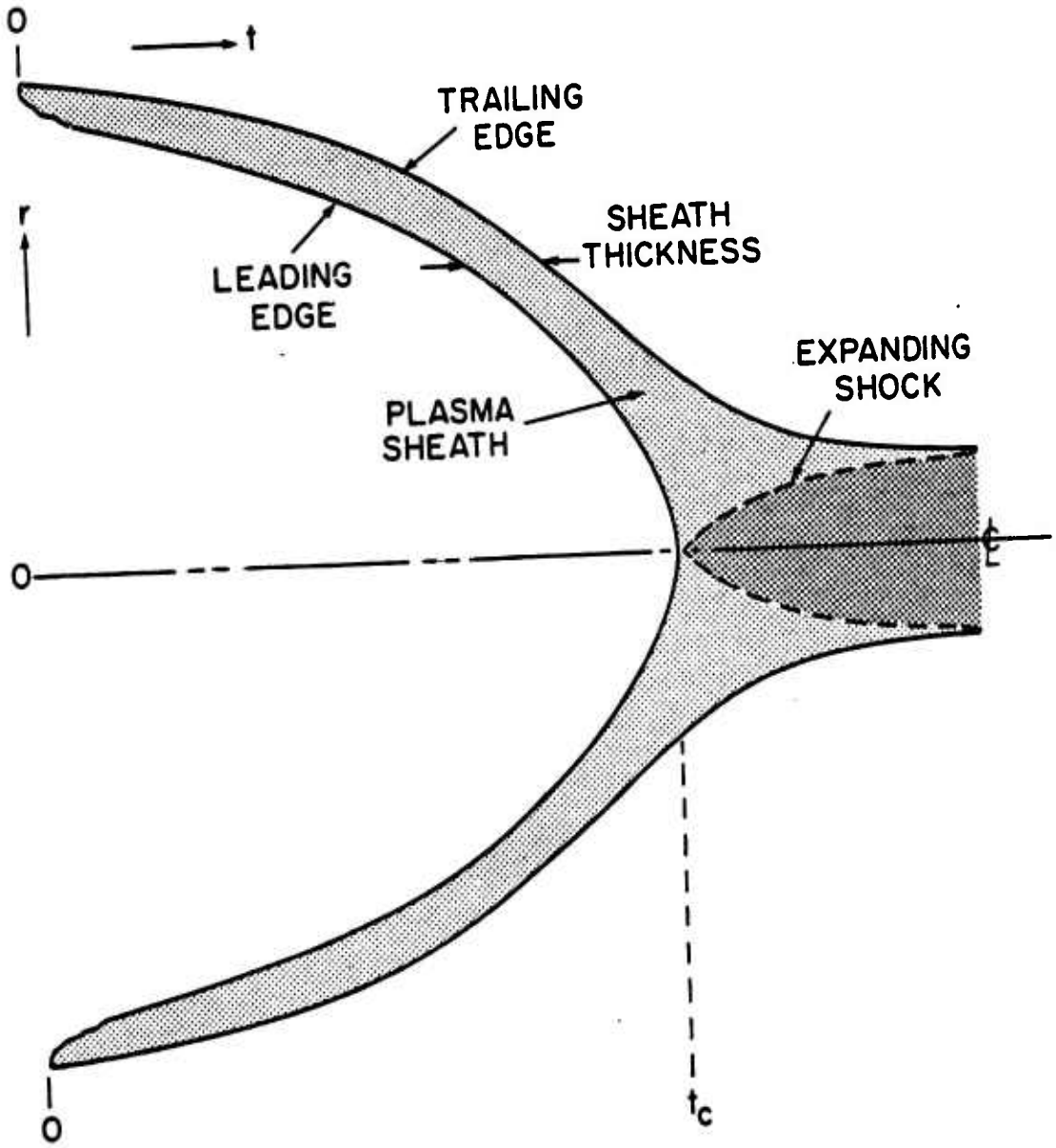

FIGURE 15

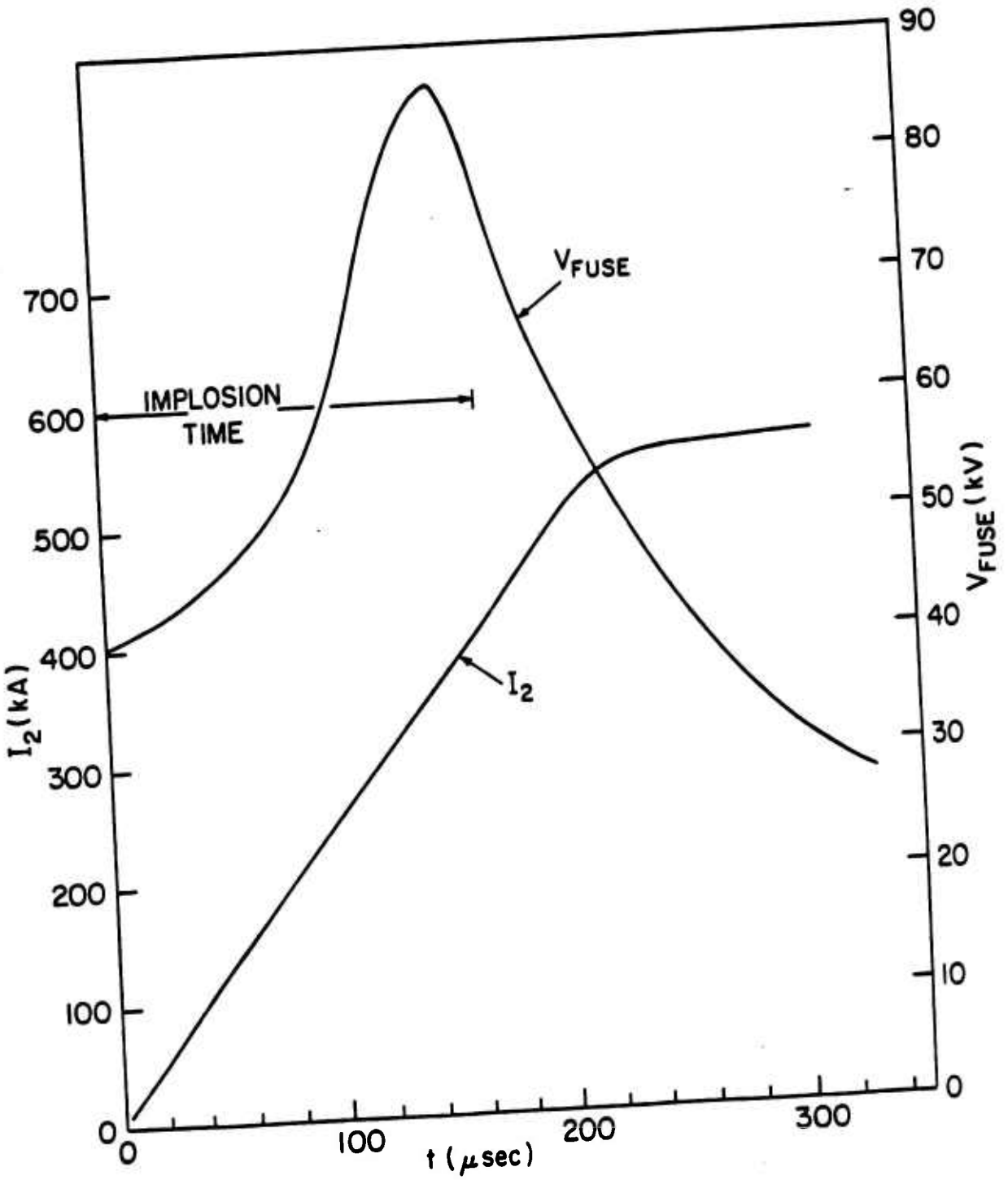
90
80
70
60
50
40
30
20
10
0
700
600
500
400
300
200
100
0
V_{FUSE}
IMPLOSION TIME
I_2
I_2 (kA)
V_{FUSE} (kV)
0
100
200
300
t (μsec)

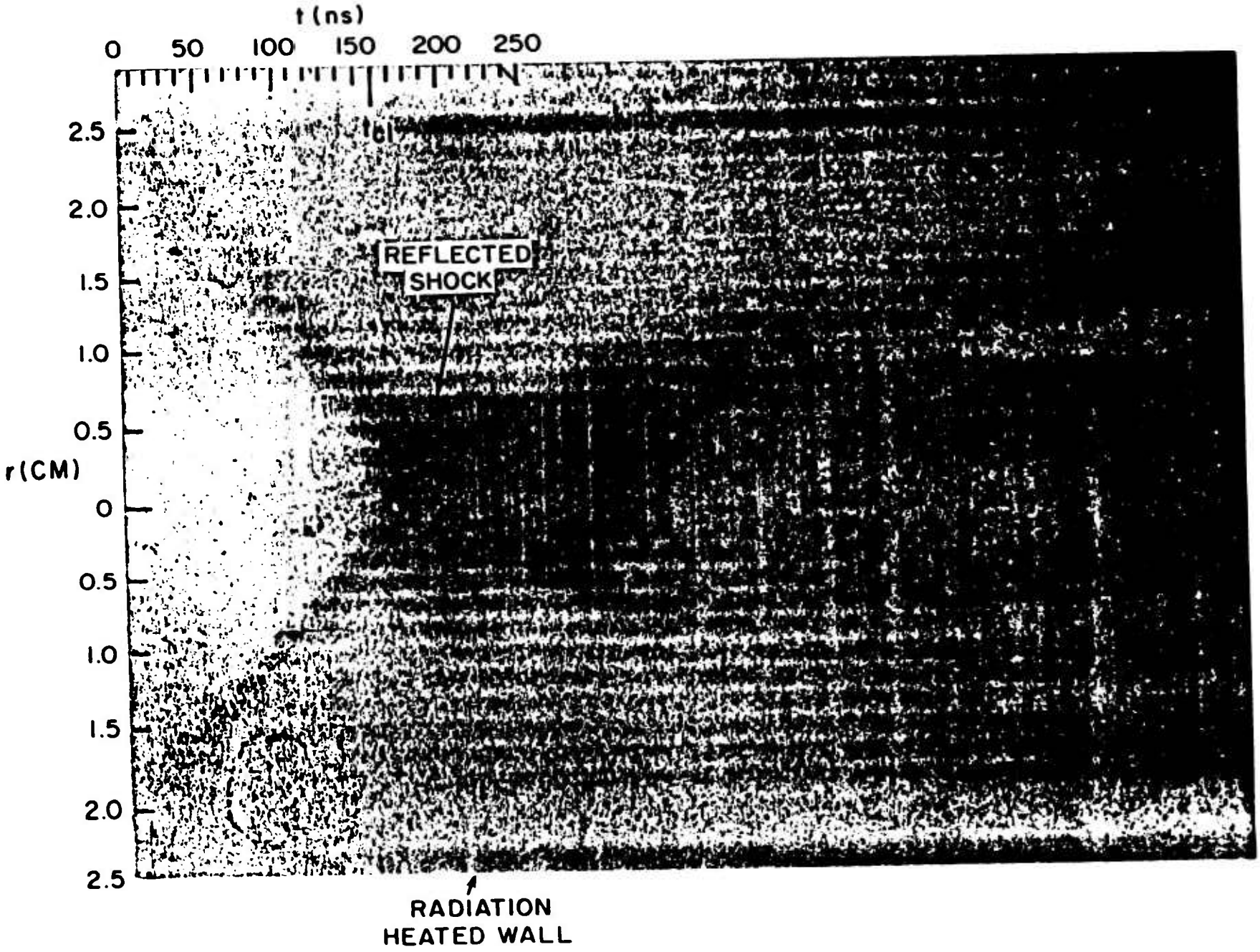
t (ns)
0
50
100
150
200
250
2.5
2.0
1.5
1.0
0.5
r(CM)
0
0.5
1.0
1.5
2.0
2.5
REFLECTED
SHOCK
RADIATION
HEATED WALL

FIGURE 17

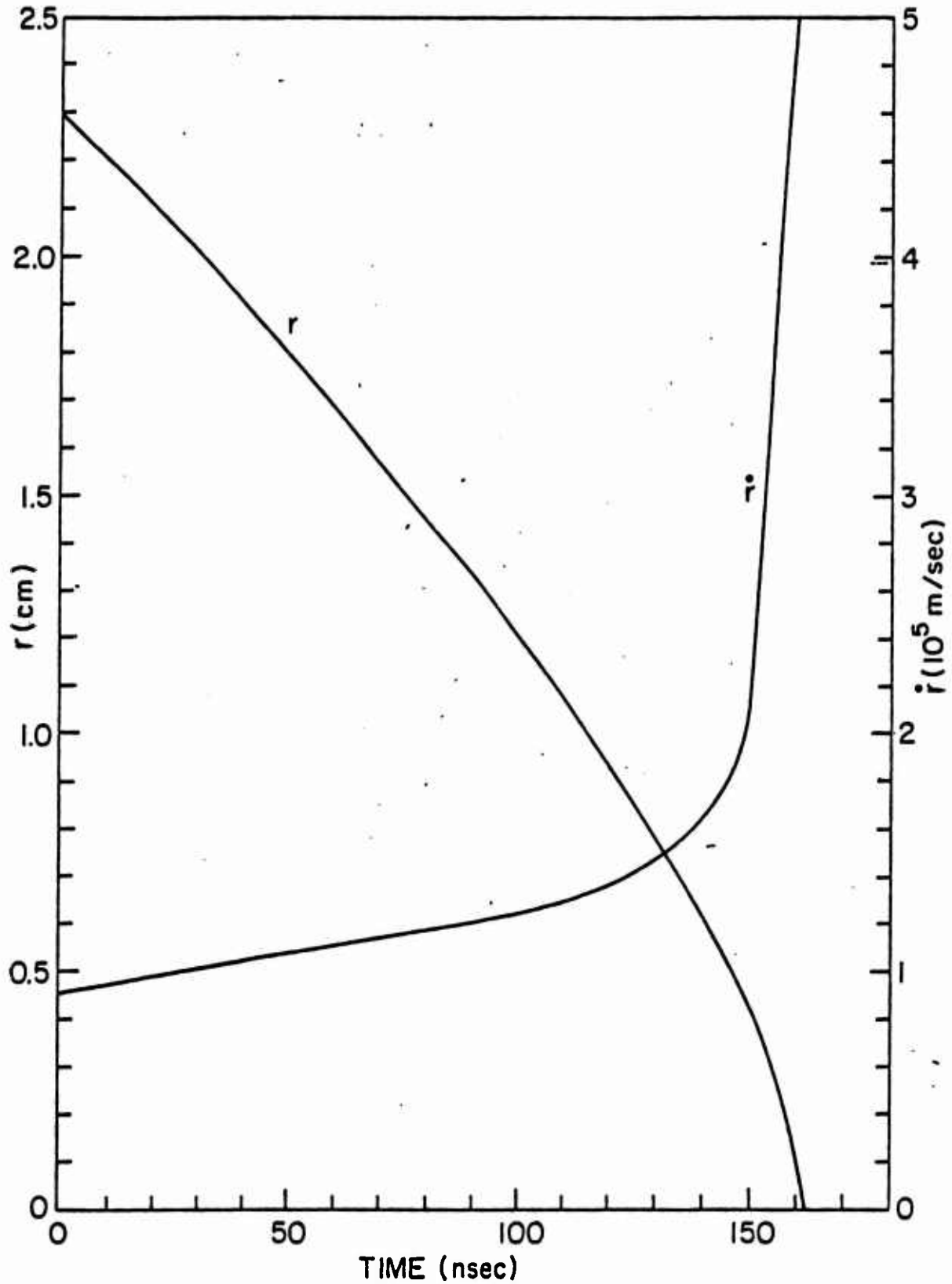

FIGURE 19 IMPLOSION DRIVEN BY FUSE STEEPENED CURRENT

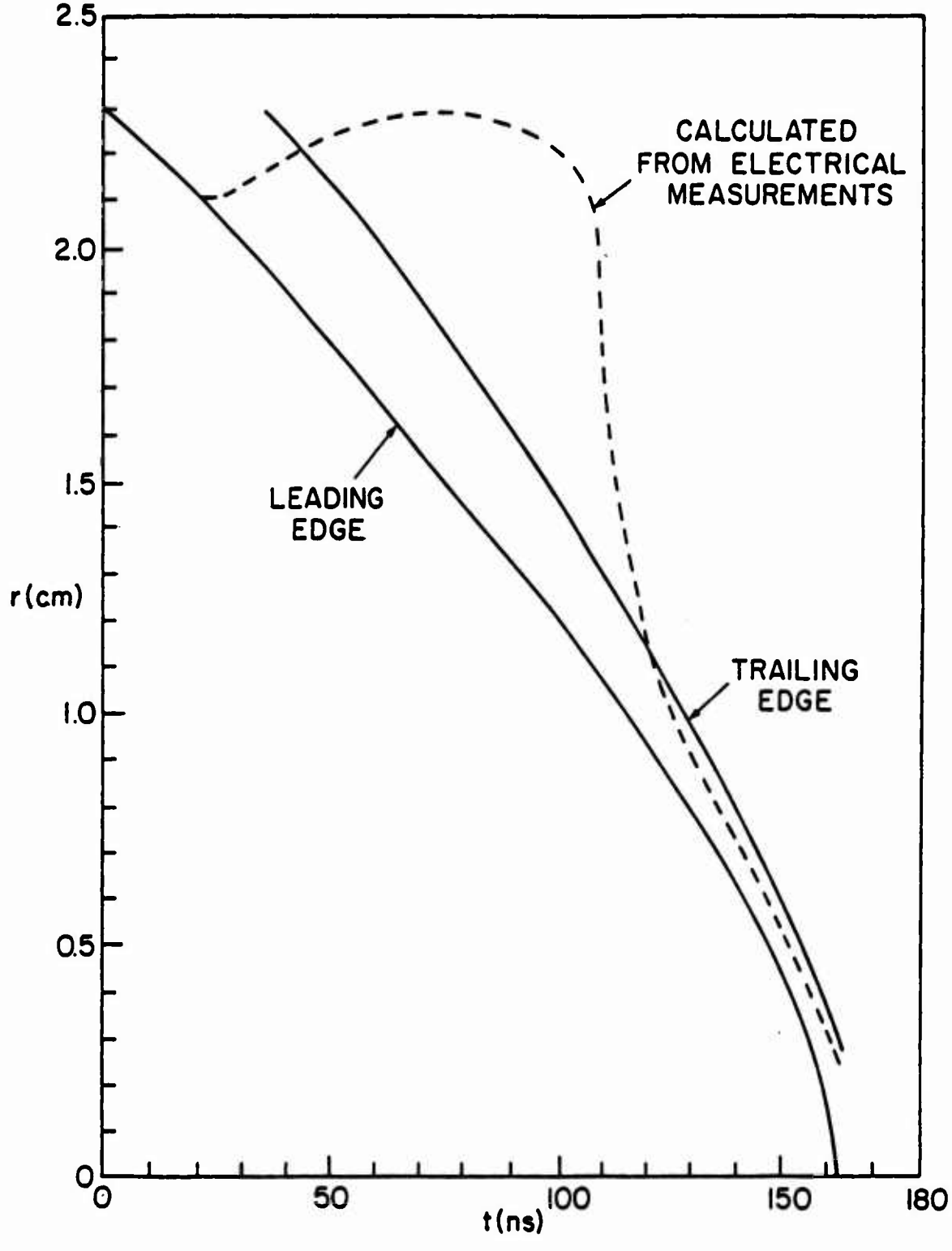

FIGURE 19

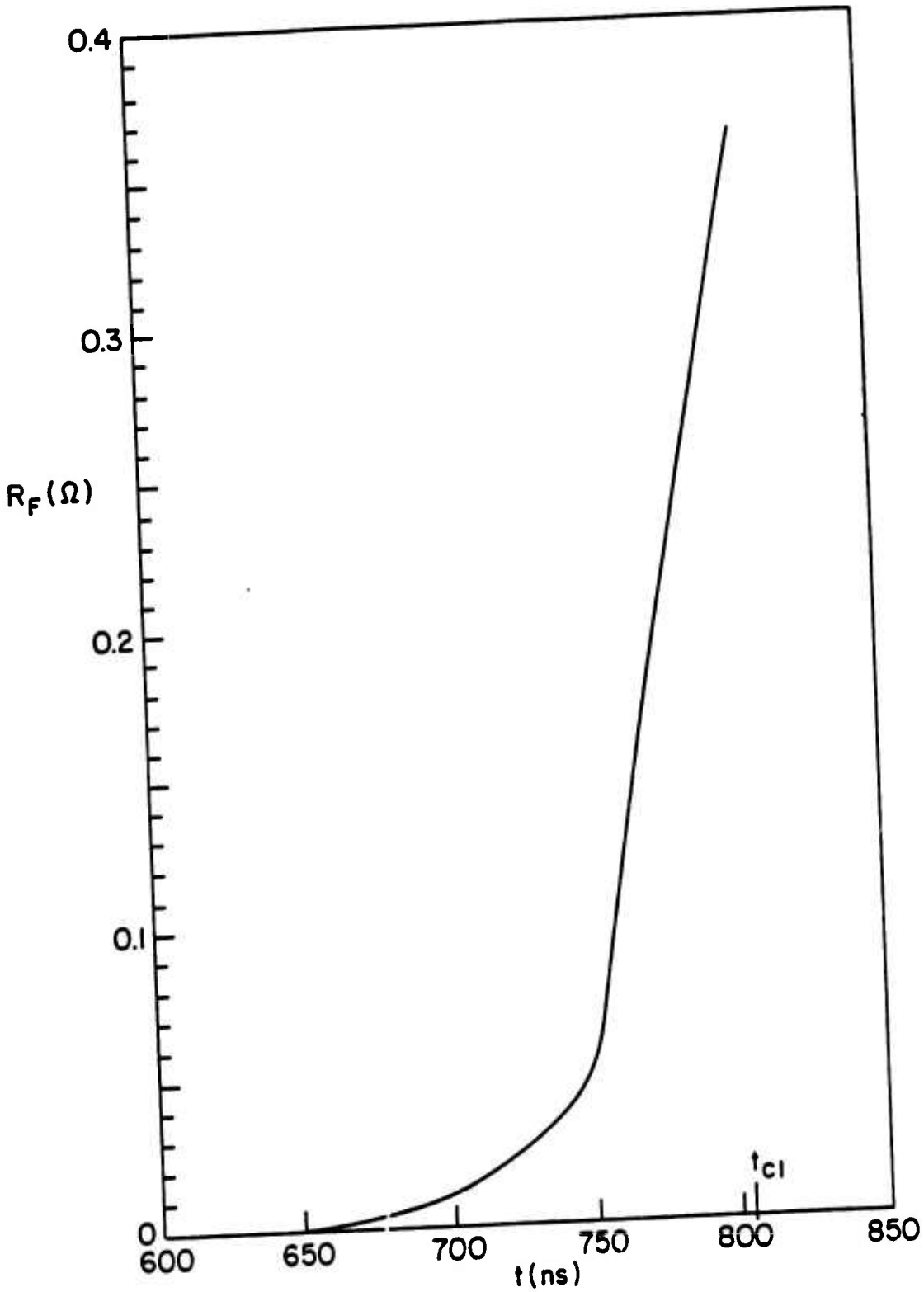

FIGURE 20

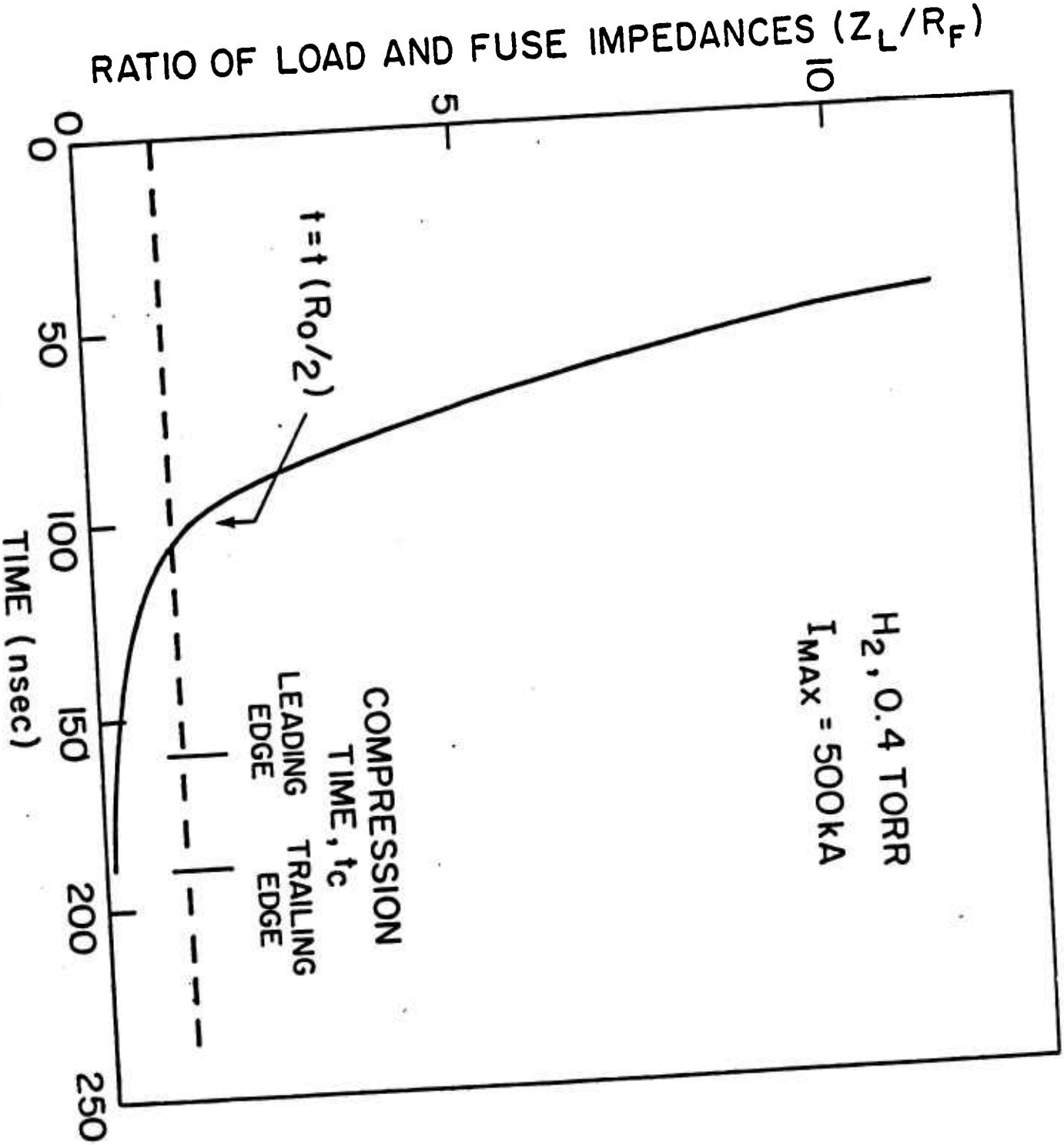
RATIO OF LOAD AND FUSE IMPEDANCES (Z_L/R_F)
0
5
10
0
50
100
150
200
250
TIME (nsec)
$t = t(R_0/2)$
COMPRESSION TIME, t_c
LEADING EDGE
TRAILING EDGE
H_2, 0.4 TORR
I_{MAX} = 500kA

FIGURE 21

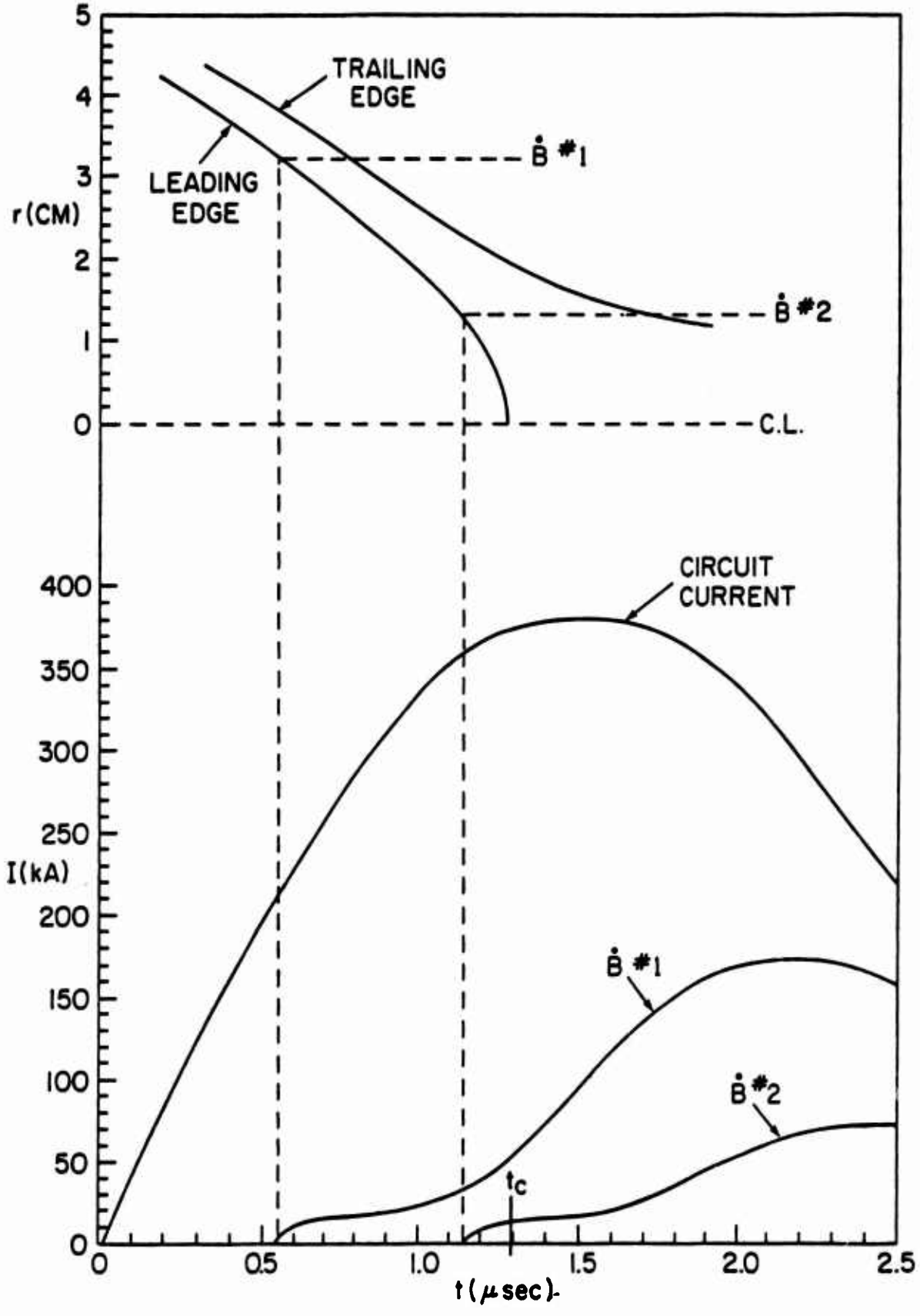
TRAILING EDGE
LEADING EDGE
$\dot{B}$ #1
$\dot{B}$ #2
C.L.
r(CM)
5
4
3
2
1
0
CIRCUIT CURRENT
400
350
300
250
I(kA)
200
150
100
50
0
$\dot{B}$ #1
$\dot{B}$ #2
t_c
0
0.5
1.0
1.5
2.0
2.5
t(μsec)

FIGURE 22

ELECTRICAL MEASUREMENTS FOR PLASMA IMPLOSION DRIVEN BY FUSE STEEPENED CURRENT

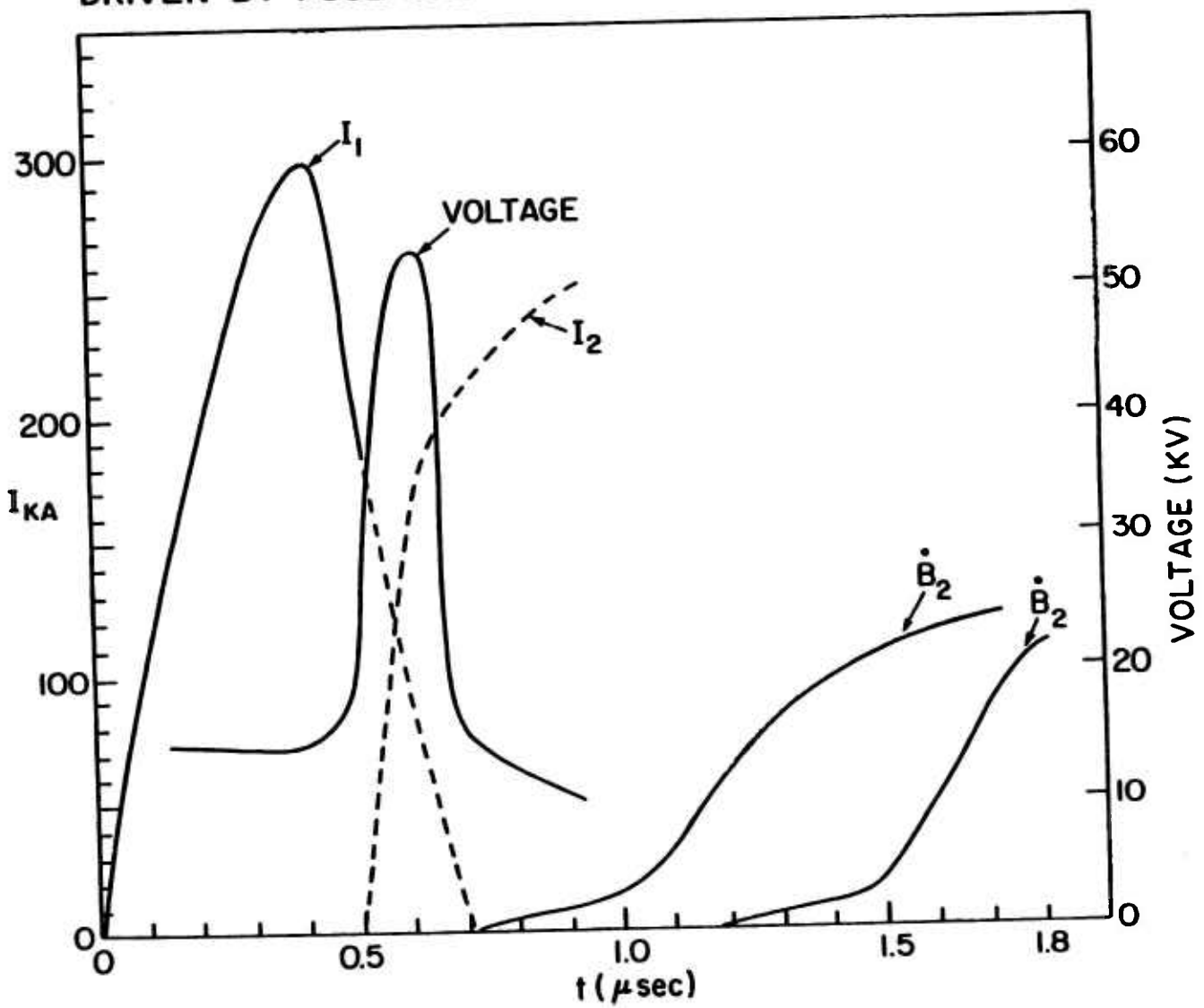

FIGURE 23 DEPENDANCE OF IMPLOSION VELOCITY AND SHEATH THICKNESS ON CURRENT RISE TIME

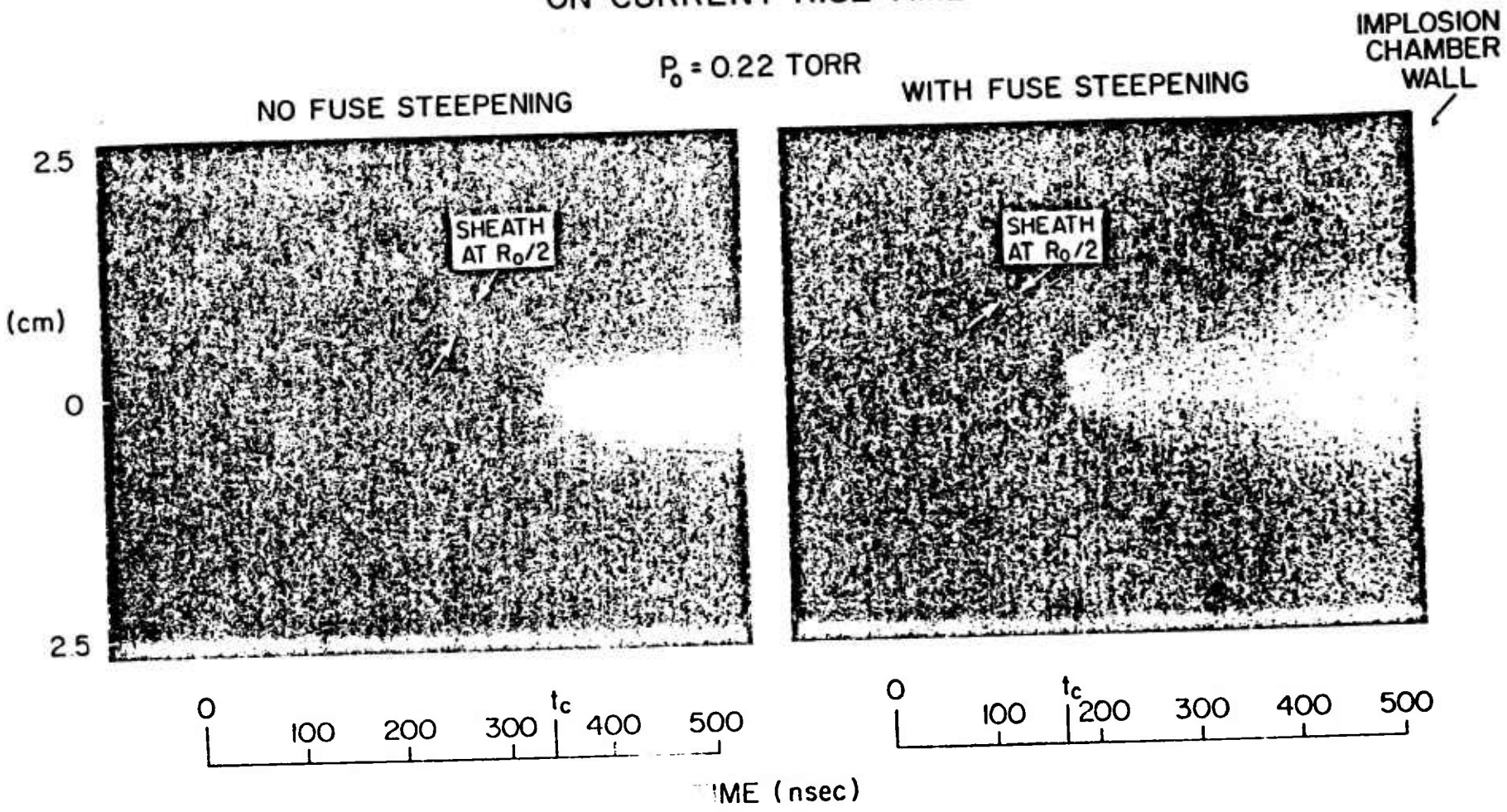

FIGURE 24 COMPARISON OF IMPLOSIONS WITH AND WITHOUT FUSE (LEADING EDGE OF PLASMA)

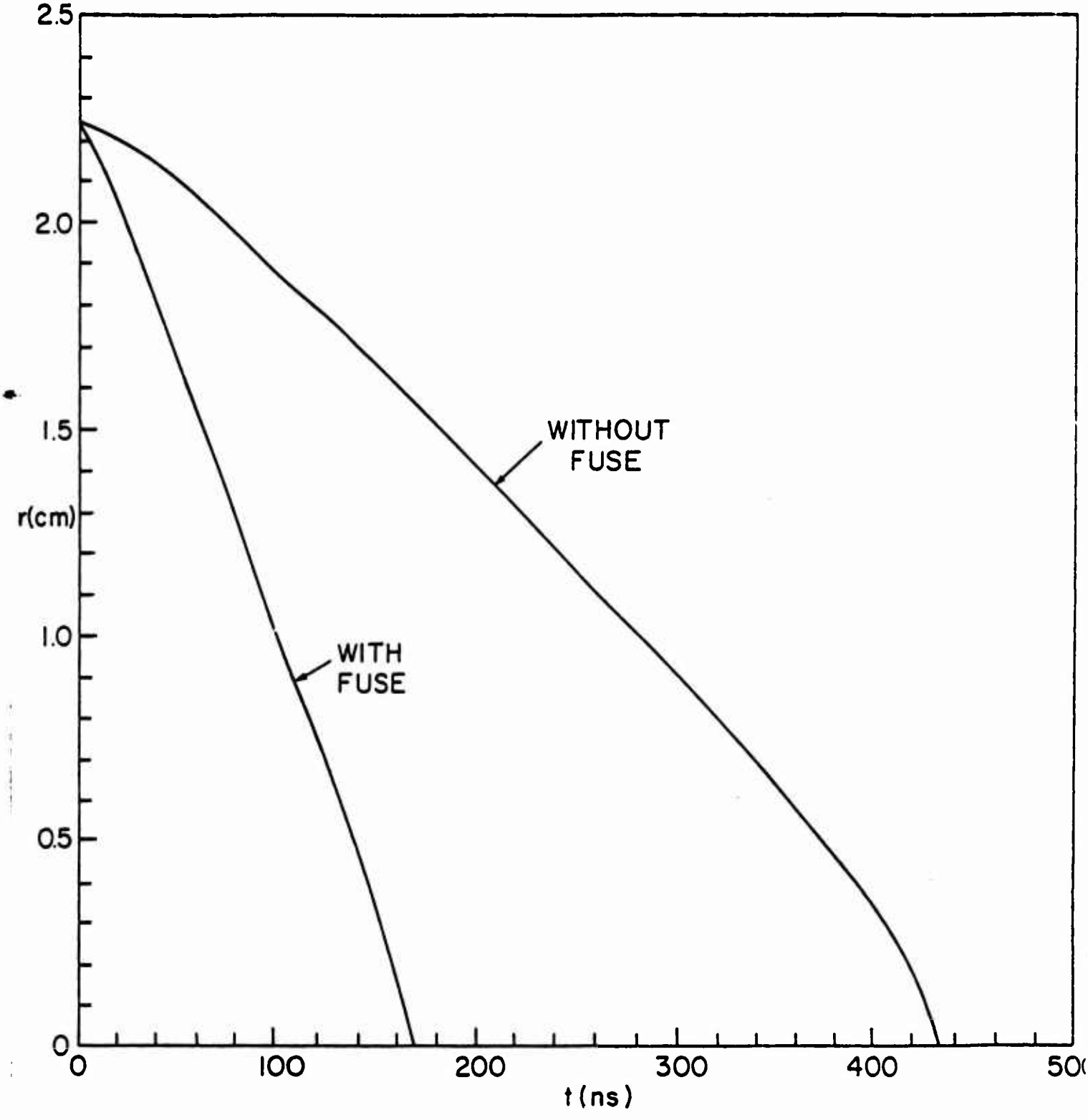

FIGURE 25

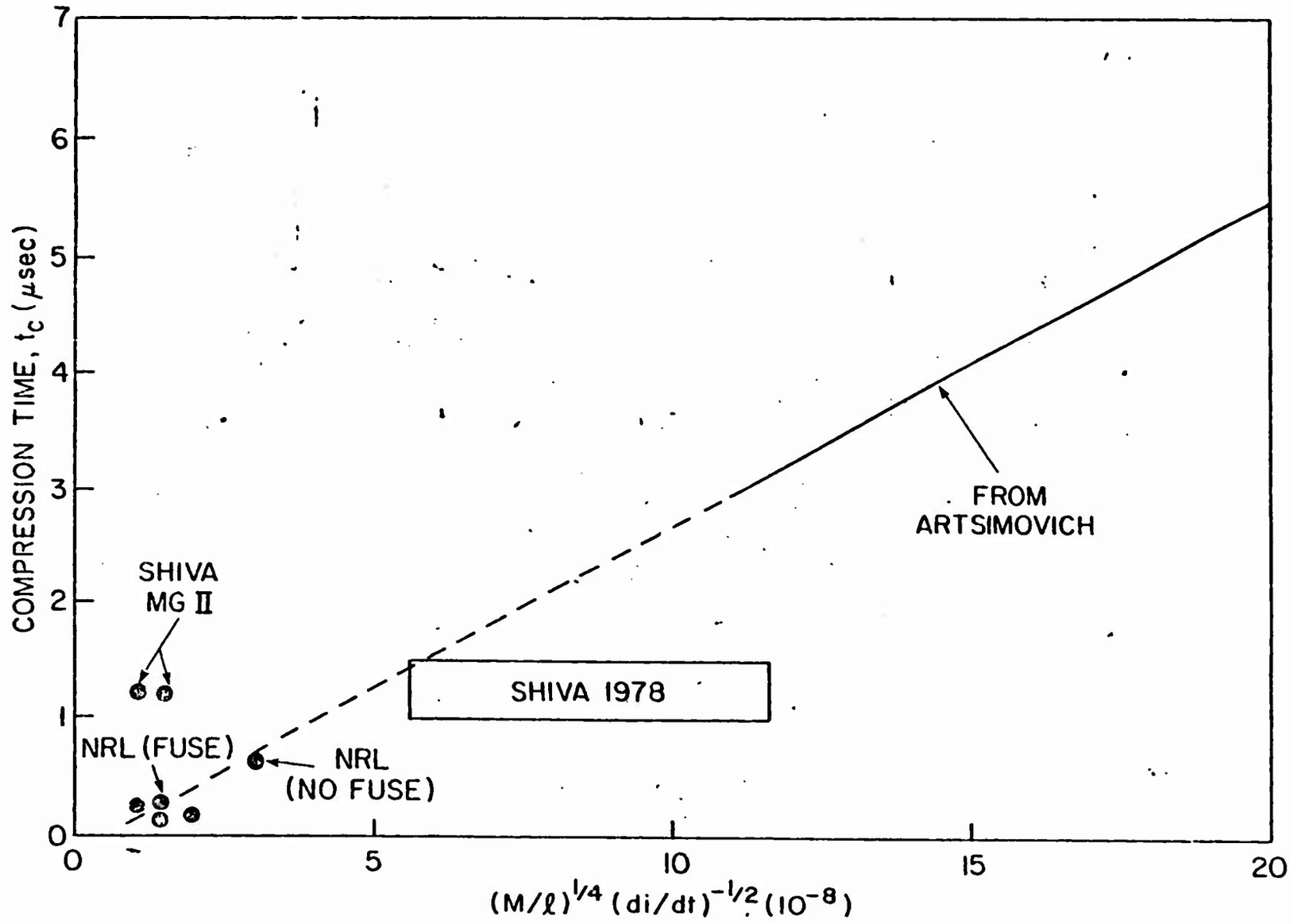
COMPRESSION TIME, t_c (μsec)
$(M/\ell)^{1/4}\,(di/dt)^{-1/2}\,(10^{-8})$
0
1
2
3
4
5
6
7
0
5
10
15
20
FROM ARTSIMOVICH
SHIVA MG II
SHIVA 1978
NRL (FUSE)
NRL (NO FUSE)